University of Udine

Department of Mathematics and Physics

PH. D. THESIS

MONTE CARLO SIMULATIONS FOR THE ČERENKOV TELESCOPE MAGIC–II AND DESIGN OF A NOVEL QUANTUM INTERFEROMETER

Candidate:

F. de Sabata

Supervisors:

Ch.mo prof. A. De Angelis

Ch.mo prof. C. Barbieri

Doctorate of Philosophy in Mathematics and Physics – XXI cycle
Academic Year 2008–2009

Figure 1: The MAGIC stereoscopic telescope system at "El Roque de los Muchachos" (European Northern Observatory, La Palma island)

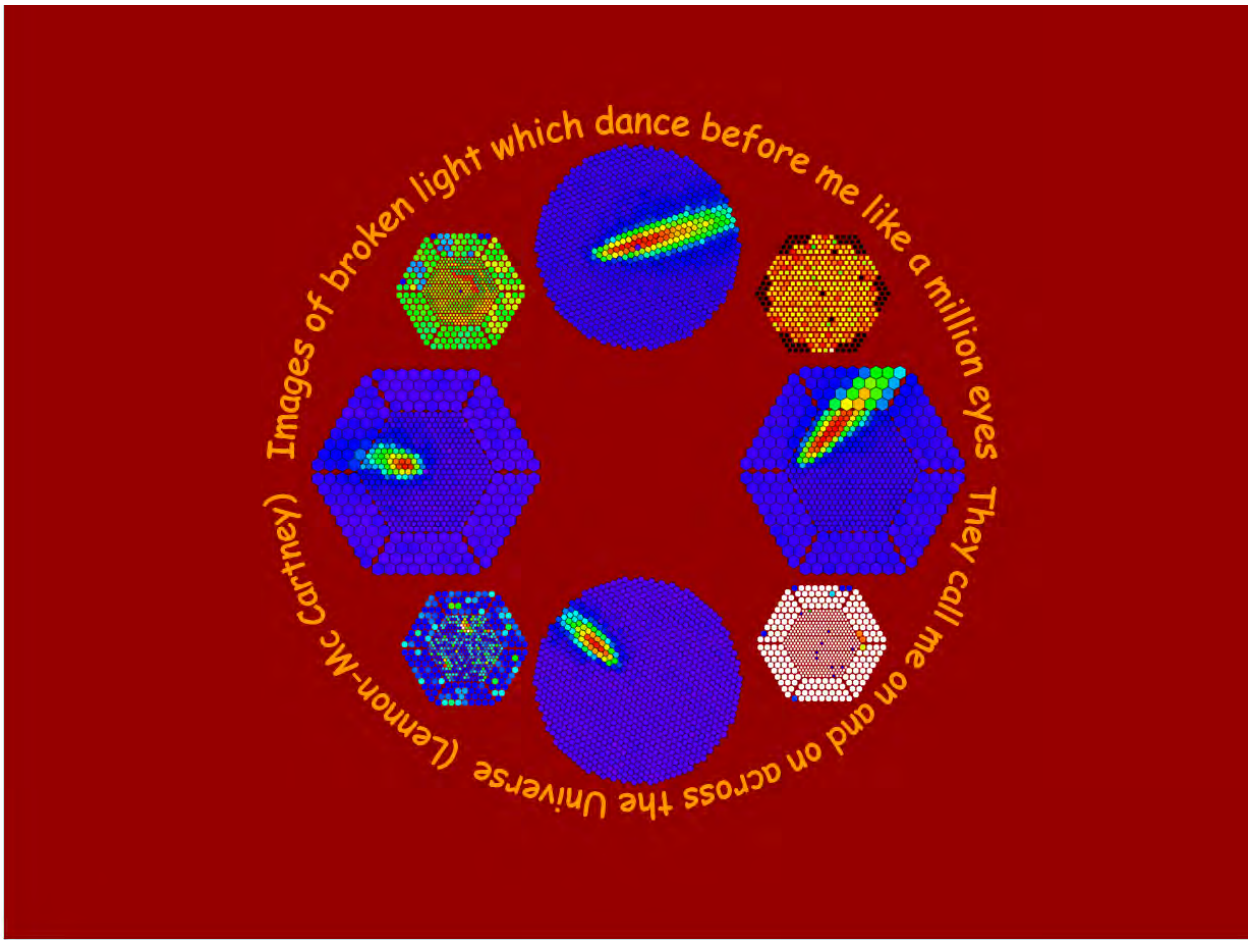
Images of broken light which dance before me like a million eyes They call me on and on across the Universe (Lennon-Mc Cartney)

To little Pietro, who knew the sky imaging of the MAGIC telescope
before the magic of the starry sky
and to Marcella, the true Polar star of my journey across the Universe.

Abstract

MAGIC-II is at present the stereoscopic telescope with the largest single mirrors and technologically the most advanced instrument employing the IACT technique to detect and study VHE γ-ray cosmic signals.

A single MAGIC telescope has been operating on the Canary island of La Palma since the summer of 2004; more than two hundred physicists from different countries (with Germany, Italy and Spain as main partners) join their efforts to develop its technical and scientific achievements.

The MAGIC collaboration already produced many important discoveries and results on different topics of γ-ray astrophysics, with more than forty related scientific publications (end of 2008). The first chapter of this thesis is a rapid overview on the VHE γ-ray astrophysics field.

The rapid technological progress and the successes of the first observations of AGNs and γ-rays galactic sources have encouraged the MAGIC physicists to improve the detector, building a second "clone" telescope to perform more accurate and detailed measurements.

The new MAGIC-II stereoscopic system, whose first light is planned for early 2009, will enhance both the sensitivity and the precision of the observations with respect to the single telescope, lowering at the same time the energy threshold for the detection. The telescope is described in detail in the second chapter.

An extensive analysis of technical features and performance of the new instrument is of primary importance for the correct interpretation of the experimental results.

As a part of my PhD work, I developed and maintained the new database of simulated events required to study in detail the functioning and performance of the new telescope: the produced data are presently available via web to the MAGIC collaboration members.

I used this large statistical simulated sample to determine precisely the sensitivity of the stereoscopic MAGIC-II before the commissioning of the second telescope: the results are illustrated in detail in the third chapter.

I also investigated the possible use of MAGIC-II in observational fields other than γ-ray astrophysics, as the advanced optics and electronics performance of the telescope disclose new perspectives on different scientific applications, mainly in the field of quantum astronomy, whose historical and theoretical backgrounds are reviewed in the fourth chapter.

The use of MAGIC-II as intensity interferometer turns out to be of particular interest for astronomical studies, from fine imaging of stellar systems to the variations of astrophysical sources on the shortest time-scale.

The possibility of detecting single optical photons also allows to indagate sophisticated quantum correlation effects, e.g. to probe the nature of possible cosmic laser sources.

I developed therefore a project of a novel quantum interferometer to be implemented on MAGIC-II: the project is illustrated in detail in the fifth chapter.

During my PhD work within the MAGIC collaboration, I was also involved in some outreach activities and communicating physics in the schools: a didactical project carried out in a secondary school and the production of outreach materials are briefly illustrated in Appendix A.

Contents

Chapter 1

Very High Energy gamma-ray astrophysics

Astronomy and astrophysics have always achieved important advances whenever a new observational window has been opened on the Universe, thanks to the availability of new istruments or to the development of new techniques. This has happened since Galileo turned his new "cannone occhiale" up to the starry sky [Gal10], inaugurating a new era in the astronomical observations.

Getting closer to modern times, the introduction of photographic imaging techniques coupled with optical telescopes brought great results, as in the observations by A. Eddington [Dys20] and E. Hubble [Hub29], which originated modern cosmology.

The use of photographic emulsions as tracking devices, which allowed the pioneering observations of particle production by cosmic rays, can be regarded as a milestone both in cosmic-ray astrophysics and in the field of elementary particles (see e.g. [Ros64]).

Impressive astronomical breakthroughs have also come from observations in the radiowaves range, which led to the discovery of new classes of objects, including radio galaxies, pulsars and quasars. The study of such objects pointed out the extreme energetic nature of the Universe, which could have been hardly imagined on the basis of purely optical observations.

The microwave astronomy has also given crucial results in probing the evolution of the Universe since the discovery of the *Cosmic Microwave Background* (CMB) made by A. Penzias and R. Wilson [Pen65].

The infrared-detectors allowed for the first time the observations of the dense interstellar dust clouds which were recognized as the birthplace of stars, giving experimental access to the very first phases of stellar evolution, long before hydrogen burning starts.

The beginning of research in higher energy ranges, namely X-ray and γ-ray astrophysics, was historically delayed to the end of the 1950's because these radiations do not reach the Earth at ground level: their detection required rocket and satellite technology to carry the instruments out of the atmospheric shelter (nowadays, ground-based detection of γ-rays is also possible with indirect techniques, like the Čerenkov imaging of the showers produced in the atmosphere by the impinging cosmic rays which will be illustrated in section 1.5.2).

The detection of Sco X-1, the first extrasolar X-ray source discovered in 1962 by R. Giacconi and B. Rossi with rocket-borne Geiger counters [Gia62], can be regarded as a further example of the strong relationship between the application of new techniques and the discoveries in previously unreachable energy domains.

Due to the early promise of strong sources and ease of detection also in the γ-ray energy range [Mor58], the technique of balloon- and satellite-borne detectors was tried in the same years, first

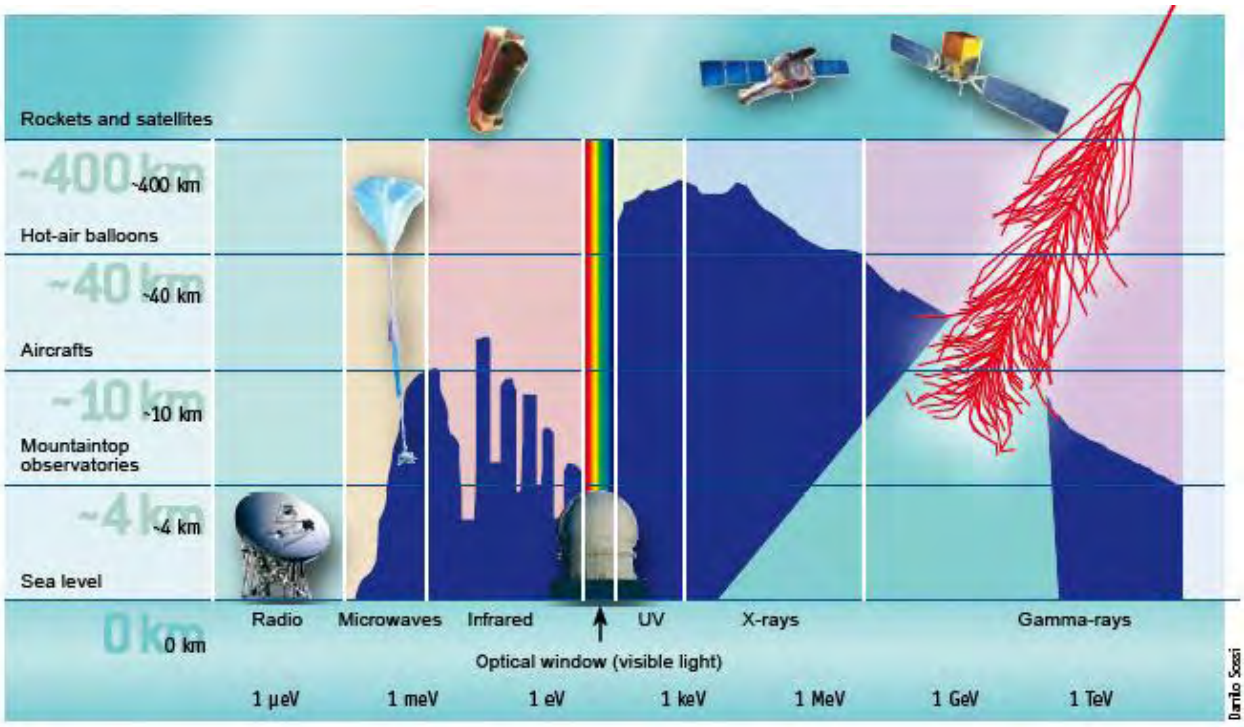

Figure 1.1: *Transparency of the atmosphere for different photon energies and possible detection techniques [Ang08c].*

with negative or controversial results.

The building of Čerenkov telescopes started in the early 1960's, following the first observations of atmospheric Čerenkov radiation and the theoretical predictions [Coc59] for ground-based (indirect) detection of cosmic γ-rays with an energy order of 10 – 100 GeV.

This technique established a firm result in 1989, with the discovery of the first steady γ source at very high energy (VHE, roughly more than 10 GeV), the Crab Nebula [Wee89], which became the "standard candle" for the subsequent γ sources.

VHE γ-ray astronomy opened a privileged window on the "non-thermal Universe" and its constituents (see figure 1.2), such as Supernovae, Supernova Remnants, Black Holes, Active Galactic Nuclei (respectively SN, SNR, BH, AGN hereafter), or the detection of Gamma Ray Bursts (GRB).

The variety of phenomena which can be investigated through VHE γ-ray detection fully justify the efforts to develop new instruments and techniques to access this energy range both from satellite and ground level.

This chapter introduces to VHE γ-ray astronomy, starting from the mechanisms of production and absorption of cosmic γ-rays, turning then to the description of the different kinds of sources and ending with general information about γ-ray detectors.

1.1 The gamma-ray window on the Universe

High energy astrophysical processes are known to produce relativistic particles and the associated gamma radiation over an energy range spanning from 10^6 eV to 10^{20} eV and even more.[1]

[1]The theoretical upper limit on the energy of cosmic rays from distant sources, known as the GZK cutoff [Gre66, Zat66], is due to a resonant interaction of protons with energies greater than 10^{20} eV with the CMB photons. Over

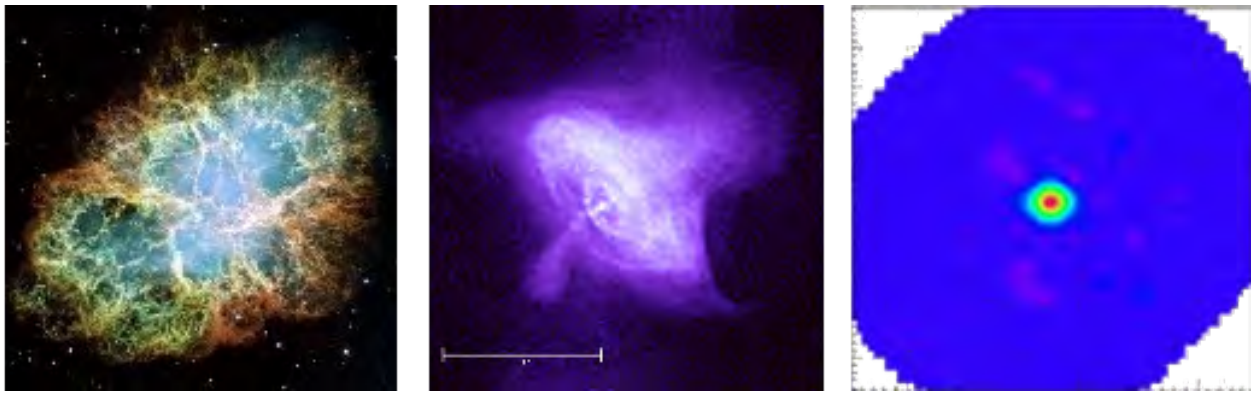

(a) (b) (c)

Figure 1.2: *The Crab Nebula as oserved at different wavelengths: (a) in the optical range, (b) in the X-ray range and (c) as seen by MAGIC in the γ-ray range (image courtesy (a), (b): NASA).*

The bulk of cosmic rays flow (not considering neutrinos) consists of charged particles as protons (roughly 90%), helium nuclei (less than 10%), ionized heavier elements and electrons (less than 1%). The γ-ray component, i.e. photons with energy greater than 1 MeV, is just a tiny fraction, ranging from 0.1% to 1% of the total.

The flux variation with energy is referred to as the *energy spectrum*. The flux dependence on the energy E of the particle can be approximated by a power law $dN/dE \propto E^{-\alpha}$ (the spectral index α ranging between 2.5 and 3) over ten decades of energy with few noticeable structures (see figure 1.3.a).

The slope steeping around $10^{15.5}$ eV is called the "knee" of the spectrum (whith α raising from ~ 2.7 to ~ 3), while the flattening which occurs around $10^{18.5}$ eV is referred to as the "ankle".

It is generally believed that cosmic rays with energy below the knee value have a galactic origin and that they have been confined inside our Galaxy for at least 10^7 years by its magnetic field, which is of the order of 1 μG.

On the other hand, energies above 10^{17} eV might denote an extragalactic origin of the cosmic rays, as the galactic magnetic field could not trap them, being the extragalactic field of the order of 10^{-10} G [Ang08b].

In both cases, it is very difficult to determine the initial direction of cosmic protons: on the contrary, the positioning of γ-ray sources is easier and more reliable, as photons are not deflected by magnetic fields.

The clean information on the source position and the wide high energy range spanned make γ-rays the most interesting part of the spectrum emitted from astrophysical sources (see figure 1.3.b).

γ-ray astronomy has rapidly developed in recent years (see e.g. [Hof99a, Wee03a] as introductive lectures and [Aha08, Ang08c] for the most recent results): the classification in energy ranges used throughout this work is mostly based on T. C. Weekes' previous definitions [Wee03a]:

- low energy (LE) for γ-ray energy ranging from 1 MeV to 10 MeV;

- medium energy (ME) for γ-ray energy ranging from 10 MeV to 30 MeV;

adequate distances the reaction $p + \gamma \rightarrow \Delta \rightarrow N + \pi$ lowers the initial proton energy to the threshold value. This mechanism, recently confirmed by experiments [Yam07], inhibits the observations of extragalactic cosmic rays with such initial energies coming from sources farther than 100 Mpc.

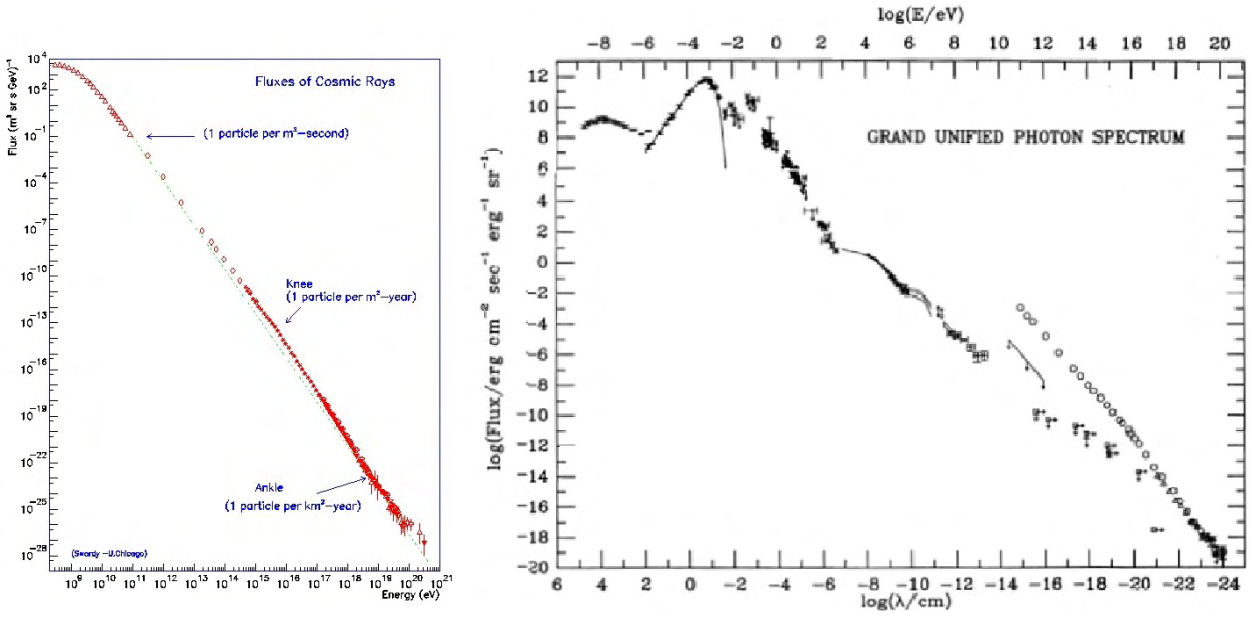

(a) (b)

Figure 1.3: *(a) Energy spectrum of cosmic rays [Cro97] and (b) Flux of diffuse extragalactic photons [Res90].*

- high energy (HE) for γ-ray energy ranging from 30 MeV to 30 GeV;
- very high energy (VHE) for γ-ray energy ranging from 30 GeV to 30 TeV;
- ultra high energy (UHE) for γ-ray energy ranging from 30 TeV to 30 PeV;
- extremely high energy (EHE) for γ-ray energy above 30 PeV.

Although arbitrary with respect to their production mechanisms, this distinction does reflect the different interaction phenomena and the detection techniques of γ-rays.

While the lower band characterizes the region of nuclear γ-ray lines, the highest band corresponds to the maximum energy of the charged particles (and therefore also of the secondary γ-rays) that can be achieved in conventional cosmic ray acceleration scenarios.

VHE γ-rays can be used to probe fundamental physics at energy scales important for particle physics and beyond the reach of terrestrial accelerators, including the 100 GeV scale expected for Cold Dark Matter, the TeV scale at which SuperSymmetry may emerge and possibly the unification scale for the strong and electroweak forces.

1.2 Production processes of cosmic gamma rays

Gravity is the prime power source for high-energy particle emission by astrophysical objects, as it causes the collapse towards massive objects which fuels most of the processes involved in matter acceleration.

The gravitational collapse usually generates a rotating accretion disc with the presence of plasma jets outflowing perpendicularly to the accretion plane and strong magnetic fields, exhibited by many AGN sources and also by some stellar systems.

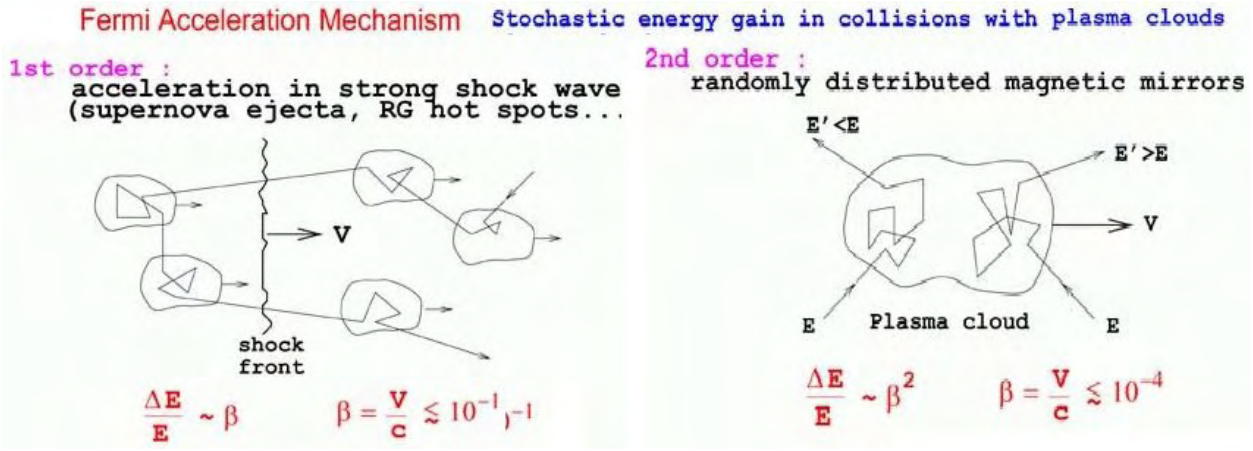

(a) (b)

Figure 1.4: *(a) Sketch of the Fermi acceleration mechanism at first and second order on charged particles by a shock front [TAR].*

It is currently believed that the particles with energy up to 10^{15} – 10^{16} eV are accelerated in galactic objects like SNR [Ame06], while the origin of particles with energies between the knee and the ankle can be various and the particles with energy above the ankle value originated most probably from extra-galactic sources [Sza94].

The acceleration of charged particles in accretion discs and jet structures, as well as in the external shells of SN, is related to the presence of strong shock waves.

The model, based on a mechanism first proposed by E. Fermi [Fer49] (see figure 1.4), has been elaborated taking into account the efficiency rates and the measured cosmic-ray spectrum [Bel78, Bla78] under the name of Diffusive Shock Acceleration.

It is worth noting that up to now no single source, either galactic or extra-galactic, has still been firmly identified as a cosmic-ray accelerator, even if the AUGER experiment recently showed some correlation between the arrival directions of cosmic rays with energy above 6×10^{19} eV and the position of some AGNs lying within 75 Mpc from the Milky Way [Abr07].

Charged particles, however accelerated, can transfer (part of) their energy to γ-rays by means of different radiation processes, some of which are of particular interest in the production of cosmic γ-rays, namely the *electron bremsstrahlung* (an important mechanism for the production of γ-rays inside the Galaxy), the *Inverse Compton scattering* (IC, one of the main production mechanism in sources) and the *Synchrotron Radiation* (SR, the principal emission mechanism from high energy particles in astrophysical situations).

Other primary γ photons can originate from π^0 decay (the major γ production mechanism in a hadronic environment) or from nuclear transitions; finally, it must be considered the possibility of obtaining characteristic photon signals also from annihilations or decay of heavy particles, either hadron pairs or baryonic resonances like the Δ family, or from the self-annihilation of the still unknown Dark Matter.

Two models for VHE γ-ray production are briefly recalled in the following; it is likely that both are active in astrophysical context.

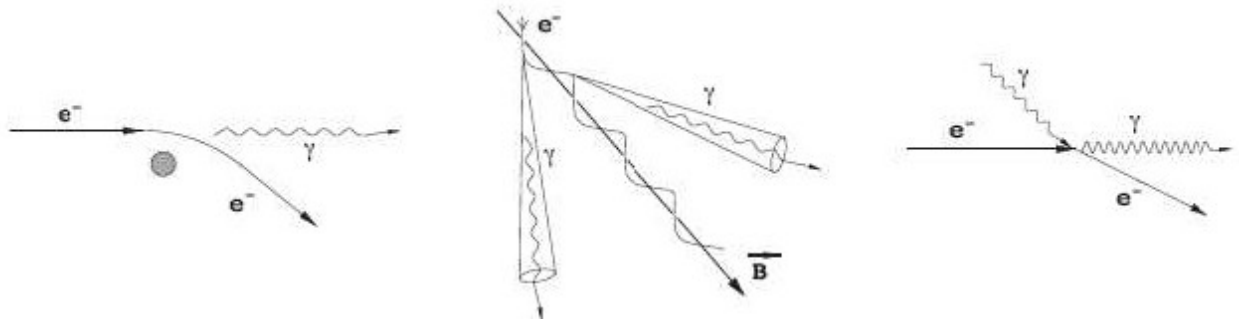

(a) (b) (c)

Figure 1.5: *Sketch of different γ radiation mechanisms: (a) bremsstrahlung emission, (b) Synchrotron Radiation and (c) Inverse Compton scattering.*

1.2.1 Leptonic Model

When a relativistic electron is moving inside a magnetic field H, the Lorentz force will bend the charged particle in a spiral path at a constant pitch angle θ, i.e. the angle formed between the electron velocity and the direction of the magnetic field H.

Due to the continuous acceleration towards the guiding center of its orbit, the electron will lose its energy emitting synchrotron radiation (SR) strongly beamed into a cone of angle $\alpha \sim m_e c^2/E$ (see figure 1.6.a), where m_e is the electron mass and E its energy. High-energy SR is produced only in astronomical regions with very strong magnetic fields, e.g. close to a neutron star surface (where $H \gtrsim 10^{12}$ G).

At relativistic energies the radiation occurs with a continuum spectral distibution peaked about ω_c (see figure 1.6.b), the critical frequency at which the maximum power is emitted, expressed as

$$\omega_c = (3/2)(eH_\perp/mc)\gamma^2 \sin\theta\,. \tag{1.1}$$

In typical galactic magnetic fields, the energy can be approximated by

$$E_\gamma \simeq 0.05\big(\frac{E_e}{\mathrm{TeV}}\big)^2\big(\frac{B}{3\,\mu\mathrm{G}}\big)\,\mathrm{eV} \tag{1.2}$$

In the case of AGNs, the SR relativistic electrons is responsible for the emission between the radio and X-ray bands.

For the ultrarelativistic electrons typically encountered in astrophysical situations, the emission spectrum below the cutoff assumes the power-law form

$$\frac{\mathrm{d}N_\gamma}{\mathrm{d}E_\gamma} \propto E_\gamma^{-\frac{q+1}{2}} \tag{1.3}$$

where q is the spectral index of the parent electron distribution[2].

[2]It is worth noting that proton SR is generally not a relevant process. For protons and electrons of the same energy, $E_p = E_e = E$, the energy loss rate of protons ($\mathrm{d}E/\mathrm{dt}$) is $(m_p/m_e)^4 \sim 10^{13}$ times lower than the energy loss rate of electrons. The corresponding critical frequency ω_c emitted by a proton is $(m_p/m_e)^3 \sim 6\times10^9$ times smaller than the critical frequency for an electron of the same energy. However, in extreme conditions (i.e. for energy values above 10^{18} eV), the synchrotron cooling time of protons can be comparable or even shorter than other time scales that characterize the acceleration and confinement regions of relativistic protons [Aha04].

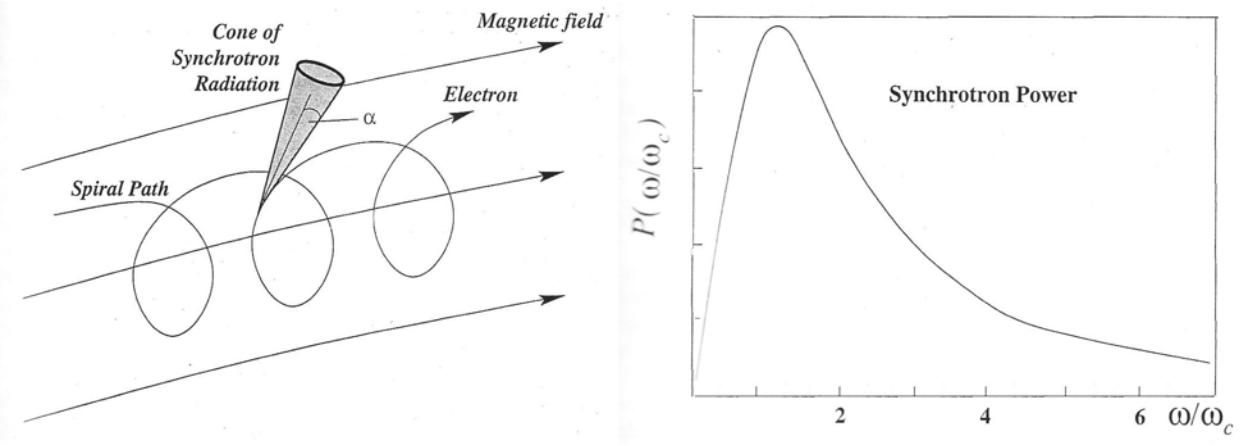

(a) (b)

Figure 1.6: *(a) The geometry of synchrotron emission from a charged particle in a magnetic field and (b) the power distribution as a function of critical frequency [Wee03a].*

The Compton scattering of photons on electrons ($e^-\gamma \rightarrow e^-\gamma'$) of low energy (at rest) results in an energy loss for the outcoming photon, while the scattering on energetic electrons may raise the photon energy (see figure 1.5.c): the process is then called *Inverse Compton* (IC) scattering, though the dynamics is the same in the two situations.

The scattered radiation has a continuous spectrum with a maximum at $\varepsilon'_{max} = 4\gamma^2 E_e$ (where E_e is the energy of the incident electron and ε' is the energy of the outcoming photon), corresponding to head-on collisions. The high dependence of ε' on the electron Lorentz factor γ ($\sim 10^2$ – 10^3) gives a possible increase of 10^4 – 10^6 times for the photon energy.

The IC scattering of photons on relativistic electrons is quoted for the VHE emission observed from the highest energy sources, like TeV blazars. IC scattering in SR sources is inevitable, since the synchrotron photons themselves become targets to be boosted to energies close to that of the radiating electrons [Hur94]. The combined action of SR and IC is the basis of the Synchrotron Self-Compton (SSC) models which reproduce the photon *Spectral Energy Distribution* (SED) of the highest energy sources observed.

In the simplest "one-component" SSC model, the same population of relativistic electrons emits SR and then scatters the produced photons up to higher energies: realistic models rely on more complex structures as multiple shells.

Typical multi-wavelength SSC spectra show a two-peaked profile, like two power-law emissions joint at break energies (see figure 1.7.a), with the Compton component energy peaked in the GeV – TeV range. This behaviour has been verified with high accuracy on the Crab Nebula (see figure 1.7.b), a steady VHE gamma emitter in the Milky Way often used to calibrate VHE gamma instruments, as well as on many AGNs.

Following SSC models, if the photons produced by the SR in a given region can be described by a power law with spectral index p, in a first approximation the tails at the highest energies from both SR and IC mechanisms will have a spectral index p.

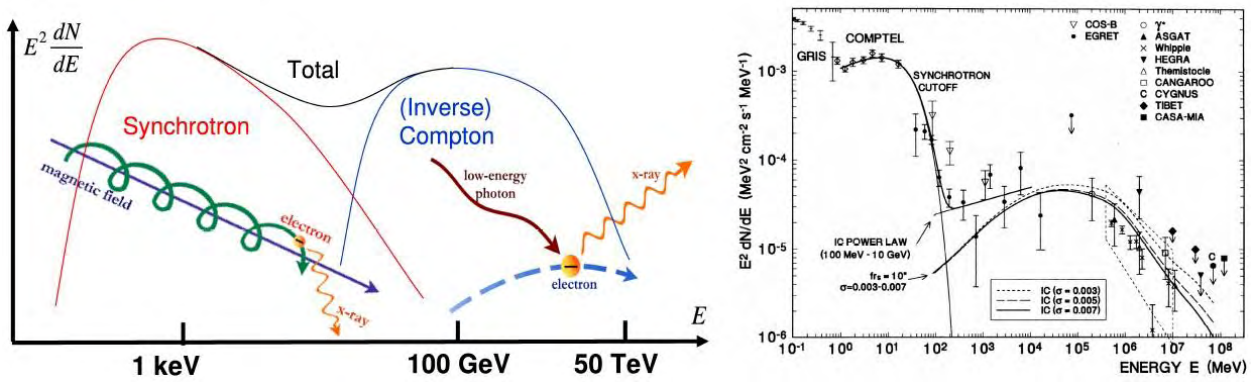

(a) (b)

Figure 1.7: *(a) A sketch of the differential energy spectrum of photons in the SSC model [Ang08c]; (b) The Spectral Energy Distribution (SED) of the Crab Nebula as deduced from experimental data [dJ96].*

1.2.2 Hadronic models

The interaction of relativistic protons with interstellar medium matter or radiation produces hadronic cascades, made mainly of pions (π mesons); as π^0 and $\pi^\pm$ are produced with the same probability, on average one pion out of three is neutral and subject to decay electromagnetically in two γ photons: $p\,X \rightarrow \pi^0 X \rightarrow \gamma\,\gamma\,X$, where X represents other secondary particles.

A pion at rest decays in two γ-rays with an energy distribution peaking at a broad maximum at about 70 MeV (about half of the π^0 mass), while the photons generated from a π^0 decaying on flight with velocity $v = c\beta$ will have energy (in the laboratory frame):

$$\varepsilon = \frac{1}{2} m_\pi c^2 \frac{1 + \beta \cos\theta}{\sqrt{1-\beta^2}} \tag{1.4}$$

θ being the angle of the outcoming photon with respect to the π^0 direction. In principle, the energy spectrum of γ-rays produced by pion decay is distinguishable from those of electromagnetic origin.

Differently from neutral pions, $\pi^\pm$ decay weakly into muons and neutrinos. As an example, the production and decay of a positive pion can proceed along the following chain:

$$p + p \rightarrow \pi^+ + X \rightarrow \mu^+ + \nu_\mu + X \rightarrow e^+ + \nu_e + \bar{\nu_\mu} + \nu_\mu + X \tag{1.5}$$

Although there is firm evidence on production of VHE gammas through leptonic mechanisms, the evidence for hadronic components is still marginal. The detection of neutrinos and gammas associated spectra would be a smoking-gun for a cosmic-ray (proton) accelerator.

1.3 The propagation of gamma rays through the interstellar medium

Gamma rays travelling from the cosmic source towards the observer can be absorbed by interstellar (or intergalactic) particles. A straightforward calculation shows that the absorption of VHE γ-rays by matter is negligible[3].

[3]To calculate the absorption probability of gamma-rays by galactic or extragalactic matter, consider a radiation length value of 38 $\mathrm{g \cdot cm^{-2}}$ and a cross section value of about $10^{-26}\,\mathrm{cm^2}$. Typical values for interstellar space or

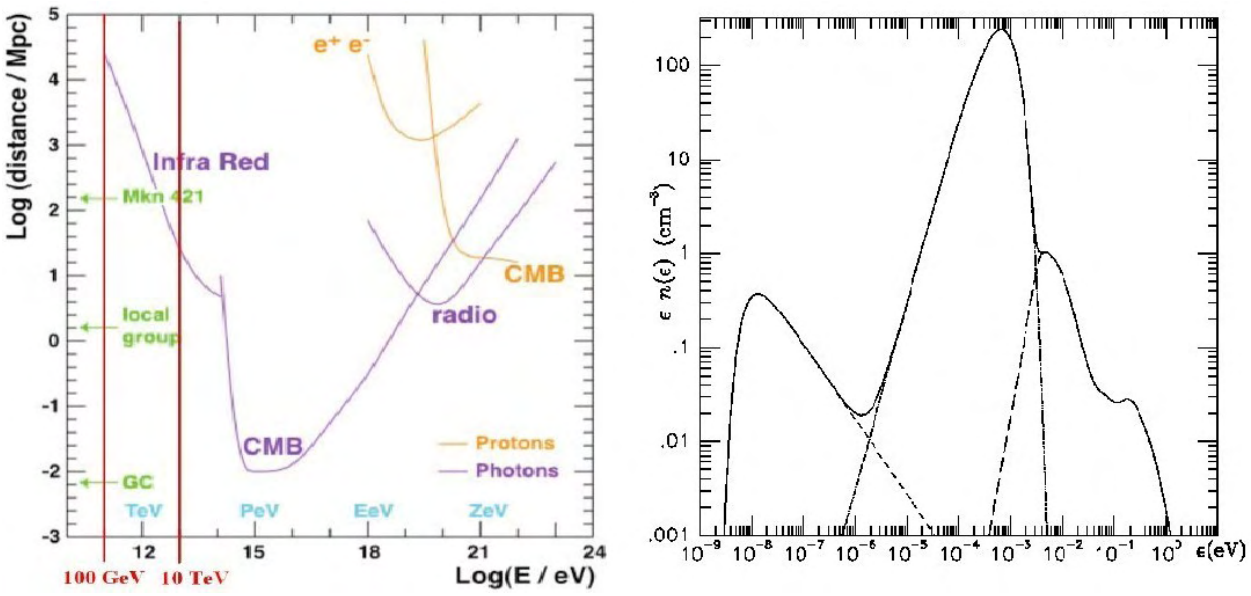

(a) (b)

Figure 1.8: *(a) Photon mean free path as a function of its energy (the interval between 100 GeV and 10 TeV corresponds to the bulk of VHE range) [Cop97] and (b) photon number density of the intergalactic radiation field at $z = 0$ [Lee98], composed by the radio background (short dashed line), the CMB (dense dotted line), and the infrared/optical/ultraviolet background (EBL) (long dashed line).*

On the contrary, the *Extragalactic Background Light* (EBL) low-energy photons turn out to produce an opacity of the Universe, which increases with the γ-rays energy and is expected to fade and even hide the farthest energetic gamma sources.

In more detail, the reaction considered is $\gamma\gamma_{(EBL)} \rightarrow e^+e^-$, which can occur above the pair production threshold.

The corresponding cross-section is described by the Bethe-Heitler formula [Hei60], derived in a QED framework, i.e. without assumptions of astrophysical nature, in the form:

$$\sigma(E,\varepsilon) \simeq 1.25 \cdot 10^{-25}(1-\beta^2) \cdot \left[2\beta(\beta^2-2) + (3-\beta^4)\ln\left(\frac{1+\beta}{1-\beta}\right)\right] \text{cm}^2 \qquad (1.6)$$

where $\beta = \sqrt{1-(m_e c^2)^2/(E\cdot\varepsilon)}$, m_e being the value of the electron mass, E the energy of the (hard) incident photon and ε that of the (soft) background photon.

The cross section in 1.6 is maximized when $\varepsilon\,(\text{eV}) \simeq 500\,\text{GeV/E}$. For instance, if $E = 1$ TeV, the interaction cross section is maximal for $\varepsilon \simeq 0.5$ eV, corresponding to a near-infrared EBL photon.

VHE γ-rays then interact mainly with optical or infrared photons, while the interaction with the CMB photons becomes dominant at $E_\gamma \sim 1$ PeV.

intergalactic space densities are $\sim 1\,\text{atom/cm}^3$ and $\sim 10^{-5}\,\text{atom/cm}^3$ respectively, while their characteristic distance scales are 10^4 ly and 10^8 ly, respectively. As typical atomic masses are order of 10^{-24} g, direct inspection shows that the total amount of matter encountered by gammas traveling from sources at these distances is much less than a radiation length.

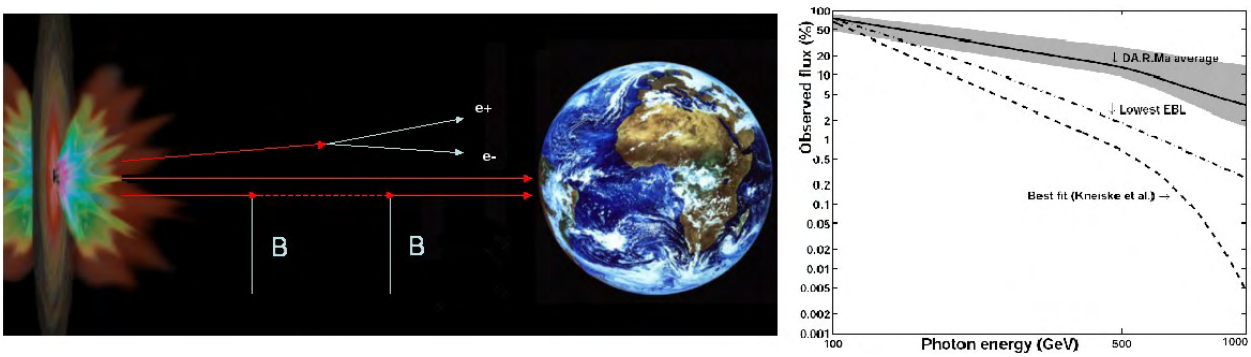

(a) (b)

Figure 1.9: *(a) A sketch of the DARMA oscillation mechanism [Ang08a] and (b) its prediction for the fraction of photons surviving to a travel distance equivalent to that of 3C 279, compared with the "best-fit model" of EBL (dashed line) and the minimum EBL density compatible with cosmology [Kne04].*

EBL is the light emitted from the stars and galaxies since the beginning of their existence. A direct measurement of EBL implies large uncertainties when accounting for Solar System and Galaxy light emission, while a thorough analysis of the γ-ray emission of distant extragalactic objects results in stronger constraints [Maz07a, Maz07b].

The absorption features imprinted on the γ-ray spectra by interaction of TeV photons with EBL carry information on both the evolution of baryonic components of galaxies and the structure of the Universe in the pre-galactic era.

The interaction of γ-rays with EBL produces an exponential cut-off in their spectra, usually expressed in the form $F_{obs} = F_0 e^{-\tau(E,z)}$, where $\tau(E,z)$ is called the *optical depth*, which turns out to be a function of the energy of the particle and its redshift (see e.g. [Ang08c]).

The *γ-ray horizon* (GRH, see [Bla03], also named *attenuation edge*, as in [Pri01]) for a photon of energy E is then defined as the distance corresponding to the redshift z for which $\tau(E,z) = 1$, i.e. the path length which attenuates the photon flux by a factor $1/e$.

The energy dependence of τ modifies the observed γ-ray SED with respect to the emission spectrum even for small differences in τ: as the absorption coefficient increases with energy in the region of interest, the observed SED results steeper than the emitted one.

The attenuation deduced by observed VHE spectra can be used to constrain the EBL density, as recently obtained from the detection of distant VHE sources with IACT telescopes [Aha06b, Maz07b].

On the other hand, once the Universe opacity to γ-rays is known, it becomes possible to calculate the unabsorbed intrinsic emission spectra of TeV sources and test the emission models.

The spectrum of sources with higher redshift is expected to be rapidly cut off by EBL absorption. This is in agreement with present observations: the EGRET satellite discovered 93 blazars with gamma emission in the range 100 MeV – 10 GeV, while only six sources with these features have been observed at energies above 300 GeV by ground-based telescopes, almost all with redshift values $z < 0.2$.

Nevertheless, it is worth noting that the recent observations of H.E.S.S. and MAGIC collaborations of distant TeV blazars [Aha06a, Tes07b] suggest that the intergalactic space could be more transparent to γ-rays than it was previously thought [Mad06, MAG08e].

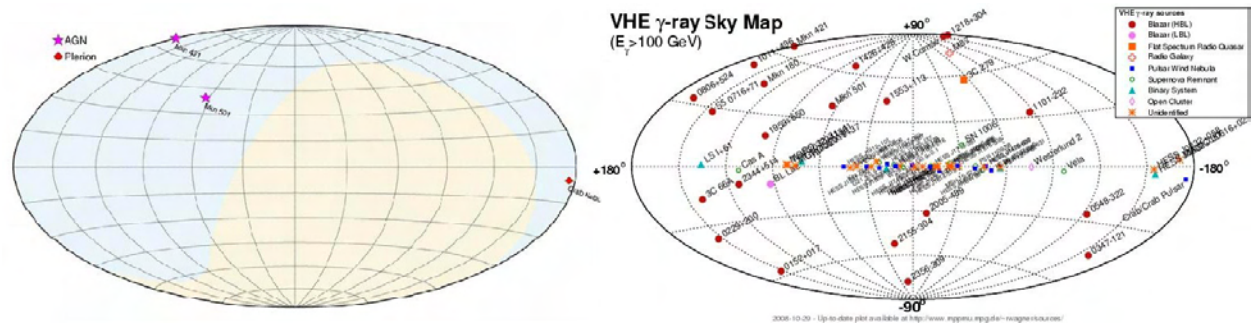

Figure 1.10: *A comparison between the known TeV gamma sources in 1996 and 2008 [TEV].*

Since these data do not easily match with a pure QED picture, different propagation processes besides the absorption mechanism just described have been proposed, which could eventually result in a change of present γ-ray propagation picture.

For instance, following the "DARMA" model [Man08, Ang08a], γ-rays might interact with very light axion-like particles, changing in that way the VHE γ-ray absorption length [Ang07, Ang08a] (see figure 1.9.a).

Differently from an interaction which invokes the conversion of photons into axion-like particles directly at the emission source [Sim08], the DARMA mechanism would be mediated by the intergalactic magnetic fields [Ang08b] and might contribute in enhancing the photon flux by a photon-axion oscillation (figure 1.9).

However, the whole topic of Universe transparency to γ-rays is still under debate, with recent contributions [Tav08, Ste08] which hold on different positions about the interpretation of the related experimental results.

1.4 Astrophysical sources of VHE gamma rays

In 1989 the Whipple collaboration discovered the first steady VHE γ-ray signal with large significance at TeV energies, coming from the Crab Nebula (also known as M1) [Wee89]; in 1992, VHE γ-ray emission was also detected from Mkn421 as the first extra-galactic source in this range [Pun92].

In the last decade, the use of new ground-based telescopes produced an impressive sequence of discoveries (see figure 1.10), raising the total number of VHE γ-ray sources to more than 80 in 2008, and the list is continuously and rapidly increasing (see also [TEV] for the latest update).

There are different kinds of γ-ray sources, but the large amount of energy emitted relates all of them to extreme physical events. A first distinction is between galactic and extragalactic sources. All extragalactic sources are point-like, but galactic ones can also be extended and diffuse.

Some highlights on typical observed sources are given in what follows, illustrated by recent results from the "MAGIC cornucopia".

1.4.1 Galactic sources

Most γ-ray sources within the Milky Way are remnants of ancient SN explosions, classified as SN I and SN II types depending on the amount of energy released: SN I can reach 10^{44} J, while SN II can emit emit up to 10^{46} J and sometimes leave a neutron star as relic.

The SNR spectra are interpreted as a superposition of SR emission from radio up to soft gamma wavelengths peaking at keV energies, and an IC part ranging from soft- to VHE-gamma energies,

according with the SSC model (see figure 1.7.a).

SNRs are classified into different types, namely shell-type SNRs, with no relic star inside the nebula, and Pulsar Wind Nebulae (PWN hereafter), where an inner substructure is observed, indicating the presence of a pulsar in the centre.

Pulsars are fast spinning neutron stars produced in SN II explosions. With their masses ranging from $1.4M_{\odot}$ to $3M_{\odot}$ and diameters of about 10 km, they are the densest known objects in the Universe (not considering Black Holes): their core density can reach 10^{15} g/cm^3 and they produce the strongest magnetic fields in the Universe, reaching values up to 10^{12} G.

About 1500 pulsars have been detected so far, out of which about 35 emitting in X-rays and 9 in γ-rays. The EGRET satellite discovered 7 pulsars with gamma emission above 100 MeV which all have counterparts at other wavelengths.

The Crab Nebula is a PWN originated by a SN that occurred in 1054 A.D. at a distance of about 2 kpc from the Solar System: it is one of the best studied non-thermal celestial objects on the whole electromagnetic spectrum, from 10^{-5} eV (radio waves) to nearly 10^{14} eV (γ-rays), commonly used for inter-calibration between different telescopes and to check the instrumental features and the analysis procedures.

The Crab Nebula spectrum from radio to γ-rays ($E < 1$ GeV) is interpreted as SR emission from relativistic electrons and positrons, while at higher energies it is dominated by IC γ-ray production (see figure 1.7.b).

There is little doubt that the engine of the nebula is the pulsar PSR B0531+21 (hereafter, Crab Pulsar), which is also a strong source of γ-rays detected up to 10 GeV.

The detection of pulsed γ-ray signals from the Crab pulsar above 25 GeV is an impressive result recently obtained by the MAGIC collaboration [MAG08f]: the pulse profile features measured impose strong constraints on the Crab pulsar emission model [Bar04, MAG08f].

Other interesting galactic γ-ray sources are binary systems, i.e. systems formed by a very massive object (neutron star, BH) accreting matter from a partner star (usually a blue giant or white dwarf) orbiting around them.

These binary systems show different characteristics and evolutions depending on the involved objects: in some cases (e.g. Cygnus X-1), the BH produces relativistic jets: this kind of system is also called *microquasar* (μQ).

An example of binary system is LS I +61 303, from which MAGIC recently detected a VHE γ-ray signal [MAG06, MAG08c]. This emission at TeV energies was found to have a period of ($\tau = 26.8 \pm 0.2$) days, close to the orbital period of the system.

A detailed multi-wavelength analysis of LS I +61 303 was also performed merging the MAGIC observations with the X-ray data from Chandra and those of MERLIN, e-EVN and VLBA arrays in the radiowaves, which resulted in tighter constraints on the morphology and emission mechanism of this high-mass X-ray binary system [MAG08a].

1.4.2 Extragalactic sources

1.4.2.1 Active Galactic Nuclei

Very few of the known galaxies show strong, variable and non-thermal emission from their inner cores, which are called *Active Galactic Nuclei* (AGN). The core mass for AGNs ranges from $10^6 M_{\odot}$ to $10^9 M_{\odot}$, concentrated in a region the size of the solar system. These central objects must be Super-Massive Black holes (SMBH hereafter): therefore, AGNs are special laboratories for extreme physics.

Depending on the observed features, AGNs have been classified into Seyfert galaxies, radio

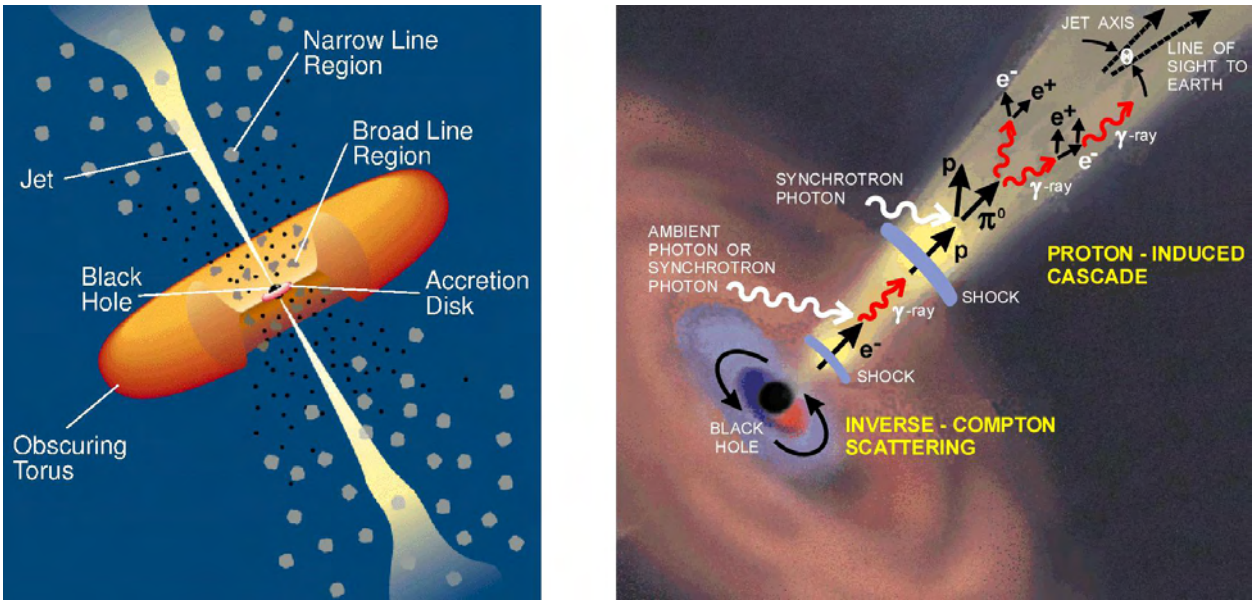

(a) (b)

Figure 1.11: *(a) Schematic view of the standard AGN unified model [Urr95]. (b) Particular of an AGN jet, with a sketch of SSC emission.*

galaxies, quasars, blazars and others (for a review, see e.g. [Kem99]). These objects show very variable fluxes, spanning from radio to the TeV range. The emission can grow by orders of magnitude with respect to the usual activity when the quasar is *flaring*.

A unified theory for all AGNs has been proposed [Urr95], which reduces the differences in the observed phenomena to the orientation of the source relative to our line of sight (see figure 1.11.a).

In this model, the central BH is surrounded by a rotating plasma accretion disc, which is heated up and emits from optical to X-ray wavelengths with a thermal spectrum peaked in X-ray band.

A thick dust obscuring torus, situated farther outside, absorbs the emission from the accretion disc and on its turn emits IR radiation; two narrow jets emerge from the BH perpendicularly to the disc plane and extend for several kiloparsecs.

The typical emission from a jet is non-thermal and fits the SSC model (see figure 1.11.b), spanning from radio-wave to γ-ray frequencies: the origin of such jets is one of the fundamental open issues in astrophysics.

When the jet is mostly aligned with the direction of observation, its emission dominates the spectrum, which changes drastically: the peculiar object resulting to the observer is known as a *blazar*.

Blazars are the most "active" kind of AGNs. Due to the polar view of the jet, the bulk relativistic motion of the emitting plasma causes radiation to be beamed in a forward direction, making the variability appear more rapid and the luminosity higher than in the rest frame due to the Lorentz dilation.

Firm VHE detections of AGN include at present about 20 blazars [Per08], the quasar 3C 279, and the radio galaxy M 87 [Aha03]).

The farthest VHE source currently detected is the blazar 3C 279, with $z = 0.536$, discovered in γ-rays by the *Compton Gamma-Ray Observatory* (CGRO) in 1990 [Har92], well-known for its

superluminal motion features and widely studied all over the e.m spectral range [Web90, Mar94, Har01].

An intense flare of 3C 279 (RA=$12^{h}56^{h}11.1^{s}$, Dec=$-5°47^{m}22^{s}$) was observed by MAGIC on February 23^{rd}, 2006. The VHE signal 3C 279 has been detected with a statistical significance 6.1σ for energies lower than 220 GeV and at 5.2σ within 220 and 600 GeV [Tes07b].

This source is being thoroughly analyzed in relation to the transparency of the Universe and the possible violations of the Lorentz invariance by means of the light dispersion (see also [MAG08d]) expected in some quantum gravity models [Ame98].

1.4.2.2 Gamma-Ray Bursts

Gamma-Ray Bursts (GRBs) are the most luminous electromagnetic events occurring in the universe [Wee03a]. They are flashes of gamma rays emanating from seemingly random places at random times. The duration of a GRB is typically a few seconds, but can range from few milliseconds to several minutes, and the initial burst is usually followed by a longer-lived "afterglow".

Most observed GRBs appear to be collimated emissions caused by the collapse of the core of a rapidly rotating, high-mass star into a black hole. A subclass of GRBs (the "short" bursts) appear to originate from a different process, most probably the merging of neutron stars orbiting in a binary system. All observed GRBs have originated from outside the Milky Way, though a related class of phenomena, the soft gamma repeated flares, are associated with galactic objects. The sources of most GRBs have been billions of light years away.

Although VHE gammas from GRBs are expected, only a couple of times up to now photons above 10 GeV have been detected from such sources; this might be due to instrumental limits.

1.5 The detection of cosmic gamma rays

As the Earth's atmosphere is opaque to γ-rays (see figure 1.1), the emission from high energy sources in the Universe can be investigated proceeding along two different experimental avenues:

- employing satellite-borne instruments, which can directly detect the primary radiation;
- employing ground-based instruments, which observe the effects of the interaction of γ-rays with the atmosphere.

The two classes of instruments are in some way complementary, both contributing to clarify the scenario of VHE γ-ray sources.

1.5.1 Satellite observations

Satellite-borne telescopes for HE γ-rays such as EGRET, AGILE and the *Fermi Gamma-ray Space telescope* (FGST, launched in June 2008, see figure 1.12.a) detect the primary photons at lower energies than ground-based telescopes; on the other hand, satellite detectors suffer from low sensitivity, due to their small effective area (about 1 m^2).

Since they are not constrained by night operation, satellite-borne instruments offer large duty cycles with a low rate of background events, but they are rather expensive.

The detection technology used on present orbiting γ-ray telescopes has been inherited from the EGRET instrument, which operated from 1991 to 2000 on board the CGRO.

An incident γ-ray is identified by its conversion into an e^+e^- pair induced in the foils of heavy materials alternated to the silicon planes which can detect the charged particles. The presence

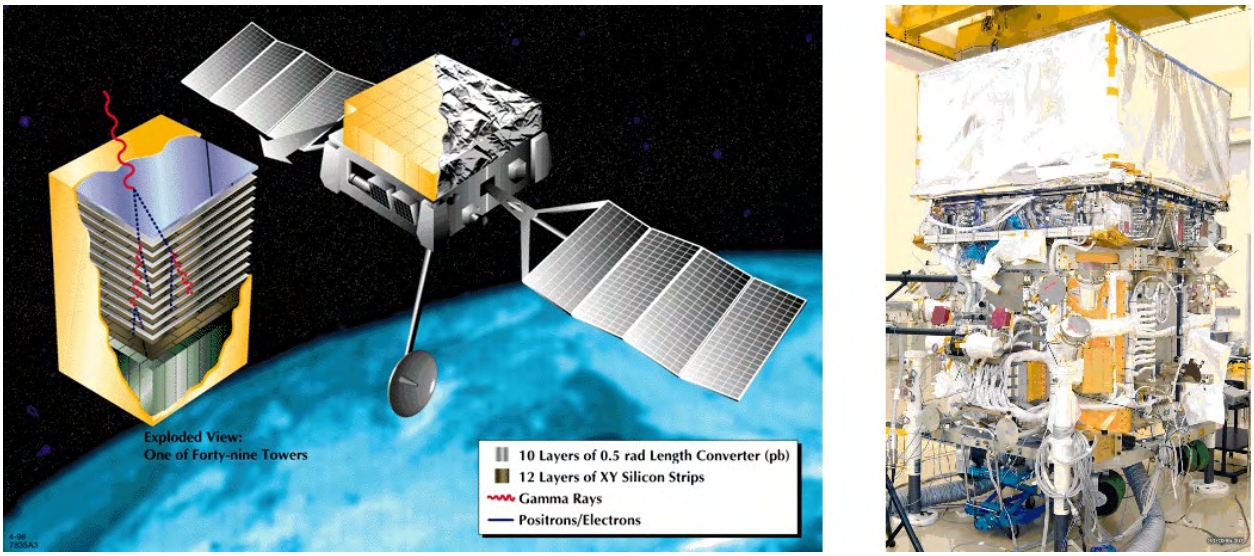

(a) (b)

Figure 1.12: *(a) The Fermi Gamma-ray Space Telescope [FGS]. (b) The LAT and GBM detectors.*

of an anti-coincidence veto around the detector rejects the noise signals from unwanted charged cosmic rays.

The angular resolution of these telescopes is limited by the opening angle of the e^+e^- pair and mostly by the multiple scattering of electrons and positrons inside the instrument.

Depending on the weight allowed on the satellite, a calorimeter in the bottom of the tracker can be used to improve the energy resolution, even if it rarely holds in the whole shower.

Since multiple scattering is the dominant process at low energies, the optimal detector design is a tradeoff between small radiation length (which decreases the conversion efficiency) and the large number of samplings (which increases the power consumption, limited by the problems of heat dissipation in space).

The main quality criteria for a satellite-borne detector are its effective area (i.e. the product of the area times the detection efficiency), the energy resolution, the space or angular resolution (also called point-spread function, PSF) and the time resolution.

FGST is composed of the spacecraft and two instruments: the Large Area Telescope (LAT) and the GLAST Burst Monitor (GBM): the two instruments are integrated and they work as a single observatory (see figure 1.12).

The structure of the LAT consists mainly in a tracker, an anticoincidence apparatus and a calorimeter: LAT can detect γ-rays with energies from 20 MeV to about 300 GeV, while the range explored by the GBM is 10 keV – 25 MeV.

The Fermi LAT outperforms EGRET by two orders of magnitude thanks to its effective area that approaches 1 m^2 (to be compared to 0.15 m^2 from EGRET) and its time resolution of 10 μs.

In the first months of activity, FGST already achieved important observations, like the discovery of a γ-ray radio-quiet pulsar within the CTA 1 SNR [Abd08].

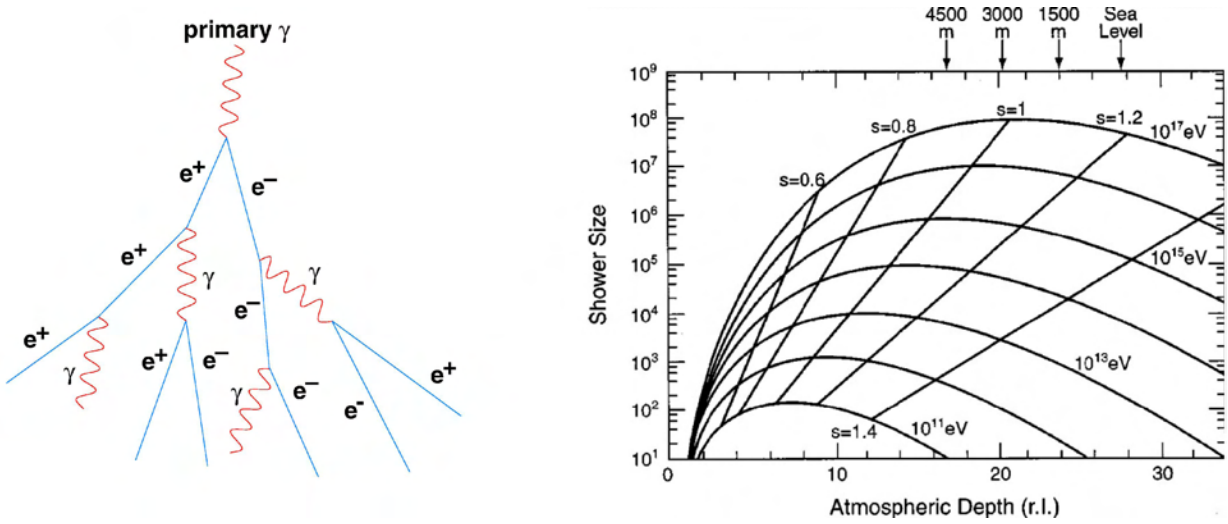

(a) (b)

Figure 1.13: *(a) Sketch of an air shower started by a cosmic γ-ray (electromagnetic shower). (b) Longitudinal shower development [Hof99a]. The parameter s describes the shower age, being 0 at first interaction, 1 at its maximum and 2 at its death [Ros41].*

1.5.2 Ground-based observations

VHE γ-rays of cosmic origin undergo destructive interactions with the nuclei in the Earth's atmosphere.

Low energy γ-rays interact with matter mostly via Compton scattering and photoelectric effect, while e^+e^- pair production dominates at energies above 10 MeV.

Incident γ-rays with energies over a threshold of about 10 GeV produce an atmospheric electromagnetic cascade (shower) dominated by the pair production and the bremsstrahlung mechanisms.

The development of an electromagnetic shower is a well-established theory [Ros41, Nis52], largely based on studies of calorimeters used as detectors in high energy physics experiments. The Earth's atmosphere can be considered a very deep electromagnetic calorimeter with approximately 30 radiation lengths of material (above sea level).

Nevertheless, ground-based instruments only record information about a small fraction of the total radiation and particle content of the shower, and they should be considered sampling calorimeters rather than total absorption calorimeters.

After a γ-ray converted in the atmosphere to form an e^+e^- pair, the secondary particles produce a new generation of γ-rays through bremsstrahlung. The characteristic distance scale for these interactions is called the radiation length X_0 and depends on the composition of the medium.

The radiation length is defined as the distance over which an electron's energy is reduced to $1/e$ of its initial energy by bremsstrahlung: X_0 is equal to 7/9 of the mean free path for pair creation.

Roughly speaking, in each radiation length a single particle (gamma or electron) produces two more particles that share its energy (see figure 1.13.a). This process generates an increasing number of electrons, positrons and photons in dependence of the atmospheric depth (see figure 1.14.a).

Eventually the average energy of the electrons and positrons drops to the point where the cross section for ionization losses exceeds those for bremsstrahlung, and the shower development begins to fall off as fewer electrons have sufficient energy to produce secondaries. The longitudinal

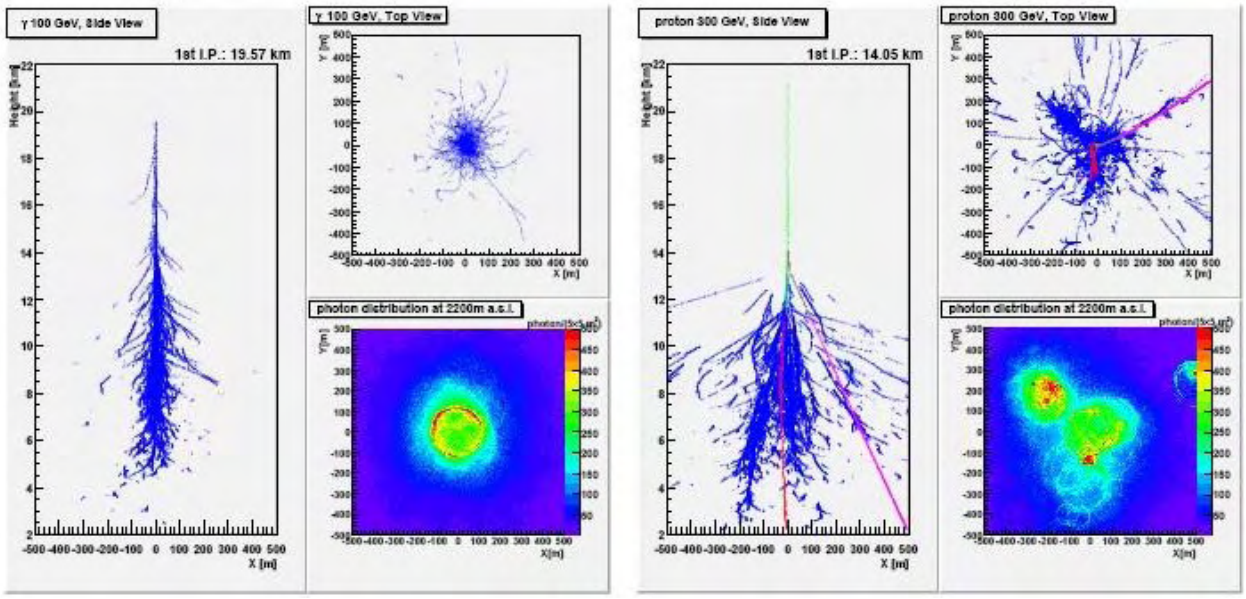

(a) (b)

Figure 1.14: *MonteCarlo simulated air showers induced by cosmic rays impinging on the atmosphere with a zenith angle $\alpha = 0^{\circ}$. The track colour code for the particles emitting Čerenkov photons is the following: blue for $e^{\pm}$, red or pink for $\mu^{\pm}$, green for hadrons (p, π^0, $\pi^{\pm}$). (a) A 100 GeV γ-ray initiated shower (the first interaction point of the primary particle is quoted on the top of the panel), in side and top view. (b) A 300 GeV proton induced air shower. The Čerenkov photon distribution at 2200 m a.s.l. is shown in the bottom right subpanel (the scale shows the number of photons in each 25 m^2 area) [Hay08].*

development of the shower is then related to the initial γ-ray energy (see figure 1.13.b).

This swarm of particles is called an *extensive air shower* (EAS). The EAS has a shape of a rough pancake gradually extending both laterally and longitudinally via multiple scattering as it approaches the ground. The central portion of the EAS is known as the core of the EAS. A typical EAS at the ground level may have a radius of 100 m (larger for higher energy primary γ-rays) and a thickness of 1 – 2 m (growing wider as the distance from the core increases).

The charged particles that comprise the EAS are traveling relativistically and therefore emit Čerenkov light[4] as they pass through the atmosphere.

[4]Čerenkov radiation occurs when a charged particle travels through a dielectric medium with a superluminal velocity, i.e. with $v > c/n$, where n is the refractive index of the medium.

When a charged particle passes through a dielectric medium, it interacts with the closest molecules inducing a temporary dipole polarization which causes them to radiate. In the case $v < c/n$, the disturbance is symmetrical around and along the particle trajectory, so there is no residual electric field and no detectable radiation. On the contrary, if $v > c/n$, all the molecules around the particles get an instant dipole except for the region ahead of the moving particle, because the particle travels faster than the emitted electromagnetic waves: a net polarization of the medium is produced along the particle track, which consequently radiates. The emitted wavefront propagates at an opening angle θ_C such that $\cos(\theta_C) = 1/(\beta n)$.

With reference to the Čerenkov light emitted by the electrons of an EAS, the value of the Čerenkov angle θ_C in air for $\beta = 1$ is about 1.3° at sea level, while at 8 km a.s.l. it is about 1°. The energy threshold at sea level is 21 MeV for a primary electron and 44 GeV for a primary muon.

Half of the emission occurs within 21 m of the shower axis (about 70 m for a proton shower).

Hadronic EAS (see figure 1.14.b) produce the main background for ground-based γ-ray observations. When a cosmic ray proton or nucleus collides with a nucleus in the Earth's atmosphere, it produces nuclear fragments and a number of pions with relatively large transverse momentum.

The neutral pions π^0 promptly decay to γ-rays, which in turn initiate electron-photon cascades. Charged pions decay to muons and neutrinos, following the reaction chain: $\pi^{\pm} \rightarrow \mu^{\pm}\nu_{\mu}$.

Although the mean life time of a muon is $\tau_{\mu} = 2.2\,\mu$s, energetic muons reach the ground level because of relativistic time dilation, giving rise to compact circular patches of Čherenkov light.

Since muons are roughly 200 times heavier than electrons, their trajectories are almost straight, as thay are not appreciably altered by multiple Coulomb scattering[5].

The different features of electromagnetic and hadronic air showers (see figure 1.14) are used to reject the much more abundant hadronic background in the electromagnetic shower studies.

To date two techniques have been successfully employed to detect VHE gamma rays from the ground: the *Extensive Air Shower Arrays* and the *Imaging Atmospheric Čerenkov Telescopes* (respectively, EASA and IACT hereafter).

Since the intrinsic angular spread of the charged particles in an electromagnetic shower is about 0.5°, the opening of the light cone is dominated by the Čerenkov angle. As a consequence, the ground area illuminated by Čerenkov photons from a shower of 1 TeV (the so-called "light pool" of the shower) has a radius of about 120 m. The height of maximal emission for a primary γ-ray of energy 1 TeV is approximately 8 km a.s.l., and about 150 photons per m^2 arrive at 2000 m a.s.l. in the visible frequencies. This dependence is not linear, being the yield of about 10 photons per square meter at 100 GeV, as illustrated in the left panel of the figure below.

The Čerenkov light is a thin front resulting in a pulse of duration 2 – 3 ns , with λ in the visible range and in the close UV, peaked on the blue for what is related to the visible part. The number of emitted Čerenkov photons per wavelength interval is proportional to $1/\lambda^2$, the wavelength dependent attenuation introduced by the atmosphere leads to a typical spectrum plotted in the right panel of the figure below.

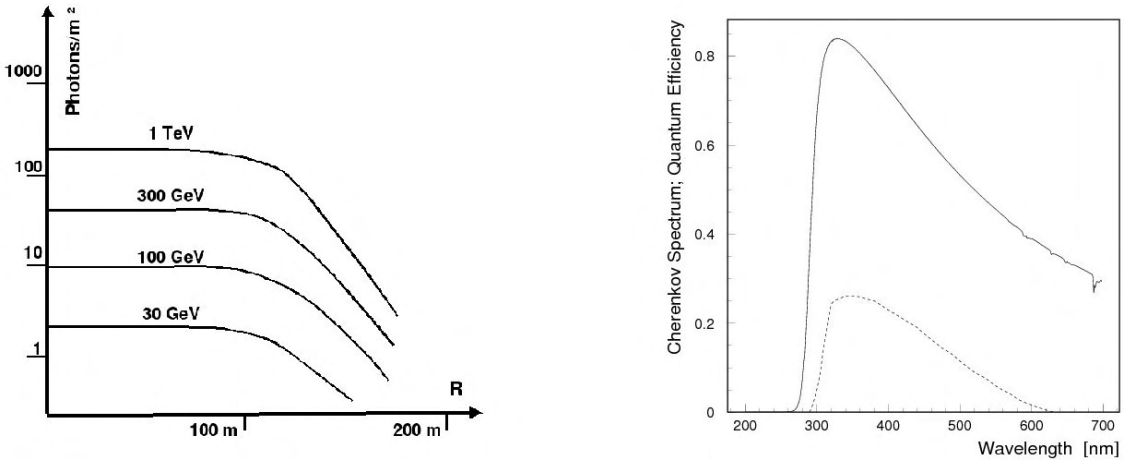

(a) (b)

(a) Density per square meter of Čerenkov photons between 300 and 600 nm as a function of distance R from the shower impact point for various photon energies as seen at 2 km a.s.l. for vertical showers [Ang08c]. (b) The typical spectrum of Čerenkov light (in arbitrary units) generated by vertical TeV air showers at the altitude of the MAGIC telescope, 2200 m asl. The quantum efficiency of typical photomultipliers [Doe01] is shown for comparison as a dashed line.

[5]The Čerenkov light emitted by these muons falls on cones of constant opening angle, producing typical rings or arcs when imaged in the focal plane of a telescope: this peculiar feature can be exploited experimentally (see paragraph 2.4). On the other hand, the very short arcs from muons with large impact parameters give rise to compact images that look very much like gamma rays, providing a further background for a single IACT.

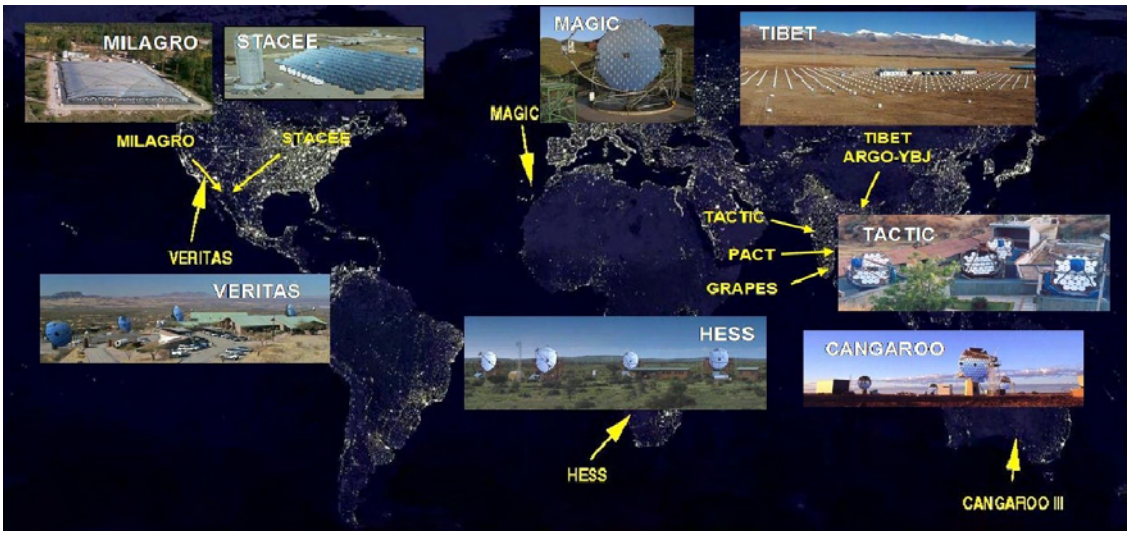

Figure 1.15: *Map of the most important ground-based γ-rays observatories [Hin07].*

(a) (b)

Figure 1.16: *(a) External view of the ARGO-JBY site and housing. (b) A glance to the "RPC-carpet", the EAS detector of ARGO [ARG].*

1.5.2.1 The Extensive Air Shower imaging technique

The EASA technique directly measures the passage of EAS particles. The direction of the primary particle is determined by measuring the relative arrival time of the EAS as it sweeps across the detector.

The direction and energy reconstruction of the primary particle requires that the shower core is contained within the detector, so that many measurements of the pulse height and arrival time can be made across the EAS.

This leads to the concept of the EAS array: a collection of charged particle detectors dispersed over a large area. Individual detectors may be wire chambers, scintillation detectors or water Čerenkov detectors. EASA have high duty cycle and a large FoV, but a low sensitivity.

A present example of EASA is the Italo-Chinese collaboration ARGO-JBY [ARG] (see figure 1.16), operating in Tibet, about 90 km from Lhasa, at 4100 m asl.

The ARGO detector arrays are made of *Resistive Plate Counters* (RPC), with energy threshold ranging from 0.5 TeV to 1 TeV. ARGO can detect the Crab Nebula with a significance of about 5σ (standard deviations) in 50 days of observation.

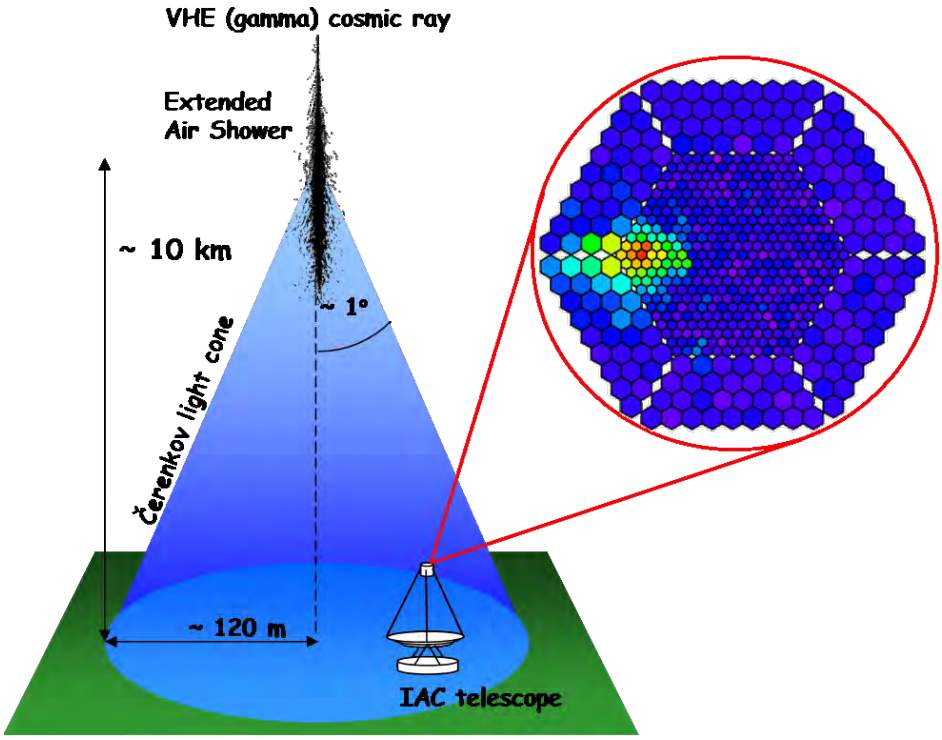

Figure 1.17: *The IAC technique at a glance, from the air shower generation to the image production.*

1.5.2.2 The Imaging Atmospheric Čerenkov technique

Čerenkov telescopes are not directly exposed to primary γ-rays: they detect the Čerenkov light produced by the charged components of the air shower originated by the incoming cosmic ray impinging on the atmosphere.

IACTs are currently the most efficient ground-based detectors of cosmic γ-rays [Lor03]. Like every tracking telescope, the IACT's design includes three basic elements, namely:

- a mechanical tracking system, to point and follow the source along its path in the sky;
- a reflecting surface, to collect the radiation and focus it on a receiver element;
- a specific detector, to convert the primary signal in a recordable image of the observed *field of view* (FoV).

As the Čerenkov light pool of a typical shower has a radius of about 100 m, a single telescope can have an effective collection area of 30000 m^2. Since about 10 photons per square meter arrive in the light pool for a primary photon of 100 GeV, a light collector of area 100 m^2 is sufficient to detect gamma-ray showers if placed at mountain-top altitudes.

The IACT collects a fraction of the Čerenkov light focusing it on a central detector (usually a set of PMTs) and converts the incident photons into electric pulses, which are elaborated to eventually form an image of the EAS (see figure 1.17).

The PMT set returns a rough image of the air shower, as Čerenkov photons emitted at different heights reach the telescope mirror dish with different angles and are therefore focused on the detector in different positions.

Figure 1.18: *The H.E.S.S. observatory, an example of Čerenkov telescope array [HES].*

The image thus brings information of the longitudinal development of the EAS, i.e. the number of particles emitting Čerenkov light as a function of their height in the atmosphere.

The Čerenkov light coming from the upper part of the shower is mapped closer to the detector centre, while the light emitted by the less energetic particles forming the "tail" of the shower originates the image part pointing away from the centre.

A detailed analysis of the shower "picture" taken with a IACT can be used to distinguish its origin (hadronic or γ-ray) and to extract relevant information about the primary cosmic particles. The parameterization of such images greatly improves the γ/hadron separation power and makes IACTs the most successful instrument for cosmic VHE γ-ray observations.

As the measurement of the Čerenkov light provides a good indicator of the energy absorbed in the atmosphere, the total amount of light contained in the image is one of the main estimators of the energy of the primary particle. In addition, orientation and shape of the image also provide information on the direction of the incoming primary particle.

An IACT is mainly characterized by its sensitivity, i.e. the minimum detectable γ-ray flux in a given number of observation hours (traditionally defined by a 5 σ excess in 50 hours of observation time) and by its energy threshold.

The energy threshold E_{th} of a IACT is usually defined as the peak value of the γ-ray energy distribution among the triggered events. It follows that E_{th} is spectrum dependent, even if it is often assumed to be a "Crab-like" spectrum, with a dependence $dN/dE \propto E^{-2.6}$. E_{th} is proportional to $\sqrt{B\Omega\Delta t/\epsilon \mathrm{A}}$ [Ong98], where B is the *night sky background* (NSB) photon flux, Ω is the solid angle subtended by a pixel (photosensor) of the detector, Δt is the integration time of the signals, A is the collection area of the mirror and ϵ is the light collection efficiency.

VERITAS, H.E.S.S. and CANGAROO, three of the "Big Four" IACT collaborations, make use of telescope arrays (see figure 1.18) to improve the overall performance since their original project, while the MAGIC team started its activity exploiting to its maximum the potential of a single telescope, building the largest collecting mirror and employing highly performant PMTs.

The first MAGIC telescope [MAG] is a good example of IACT with low E_{th}: its single-dish reflector allows the reconstruction of primary γ-rays above ~50 GeV (zenith angle dependent) with a sensitivity of 10^{-11} ph cm^{-2} s^{-1} (5σ in 50 hours of observation) and with an effective area of the order of 10^5 m^2.

The first light of a second telescope, essentially a clone of the original MAGIC, is planned for Spring 2009. It will operate in coincidence with the first telescope to improve the detection sensitivity of the system by a rough factor of three, decrease its energy threshold and significantly improve its angular and spectral resolutions (see section 3.4.2).

Chapter 2

The MAGIC telescope

The MAGIC (Major Atmosphere Gamma Imaging Čerenkov) telescope [Bar98, Fer05, Goe07a] is at present (2008) the IACT with the largest mirror dish and the lowest energy detection threshold in the world.

MAGIC is located on the Canary island of La Palma (28.75° N, 17.89° W) at 2225 m asl. The observation conditions on site are amongst the best in the world, even if occasional strong winds, winter snowfalls and high humidity demand a strong technical effort to prevent damaging and ageing of the telescope, which is too large to be protected by a dome.

2.1 The mechanical structure of MAGIC

2.1.1 The telescope frame

The reflector frame has been designed to fulfil at the same time the requirements of rigidity and lightweighting for fast repositioning. The frame, about 17 m in diameter, is a reticular structure in carbon fibre reinforced plastic (CFRP hereafter) tubes joint by aluminum knots weighing only 5.5 tons, out of a total weight of about 70 tons for the whole telescope (see figure 2.1.b). The CFRP construction is about three times stiffer and three times lighter than an equivalent steel construction.

A single aluminum tubular arc, reinforced with steel stressor cables, holds the PMT detector (camera hereafter) in the focus position 17 m away from the reflector. The weight of the camera is around half a ton, and the small bending of the arc, unavoidable during the telescope tracking, is corrected via re-orientation of the mirror.

The overall structure [Bre08], with an alt-azimuthal design, can rotate in azimuth up to 400^o along a circular rail of 9.5 m radius on six bogeys, pushed by two synchronous motors (Bosch Rexroth MHD 112C-058) used together with low-play planetary gears linked to the sprocket wheels. A third motor controls the altitude movement of the CRFP frame, the nominal power consumption of each motor being about 11 kW.

The angular positions are controlled by three shaft encoders (HENGSTLER type AC61): they are multiturn encoders with an angular resolution of 1.3 arcmin per step.

The light CFRP structure allows the telescope to react effectively to alerts from the GCN rapidly pointing to the GRB coordinates. During the fast authomatic (re)positioning which follows such alerts, the maximum angular speed is $\omega = 70.4$ mrad/s, while the maximum acceleration is set to $\alpha = 11.7\,\mathrm{mrad/s^2}$.

Eventually the telescope can turn by 180° in azimuth in less than 45 s, at the same time

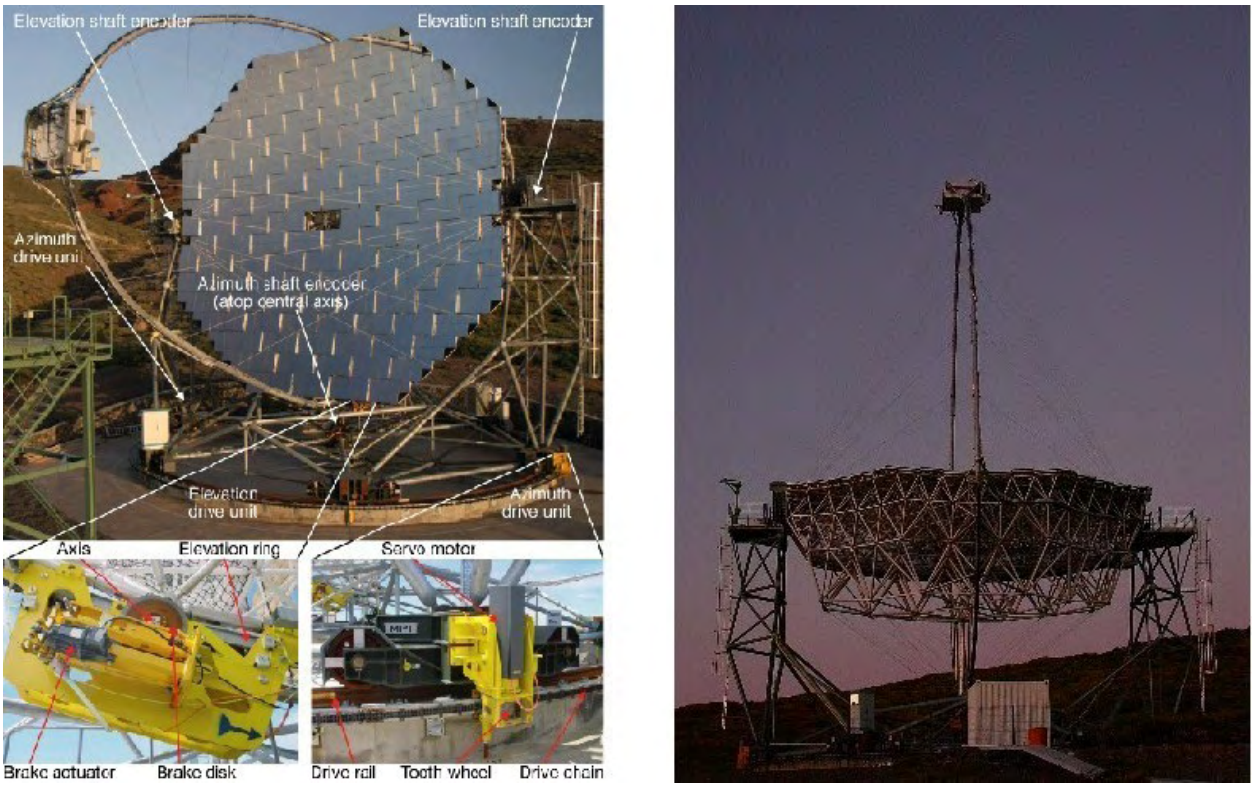

(a) (b)

Figure 2.1: *(a) Overall view of the MAGIC telescope, with zoomed views on the motors [Bre08]. (b) The MAGIC clone in vertical position: the bearing structure and the reflector frame are clearly visible.*

modifying its altitude and shape [Bil07] to match with the new target: the possibility of observing also in the so-called "reverse mode" allows the instrument to be repositioned at any point in the sky within 22 s.

2.1.2 The pointing system

Imperfections of the telescope mechanics such as the inexact alignment of the axes or deformations of the structure result in slight deviations from the position nominally pointed.

A pointing model which parametrizes these deviations has been created using the images of bright stars in the focal plane: it is based on the TPOINT^{TM} telescope modeling software [Wal05] used also for optical telescopes, .

The "T-point images" are taken with a high sensitivity CCD camera (Watec type WAT-902H) whenever possible during the observational dead-times (moontime, twilight...). Each T-point displays the spot of a star down to magnitude $m_V = 4$ reflected on a screen together with a ring of reference LEDs which define the position of the camera centre. (see figure 2.2.a).

The calibration of the model by mispointing measurements of bright stars is a standard procedure, which allows to determine the necessary corrections to the nominal pointing: the model is thenapplied on-line.

A starguider camera, mounted at the centre (offset by 1 m) of the reflector, monitors the positioning of the telescope and allows off-line corrections to the data by viewing both the camera

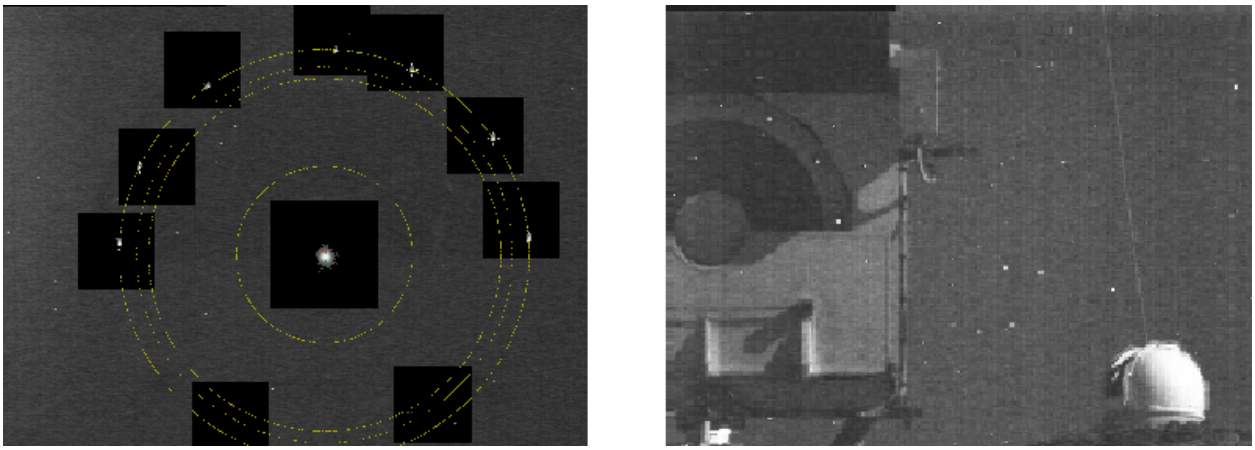

(a) (b)

Figure 2.2: *(a) A Tpoint image for the calibration of the pointing model. The image shows seven reference LEDs, as well as their reconstructed centre of gravity and location circle. Other LEDs on the bottom part are hidden by the lower lid, which holds a screen in front of the camera during Tpoint measurements. [Bre08]. (b) A sky star-field shot taken with the starguider camera. The W. Herschel Telescope's dome and laser are visible in the background (image credit: D. Dorner).*

of the telescope and the corresponding section of the sky star-field. (see figure 2.2.b).

Once the mispointing, i.e. the difference between nominal and actual pointing direction of the telescope, has been calculated by a comparison between the starfield around the pointing position and the reference stars in a catalogue, the position of a star can be determined within 1 arcsec and that of the camera centre within 2 arcsec.

More details on the (re)positioning and tracking procedures, on the tracking accuracy and on the system calibration can be found in [Bre06, Bre08].

2.1.3 The telescope reflector

The 17 m Ø reflector ($f/D = 1$) follows a parabolic profile which was chosen to preserve the temporal structure of the shower light flashes. The reflector is tessellated and composed by 956 mirrors, for a total area of 234 m^2.

Each mirror consists of a 5 mm thick AlMgSi 1.0 reflecting squared plate ($l \simeq 50$ cm), diamond-milled with a spherical curvature of various radii to fit at best the overall paraboloidal profile of the reflector. The focal lengths of single mirror tiles are increased following their radial position in the dish, from 17 m at the centre to 18 m at the boundary.

The reflecting surface is protected by a thin layer of quartz against ageing and scratches; plates are glued onto a honeycomb inside a thin aluminum box, giving a total weight of 3 kg for each mirror.

A heating wire mesh is embedded in the sandwich to dry the mirror surface in case of dew or ice deposits, the total power consumption for heating the entire reflector being 40 kW.

The mirrors are grouped on supporting panels four by four (three in some peripheral positions) and each panel can be moved by the Active Mirror Control system (AMC hereafter) described in the following. The panels are arranged in a chessboard pattern (see figure 2.3.a) to prevent them from touching each other when the AMC adjusts them.

Two mirror panels at the centre of the reflector are replaced by a suite of calibration instruments

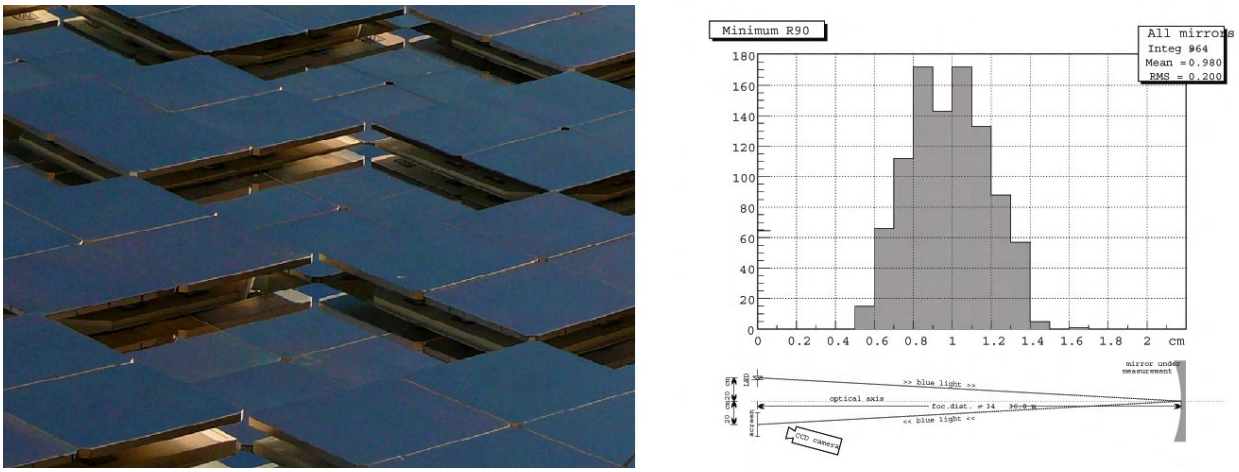

(a) (b)

Figure 2.3: *(a) Close-up of the MAGIC reflector showing the panel displacement. (b) The R_{90} distribution for all mirrors in the reflector and (below) a sketch of the instrumental setup to measure the PSF.*

including a light calibration box and several CCD cameras.

The point spread function (PSF hereafter) is expressed in terms of R_{90}, i.e. the radius of the spot which encompasses 90% of the light; all the component mirrors were checked in laboratory before their integration in the telescope, showing that 90% of the light from a parallel beam is focused within a circle of 1 cm diameter (see figure 2.3.b), well within the size of an inner pixel (1 inch diameter).

The reflectivity of the surface was measured on samples of mirrors already milled and coated with a spectrophotometer in the spectral region from 200 nm to 900 nm. In the range of interest (290 – 600 nm) the average reflectivity is 86% and never falls below 80%.

More details on the mirror production technique and the mirror optical quality and reflectivity can be found in [Dor08].

2.1.4 The Active Mirror Control

The AMC system [Bil07] was designed to correct small deformations of the mirror support dish during telescope positioning and tracking (see figure 2.4).

The mirror panels are connected to the support frame by a ball-and-socket joint and two actuators, which allow to adjust the panels with a precision better than 20 μm, corresponding to a displacement of the light spot at the camera of less than 1 mm.

Each panel is equipped with a guidance laser module to monitor its orientation with respect to the camera, which can be switched on to check the laser spot position by means of a CCD-camera situated close to the centre of the reflector.

The full system is calibrated each time the telescope is switched on, storing in a database the position of the laser spot for several stepping motor positions: when the telescope moves to a new target, the AMC authomatically adjusts the position of single mirrors to the new configuration.

Since this adjustment can be done for several panels in parallel, it takes less than 10 s and can be applied without interrupting the data-taking. Even in case of a fast repositioning of the telescope for a GRB alarm, the reflector can be adjusted while the telescope is slewing to the new orientation.

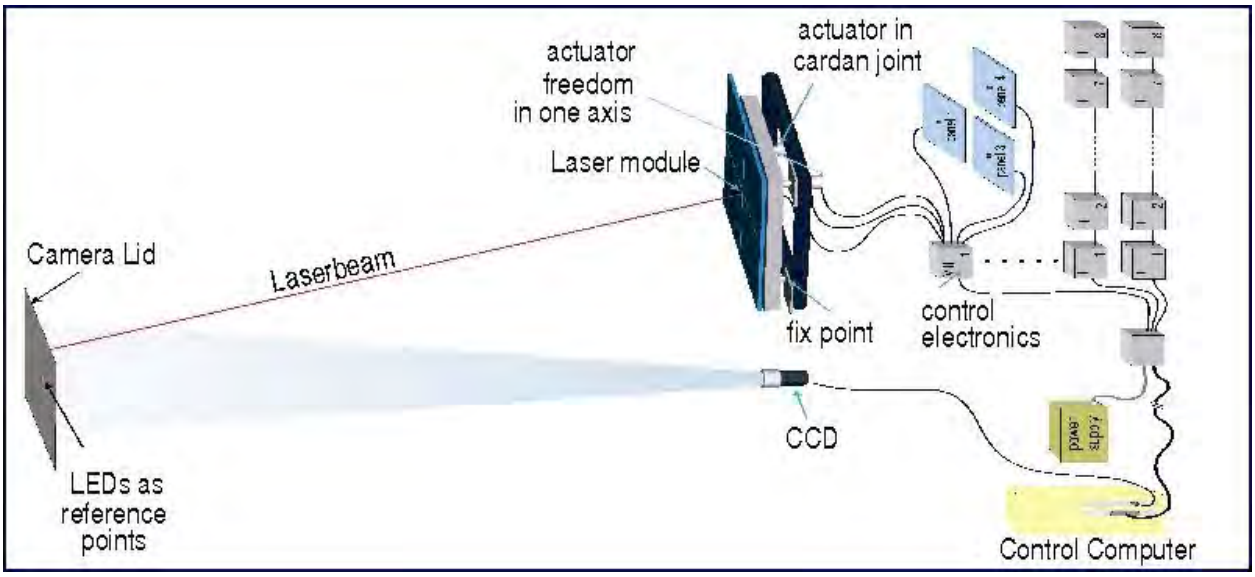

Figure 2.4: *Basic components of the AMC system [Bil07].*

The operative focusing length $f \sim 10$ km corresponds to the maximum distance of a shower produced with low zenith angle by a 100 GeV γ-ray. The focusing is set to infinity when the telescope is used in "star mode" to take T-points (see section 2.1.2), while in rest position the reflector is kept completely defocused to avoid accidental fires in the bush. After AMC adjustment, a pointlike source at a distance $f \sim 10$ km produces a gaussian image in the camera plane with $\sigma = 10.5$ mm.

2.2 The signal detection chain

2.2.1 The detector

The "heart" of the MAGIC telescope is the light detector called camera: it covers a hexagonally shaped area with side $l = 57$ cm, corresponding to a 3.6° Ø FoV (see figure 2.5).

The camera is housed is an aluminum cylinder of 1.5 m diameter, for a total weight (housing, PMTs and electronics) of about 500 kg; when operating, the camera electronics consume 800 W and are water-cooled.

Two lids, controlled by electrical motors independently powered with batteries, protect the camera from daylight and weather agents. A highly reflective disc, installed on the lower lid, is used to calibrate the AMC, to measure the mirror reflectivity and to check the alignment system (see also figure 2.2).

The camera front is equipped with hex-to-round light concentrators (Winston Cones) with high reflectivity (85 %), to reduce the dead detection area among the PMTs; a 2 mm thick plexiglas foil (type UG-218, with a UV cutoff around 290 nm) protects the PMTs and light collectors from bad weather conditions and hermetically seals the electronic sensors and camera elements from humidity and dust.

The camera is made of 576 photomultipliers (PMTs) developed by Electron Tubes in collaboration with the MPI Munich and the IFAE Barcelona on a specific design to cope with the requirements of the MAGIC Telescope.

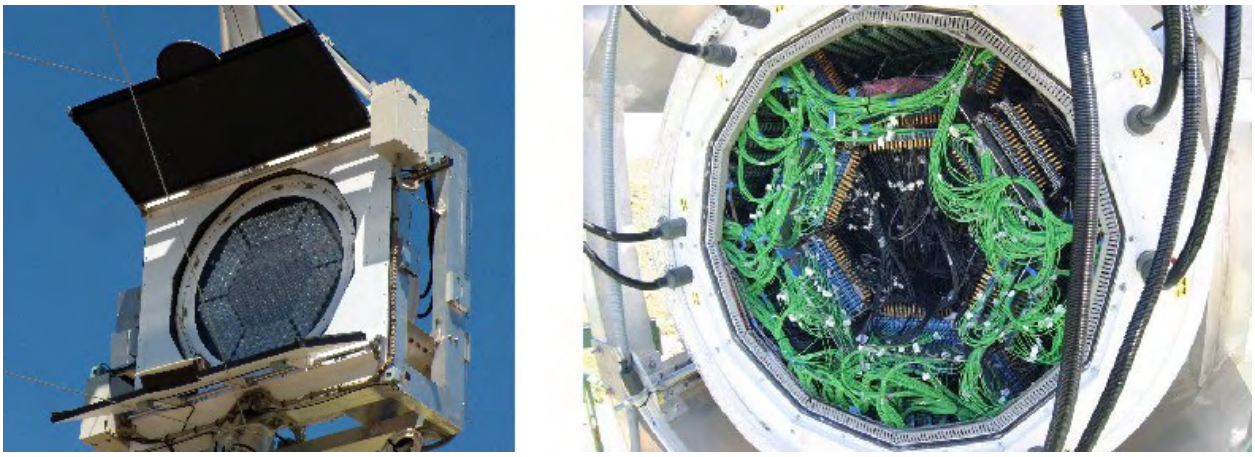

(a) (b)

Figure 2.5: *(a) Front view of the MAGIC camera: the shielding lids are open as in working condition, the hexagonal pattern of light concentrators is visible (image credit: R. Zanin). (b) Rear view of the PMT camera: the black lemo cables transport the PMT signals to the optical transmitter boxes, while the green optical fibers are bundled and exit the camera through the eight black pipes.*

More in detail, the PMT photocathode is hemispherical to enhance the probability of photon double crossing when using the appropriate light concentrators and the amplification stage has just 6 dynodes to give the low gain ($\sim 3 \cdot 10^4$) required for moontime observations.

The inner section of the camera, up to a radius corresponding to a FoV of 1.2°, consists of 396 1 inch PMTs (ET 9116A), surrounded by a ring of 180 1.5 inch PMTs (ET 9117B) [Ost00]. The photocathodes are bialkali with enhanced green sensitivity.

The original Quantum Efficiency (QE hereafter) of the PMTs (20% – 25% in the wavelength range between 330 nm and 470 nm) is enhanced by a diffuse lacquer doped with P-Terphenyl, which shifts the short wave UV component of the Čerenkov light into the spectral range of maximum sensitivity [Pan04], giving a milky aspect to the photocathodes (see figure 2.6.a).

The lacquer acts trapping the light close to the photocathode, this way enhancing its probability of being converted into photoelectrons, with a resulting QE peak around 30% at $\lambda = 400$ nm (see figure 2.6.b).

As the telescope is operated also in the presence of moonlight [MAG07], the PMT tubes were designed with only 6 dynodes, in order to avoid high fluxes of secondary electrons on the last dynodes, which would damage their surface when the telescope is exposed to strong light (up to seven times brighter than NSB).

In order to compensate for the low gain of the PMTs, the signals are amplified at the base by a 1 GHz bandwidth amplifier; it is worth noting that the amplifier noise is low enough to resolve single photolectron signals.

The high voltage supply can be tuned independently on the photocathode and on the last two dynodes of each PMT to adjust the gain.

Each PMT is assembled together with the amplifier electronics and the dynode voltage distribution electronics into a "camera pixel", which plugs directly into motherboards organized into camera sectors which route all the high and low voltages and DC control signals.

The PMTs produce signals with rise times as short as ∼700 ps and FWHM less than 1 – 1.2 ns, thereby allowing for an efficient coincidence trigger design, as well as an efficient suppression of NSB induced triggers.

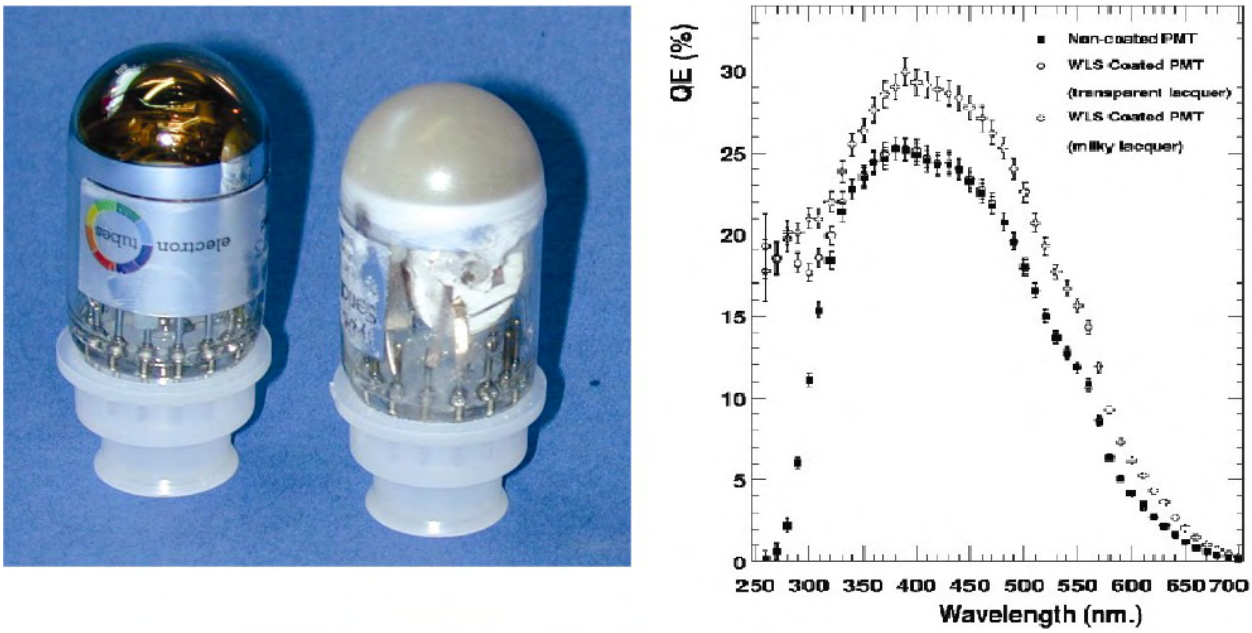

(a) (b)

Figure 2.6: *(a) A plain (left) ET9116A PMT and a PMT of the same model coated (right) with high concentration of "milky lacquer" (wavelength-shifter, WLS) [Pan04]. (b) The QE values measured as a function of the wavelength for an original PMT, for a PMT coated with a small concentration of WLS and with a high concentration of WLS [Pan04].*

The PMT signal is splitted close to the anode and integrated with a millisecond bandwidth to provide a DC readout of the anode current.

Differently from the other standard pixels of the MAGIC camera, at present the central pixel is equipped with a different PMT and a special setup designed to monitor the optical emission of pulsars [Luc05a, Luc08].

2.2.2 The signal transmission line

In order to keep the camera as light as possible and to reduce the electronic noise and the heat dissipation inside the detector, the trigger and readout electronics are displaced in the central data acquisition building, which is located about 100 m away from the telescope frame.

To avoid the attenuation and distortion of the PMT electrical signals along the transmission line, an optical transmission system [Lor02, Pan04] was adopted. The PMT pulses are transformed into light pulses by means of Vertical Cavity Surface Emitting Lasers (VCSELs hereafter) and coupled to multimode graded index fibers (50 μm Ø core, 125 μm Ø cladding). Figure 2.7.a shows two of the "transmitter boards", each of them hosting VCSELs for up to 18 PMTs.

After the 162 m travel along the optical fibers to the control house (the attenuation in the fiber is only about 0.3 dB/100 m at 500 MHz), the signals are reconverted into electrical pulses by PIN-diodes inside the "receiver boards", each of them hosting 8 channels; they are then split into two branches, one going to a discriminator (located in the same receiver board) which is part of the trigger system, the other to the FADC system, where the electric pulses are digitized.

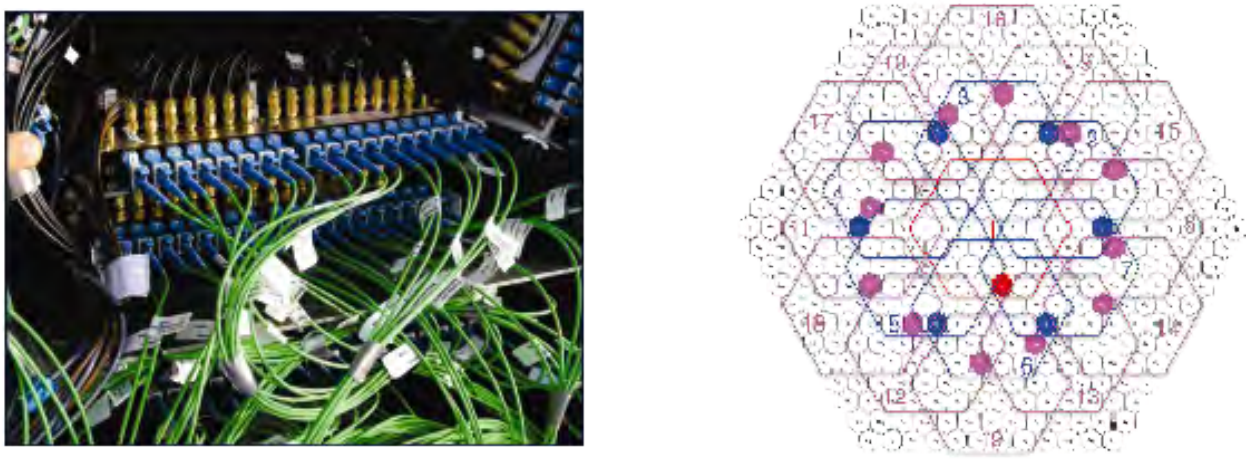

(a) (b)

Figure 2.7: *(a) Two of the transmitter boards installed inside the PMT camera. Each of the boards hosts 18 channels. The black "lemo" cables bring the electric pulses from the PMT bases. VCSELs inside the board convert the electric pulse into light pulses which transmitted to the readout electronics over the green 162 m long fibers which are also visible in the picture [Pan04]. (b) Definition of the trigger macrocells. The trigger area is restricted to the camera inner region. The trigger cells overlap to ensure an efficient coverage of all logic combinations of next neighbour pixels.*

2.2.3 The trigger system

The innermost 325 camera pixels define the trigger of the MAGIC telescope: this region is covered by 19 overlapping macrocells of 36 pixels each (see figure 2.7.b).

The trigger system [Bas01, Meu04] includes at present three stages: the discriminators (level 0) and the "level 1" and "level 2" (L1 and L2 hereafter) triggers.

The discriminators act on individual PMT signals, producing a square pulse of 6.0 ns width each time the PMT pulse exceeds the predefined threshold, which is usually set at 10 – 12 phe per pixel, depending on the NSB intensity, and can be modified also during the data acquisition if necessary.

A feedback program, the Individual Pixel Rate Control (IPRC hereafter), keeps under control the sharp signal raising of single pixels induced e.g. by the presence of bright stars in the FoV or by fast changes in the light background.

The L1 trigger looks for fast coincidences of next-neighbour (NN) pixels: the signals coming from the discriminators of the receiver boards are fed into the 19 L1 boards, each corresponding to a single macrocell.

The L1 boards use ALTERA EPLD128ATC100-7 Programmable Logic Devices (PLDs) to look for 2, 3, 4 or 5 neighbour pixels in tight time windows (4 ns of effective width) in any of the macrocells.

If the detected multiplicity is larger than 2, an additional condition is required for the signal to trigger: each candidate pixel must have at least two fired next-neighbours, giving a "closed-packed" configuration.

The L1 trigger is typically set to coincidences of 4 closed-packed pixels. Its response takes less than 80 ns, with a total time jitter in the order of 1 ns.

The L2 trigger then performs a "digital analysis" of the shower image, by applying topological cuts on the event (number of pixels, shape and orientation) to perform a true on-line image pattern

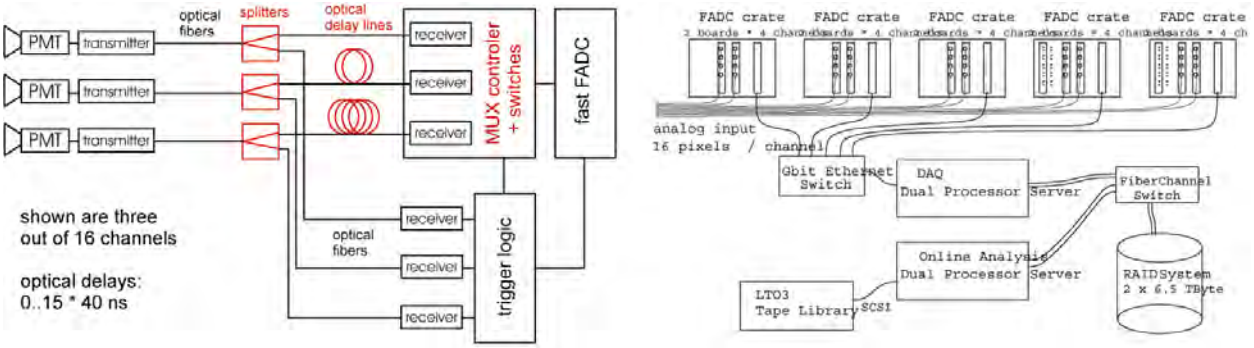

(a) (b)

Figure 2.8: *(a) Concept of the fiber-optic multiplexing technique [Goe07b]. (b) Schematics of MUX FADC data acquisition system [Goe07b].*

recognition. The L2 trigger decision takes less than 400 ns, increases the background rejection already at the trigger level and reduces the trigger rate to a value that can be processed by the Data Acquisition system (DAQ hereafter).

A different trigger system, called "sumtrigger", operates since 2007 in parallel with the L1/L2 triggers for a subset of the observation time on a reduced and different patching of the trigger area, optimizing the trigger sensitivity at γ-ray energies below 50 GeV for a point-like source at the camera centre.

It is worth noting that the sumtrigger recently allowed the first pulsed γ-ray detection with a ground-based telescope [MAG08h, MAG08f].

2.3 The readout system and data processing

The original data acquisition system (DAQ) of the MAGIC telescope [Goe03] was based on 300 MSample/s Flash analogic-to-digital converters (FADC hereafter), but in 2007 the digitization system was upgraded to a 2 GSamples/s FADC system [Goe07b].

The new readout system uses a novel fiber-optic multiplexing technique (MUX hereafter), which turned out to be effective as the signal duration (few ns) and the trigger frequency (typically around 1 kHz) result in a very low duty cycle for the digitizer.

The MUX technique results in a cost lower of about 85% than using one FADC per readout channel, the power consumption being also greatly reduced.

The MUX readout system uses a single 2 GSamples/s FADC to digitize 16 readout channels consecutively. The concept is illustrated in figure 2.8.a.

The analog signals are delayed using optical fibers in 16 channel delay boards. Each channel is delayed by 40 ns with respect to the previous channel. The signals are then electrically multiplexed and finally sent to the FADC. A trigger signal is generated using a fraction of the light, which is branched off by fiber-optic light splitters before the delay fibers.

The MUX output signals are then elaborated, digitized and sent to the central DAQ computer (MUXDAQ hereafter).

In the current readout system, a sustainable data acquisition rate of up to 100 MBytes/s, corresponding to a trigger rate of 1 kHz, has been achieved.

The disc storage system was designed using FiberChannel and Global File System (GFS) technology for high data acquisition rates and fast simultaneous access, in order to allow an online

analysis without disturbing the data acquisition(see figure 2.8.b).

The storage medium consists of two EUROstor RAID systems with 16 SATA discs, each capable of 500 GBytes. They are configured in RAID5. With one spare disc this amounts to 6.7 TBytes storage capacity per RAID system. The RAID systems are connected via two 2 GBit/s FiberChannel lines and a FiberChannel switch to the MUXDAQ. A maximum rate of 200 MBytes/s could be achieved writing data to a single RAID system.

In addition to the MUXDAQ, a second identical server, named MUXANA, is connected to the two RAID systems over the FiberChannel switch. In order to access the data simultaneously from both servers, GFS has been installed on the RAID systems. It provides a fast access to the data without interruption on the data taking, even at these high data rates.

MUXANA is used for quick data analysis, running the complete MAGIC analysis chain in a few hours. During one night up to 1 TB of raw data are recorded: this data volume exceeds the bandwidth of the Internet connection to the MAGIC data centre.

The raw data are therefore written to LTO3 tapes. Only the calibrated data generated by the quick analysis on MUXANA are transferred via Internet to the PIC data centre and become available to all the MAGIC collaborators within 24 hours after data taking.

The prompt detection of bright gamma ray sources is achieved by using a faster on-line analysis, at the cost of a reduced sensitivity (about 50% worse than the standard analysis for sources taken in wobble mode [Fom94]).

2.4 Performance of the MAGIC telescope

The present performance of the MAGIC telescope can be summarized as follows:

Positioning: the nominal accuracy of the 14-bit shaft encoders is about 1.3 arcmin. However, the intrinsic mechanical accuracy of the tracking system is determined comparing the position requested by the drive software and the feedback values from the shaft encoders: their difference being less than 10 arcsec for 80% of the time (well below the resolution of the shaft encoders), the actual accuracy of the motion control results much better than 1 arcmin.

Source tracking: the pointing accuracy is ultimately limited by the pointing model. As the star guiding system provides higher precision than the shaft encoders, the source tracking relies rather on this system. Once the nominal position has been corrected following the star guiding feedback, the tracking accuracy is almost ever less than 0.02° ($\sim$1.3 arcmin).

Timing: The clocks of all PCs are synchronized to UTC to an external internet time server. The absolute time for the telescope events is provided by a Rubidium clock which is corrected for long term drifts using GPS. With regard to the single pulse timing, the time resolution of the entire signal chain has been determined by means of calibrated events in 390 ps (see figure 2.9.a).

Reflectivity and PSF: The reflectivity and PSF of the whole reflector can be measured using stars imaged at the focal plane. The reflectivity of the mirrors in all wavelengths ranged between 80% and 85% for the entire period, with little degradation after 4 years of exposure to the atmosphere of La Palma.

The reflectivity and PSF of the reflector can also be estimated using cosmic muons [Goe05] on a more regular basis, giving a PSF estimate within 5% and an overall conversion efficiency estimate within 3% in a typical datataking night; the measured PSF stood in the range 12 ± 2 mm during the whole period of activity.

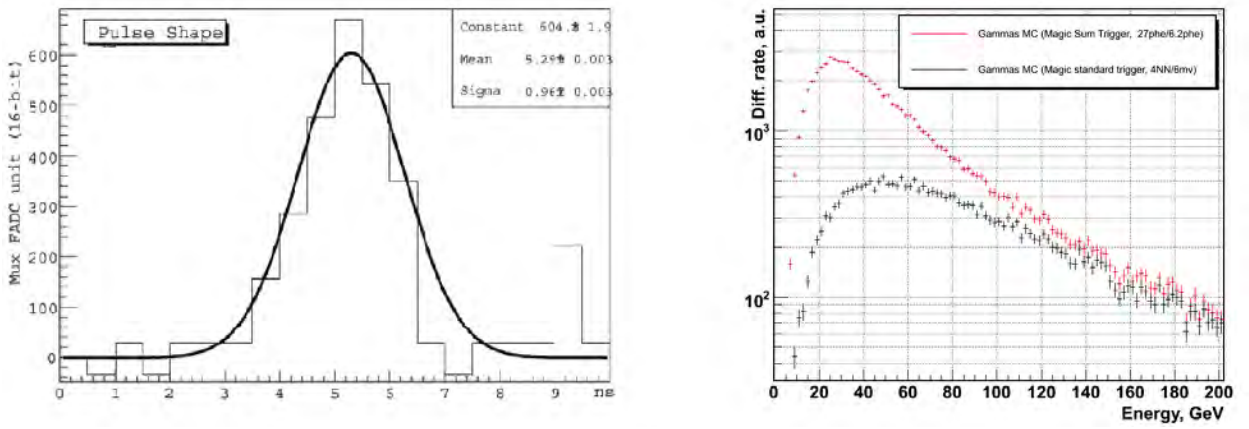

(a) (b)

Figure 2.9: *(a) A typical (∼5 photoelectrons) signal (histogram) and the mean scaled pulse shape of a single photoelectron signal [Goe07a]. (b) Differential rate of MonteCarlo simulated γ-rays fulfilling the sumtrigger and the L1 standard trigger conditions (4NN and 10 phe). The γ-ray sample was generated for low zenith angles and a Crab-like primary energy spectrum.*

Pixel calibration: the fine-tuning of the single pixels response (given in photo-electrons units, N_{phe}) to a homogeneous photon flux is possible by means of a calibration system. Once the camera has been "flatfielded" by software, $< N_{phe} >$ remains constant within 1% over a typical data taking sequence of one hour.

Trigger threshold: the individual pixel rate (IPR) is always dominated by accidental triggers produced by the NSB, but the L1 and L2 coincidence requirements among neigbour pixels sharply decrease the rate of triggers induced by NSB.

The threshold level is usually set to 32 counts for extragalactic fields of view, corresponding to about 10 phe integrated charge. The results of a full Monte Carlo simulation for vertically-incident γ-rays gave a trigger threshold value $E_{th} \simeq 55$ GeV for the standard L1 trigger, while the threshold energy obtained for a simulation of the sumtrigger electronics and a sum discriminator level of 26 phe is 25 GeV (see figure 2.9.b).

The discriminator thresholds and the level of the patches of the sumtrigger must be increased for bright fields of views where many background stars are present, for increased NSB and for moon observations (by as much as a factor 3).

The discriminator thresholds are set e.g. to 40 counts (i.e. about 12.5 phe) in a bright galactic field of view like the Crab Nebula.

Observation time: the datataking efficiency, defined as the ratio between the dark observation hours recorded versus the possible ones, together with the detailed dark or moonlight (and twilight) hours which have been recorded with the telescope during the first three years of regular operation (May 2005 – April 2008), are reported in table 2.1. Even if some technical problems resulted in a 5% to 10% loss on the total observation time, the total number of hours and the efficiency steadily improved every observational cycle, especially with regard to moon and twilight time, as the moon observation procedure has become easier and more sources get scheduled during moontime.

	Cycle 1	Cycle 2	Cycle 3
Dark observation time (hrs)	955	998	1109
Dark observation efficiency	60%	62%	67%
Moon observation time (hrs)	205	278	350
Total observation time (hrs)	1160	1276	1460

Table 2.1: *Data taking hours and efficiency versus the different cycles of activity of the MAGIC telescope. The first cycle started on June 2005, each cycle corresponds to 12 months.*

From a technical point of view, the MAGIC telescope has been an effective test bench for a large number of technical developments never applied before to IACTs and proved their reliability during regular operations according to the initial specifications, namely:

- the worldwide largest mirror dish (17 m Ø);
- the first carbon-plastic CFRP frame built for such a dish;
- the first use of diamond turned lightweight all-aluminum sandwich mirrors;
- the introduction of a novel AMC system to keep the correct dish profile during observations;
- the development of novel hemispherical PMTs with low gain and enhanced QE;
- the first use of optical-fiber transmission of the fast analog PMT signals over 160 m;
- the introduction of a novel technique (MUX) for fast digitization of the PMT pulses;
- the first use of single-quantum well LEDs driven by avalanche transistors for the calibration.

2.5 The new MAGIC-II stereoscopic system

2.5.1 Scientific and technical reasons for upgrading the MAGIC telescope

The first cycles of observations with MAGIC already gave relevant results, even on topics beyond the predicted ones. A further decrease in the energy threshold, together with improved energy and angular resolutions, hold the key for other unanswered physics questions.

MAGIC is at present the lowest threshold IACT operating in the world: higher performance will be obtained upgrading the telescope to a stereoscopic system by means of a twin telescope built 85 m aside MAGIC with advanced photon detectors and readout electronics.

The new MAGIC-II telescope system is designed to achieve an improved sensitivity and simultaneously lower the energy threshold operating in coincidence for stereoscopic observations.

All aspects of the wide physics program addressed by the MAGIC collaboration, ranging from fundamental physics to astrophysics and possible quantum astronomy extensions, will greatly benefit from an increased sensitivity of the observatory.

The expected lower energy threshold of MAGIC-II will have a strong impact on pulsar studies and extend the accessible redshift range, which is limited by the absorption of high energy γ-rays by EBL.

2.5.2 MAGIC-II interaction with other instruments

The thorough analysis of γ-ray sources requires multifrequency and multiapproach studies, as well as a full sky coverage.

MAGIC-II has straight access to synchronous dedicated optical observations, being associated with the KVA robotic optical telescope [KVA], situated next to the MAGIC site on La Palma: MAGIC-II is the only Čerenkov observatory with such a facility.

Besides standard UBVRI photometry, KVA will also be the only telescope in Europe with simultaneous polarimetric monitoring capability, a crucial asset in separating thermal and non-thermal contributions to the total flux.

A special synergy is also foreseen with the Fermi Gamma Space Telescope (FGST), which, being a survey instrument, has a large FoV and a very low background counting rate at energies above a few GeV.

Over its ten-year planned lifetime, FGST is predicted to discover thousands of new sources. However, its detections will be severely statistics-limited at energies above a few GeV, and the low photon detection rates will also affect the studies of short-term (hours or even minutes) variability in the same range.

MAGIC-II can overcome these limits with coordinate observations of the same sources.

Once the position of the sources discovered by FGST is given, MAGIC-II can deliver spectra above 30 GeV with higher accuracy and better time resolution for variability studies, thanks to its large collection area.

MAGIC-II and FGST are then complementary instruments in the overlap region, from 30 GeV to 300 GeV. The large overlap region also allows good cross-calibration, this way producing highly accurate spectra spanning an energy range of more than three orders of magnitude (from 100 MeV to 1 TeV, or wherever the sources cut off).

The new IACT array is also planned to be a significant step within the CTA project [CTA], which will allow the coordinate observation from different sites of the VHE γ-ray sky with unprecedented coverage, together with HESS [Hin04] in Namibia and VERITAS [Wee03b] in the USA as main partners.

2.6 The MAGIC-II telescope

The second MAGIC telescope is roughly designed as a clone: the experience made with the first one allowed a reduction in times and resources utilized in its building.

The lightweight CFRP frame, the drive system, the AMC and the signal optical conversion and transport are almost the same for both telescopes. Major changes involve the mirror, the camera and the electronics readout: new or improved components are employed whenever they offer greater reliability or reduce the overall cost.

2.6.1 The new mirrors

The mirrors of MAGIC are grouped four by four on 1 m^2 panels, which are adjusted by the AMC depending on the orientation of the telescope.

Differently from the first adopted solution, the second telescope will be equipped with larger 1 m^2 spherical mirrors consisting of one piece, reducing cost and installation efforts.

The new mirror tiles hav been produced using two different technologies [Bas07, Par08].

About 50% of them are all-Aluminum mirrors consisting of a sandwich of two 3 mm thick Al plates and a 65 mm thick Al honeycomb layer in the centre: they were produced by the LT Ultra-

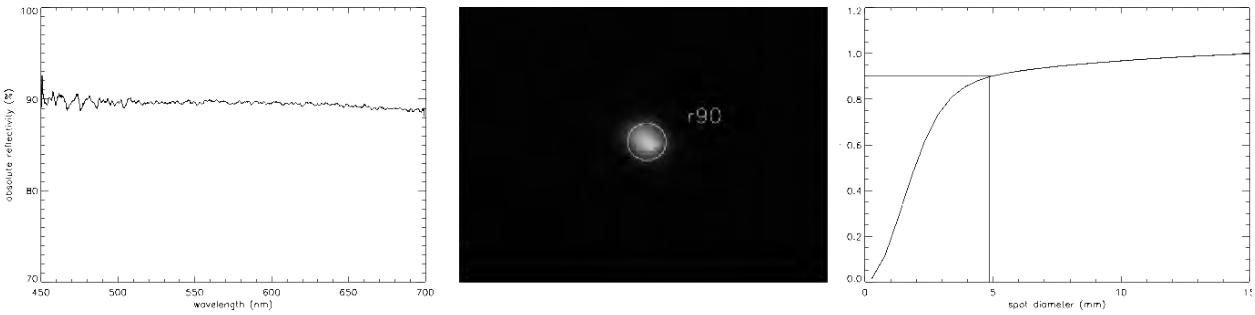

(a) (b) (c)

Figure 2.10: *(a) Test measurement of the reflectivity of a small portion of mirror before coating. (b) Spot image produced by a mirror on the focal plane. Since the picture is taken at twice the focal, the spot size is twice the actual one obtained when focusing light rays coming from infinity. (c) The distribution of the enclosed energy inside the spot [Bas07].*

Precision Technology GmbH in Germany [LTU] and now are mounted in the central area of the reflector.

Raw blanks are first bent into a spherical shape with roughly the final radius and then diamond-milling polished. After the polishing has been tested (see figure 2.10.a), front plates are coated with a quartz protective layer against scratches and ageing: the actual weight of each mirror is roughly 15 kg.

The measured reflectivity $refl$ and the radius R_{90} (i.e. the radius of the circle containing 90% of the spot light) hold the reference values $refl = 87\%$ and $R_{90} = 3$ mm (see figure 2.10).

The remaining 50% of mirrors were produced by Media Lario Technologies s.r.l. in Italy [MLT] using a less expensive procedure and now form the outer ring of the new reflector.

The reflecting surface of these tiles is obtained with the cold slumping technique [Par08]: a thin glass sheet (1 – 2 mm) is elastically shaped on a master with convex profile, then an Al-honeycomb structure is glued on the deformed glass sheet to provide the needed rigidity, ending with a second glass sheet glued on the honeycomb to obtain a 26 mm thick sandwich.

Once this support has been formed, a reflecting Aluminum layer and a thin protective quartz coating are deposited on the concave side. The typical weight of each panel is about 12 kg.

The glass-Al mirrors show a slightly worse performance with respect to the all-Al mirrors: on the other hand, the production of glass-Al mirrors is much cheaper (roughly 2000 €per panel) than the all-Al milling.

2.6.2 The new camera for the second telescope

The second camera of MAGIC-II [Hsu07] has an effective modular design: each seven pixels are grouped to form an hexagonal-shaped cluster, which can be easily plugged in the camera Al structure.

A cluster consists of 7 pixel modules and a cluster body which includes common control electronics, power distribution and a test-pulse generator. The PMTs are still coupled with the front side by Winston-cone light collectors to minimize the dead area between the PMTs.

This solution allows easy exchange of faulty clusters, as well as possibly full or partial upgrade when improved photodetectors will be available.

The two MAGIC cameras have the same 3.5° diameter, but that of the second telescope is formed with 1039 identical 0.1° FoV pixels in a round configuration: moreover, its trigger area is

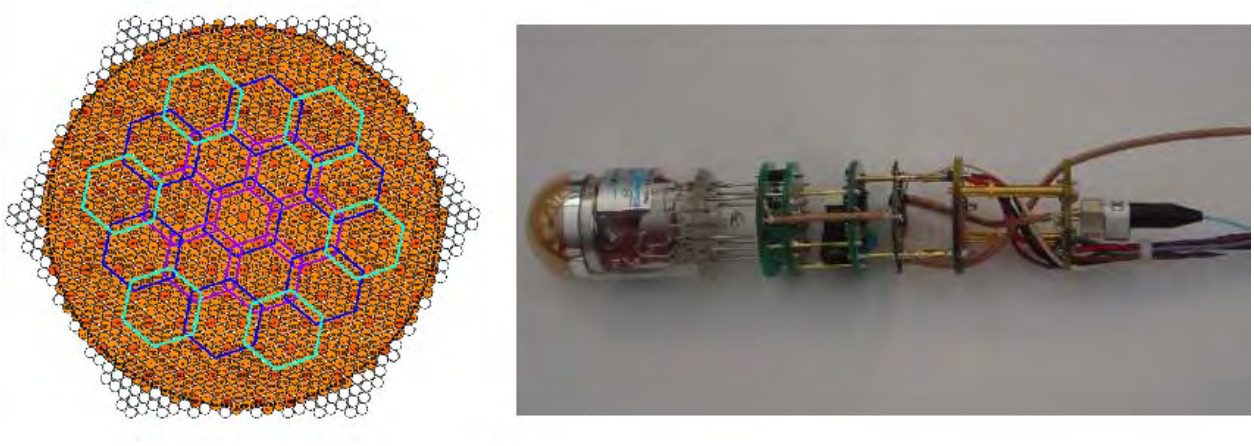

(a) (b)

Figure 2.11: *(a) Schematics of the MAGIC-II camera. Only colored pixels in a round configuration will be equipped. The hexagonal shapes indicate the trigger region [Goe07b]. (b) A single Hamamatsu R10408 PMT assembled with the front end electronics [Hsu07].*

increased compared to MAGIC (see figure 2.11.a).

To start with, the new PMTs made by Hamamatsu have larger QE [HAM], but upgrades with other kind of photodetectors are already planned[1].

The Hamamatsu R10408 6-stage photomultipliers with hemispherical photocathode reach a peak QE$\simeq$ 34% [Hsu07]. These PMTs have been favourably tested for low afterpulsing rates (typically 0.4%), fast signal response ($\sim$1 ns FWHM) and acceptable ageing properties.

Hamamatsu delivers PMT modules which include a socket with a Cockcroft-Walton type HV generator: the PMT socket and all the front-end analog electronics is assembled to form a compact pixel module (see figure 2.11.b).

In a second phase it is planned to replace the inner camera region with *Hybrid PhotoDetectors* (HPD hereafter) [Hsu07]. This kind of detector is featured by peak QE values of the order of 50% (see figure 2.12.a) and will significantly increase the sensitivity for low energy showers.

The development of new SiPM solid state detectors (see figure 2.12.b) is being actively studied [Tes07c], as alternative detector with even higher QE.

The flexible cluster design allows to test this new technology directly on the telescope without major interference with the rest of the camera. Upon successful test the whole central region of the camera will be equipped with HPDs.

2.6.3 New electronics for the second telescope

The newly developed MAGIC-II readout system performs ultra-fast sampling rates and low power consumption.

The entire signal chain from the PMTs to the FADCs is designed to have an overall bandwidth of at least 500 MHz, therefore allowing a minimum integration time[2] to reduce the influence of the NSB.

[1] An upgrade of the first camera to a photodetector's optimized configuration is also planned.

[2] It should be remembered that the Čerenkov pulses from γ-ray showers are very short (1–2 ns) and the overall parabolic shape of the reflector preserves the time structure of the light pulses. A precise measurement of the time structure of the γ-ray signal is already used by MAGIC to reduce the hadronic background [Tes07a].

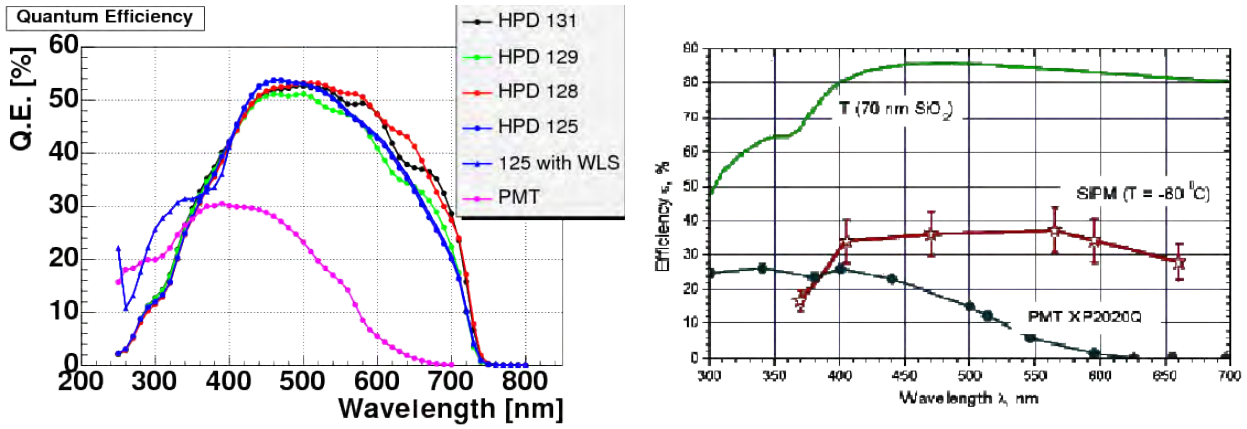

(a) (b)

Figure 2.12: *(a) QE curves of four HPDs without WLS coating, an HPD with WLS coating and a PMT with WLS coating. [Hsu07]. (b) The photodetection efficiency of SiPM of 25* $(5 \times 5)\,\mu\mathrm{m}^2$ *with micropixels size of* $(100 \times 100)\,\mu\mathrm{m}^2$ *(filling factor of 64%) at a temperature of 60°C is compared with that of a Photomultiplier [Tes07c].*

The signal transport from the camera to counting house follows the same process used by MAGIC.

The new 2 GSamples/s digitization and acquisition system is based upon a low-power analog sampler called *Domino Ring Sampler* (DRS hereafter) [Peg06].

The analog signals are stored in a multi-capacitor bank (1024 cells in DRS2) organized as a ring buffer: the single capacitors are sequentially enabled by a shift register driven by an internally generated 2 GHz clock locked to a common synchronization signal.

Once an external trigger has been received, the sampled signals in the ring buffer are read out at a lower frequency of 40 MHz and digitized with a 12 bits resolution ADC. The analog sampler, originally designed for the MEG experiment [MEG], has been successfully tested on site and showed a very good linearity and single photon discrimination capability.

A rough estimate of the data throughput for a 1 kHz trigger rate and a 2 GHz frequency sampling is of the order of 100 MBytes/s, a challenge for modern data transmission and storage solutions.

In MAGIC-II, the data are transferred to PCI memory via Gbit optical links using the CERN S-link protocol and then to the mass storage system.

2.6.4 The trigger for MAGIC-II

The trigger system of the second telescope is based on a compact next neighbour logic like the first telescope. However, the uniform camera design allows an increased trigger area of 2.5 ° diameter FoV (see figure 2.11.a), increasing the potential to study extended sources and to perform sky scans.

When MAGIC-II is operating in stereoscopic mode, a third level trigger (L3) is required to synchronize the signals coming from the two telescopes and apply the selection rules to constrain the stereoscopic information (see figure 2.13).

Whenever a shower hits a single telescope, its Ll 1 and L2 triggers generate a “pre-trigger” signal to hold the sampled waveform: if the triggered signal survives L3 level, the waveforms of

Figure 2.13: *The third level trigger (L3) operative scheme.*

both telescopes are digitized and read out. If there is no L3 validation, a feedback reset is sent to the single telescope DAQ after a given timeout.

Last, but not least, the introduction of L3 will reduce the overall trigger rate to a lower value affordable by the data acquisition system.

Chapter 3

Monte Carlo simulations for MAGIC-II

Nowadays, simulations based on Monte Carlo (MC) method are widely used in high energy physics to optimize the design of new detectors, to get accurate evaluations of their performance, to calibrate the experimental results.

In view of the upgrade to a stereoscopic system, a thorough MC simulation has been carried out to evaluate in detail the performance of MAGIC-II: the event simulation reproduces both the physics of the EAS and the telescope response.

This chapter illustrates the general characteristics of the simulation used for MAGIC-II, the principles of stereoscopic analysis and the first results obtained with a wide set of events generated to support the future experimental activity.

3.1 Simulation software for MAGIC-II

Three programs in cascade simulate the production of atmospheric showers, the reflection of Čerenkov light flashes on the mirror dishes and the response of MAGIC-II cameras to the signals.

3.1.1 CORSIKA

The CORSIKA (COsmic Ray SImulations for KAskade) software [Hec98] simulates in detail the evolution of an EAS initiated by photons, protons, nuclei, or any other particle in the atmosphere. The MAGIC-II simulation relies presently on CORSIKA 6.501 version.

The parameter values needed to steer the production of air showers are provided by the user to the program through an input card.

CORSIKA includes specific routines which simulate the transport of particles in the atmosphere and their decays and interactions with atmospheric nuclei. The atmosphere density distribution and the Earth's magnetic field are also considered in the simulation.

All particles are tracked along their path through the atmosphere and the program calculates type, energy, location, direction and arrival times of all the particles of the shower that reach a selected observation level, including the Čerenkov photons produced by the charged particles along their path.

CORSIKA is the most CPU-time expensive program of the simulation chain: in order to optimize the overall computing time, a peculiarity was introduced in present production for hadron induced showers. The same proton-induced events generated by CORSIKA are recorded as if they

reached the telescopes in 16 different positions: this solution allows a time reduction in the hadron's file production of a rough factor 15 with respect to single shower generation, at the cost of a minimum correlation in the output events. Checks were made on possible bias related to this multiple usage of protons, without detectable effects on the final results. The recorded hadronic events are then treated as independent in the subsequent simulation steps.

The MAGIC Monte Carlo Corsika Simulation (Mmcs6501) produces an output file containing the information about the Čerenkov photons (cer****** file), a ******.dat file with information about the other particles and a log file with statistics and general information on the generation of the shower.

The theoretical knowledge of all the high-energy hadronic interactions which occur in an EAS is still incomplete: the CORSIKA simulation accounts for the following physical features:

Hadronic interactions and decay of unstable particles: The distance covered by a hadron before it interacts or decays is determined by its cross-section for hadronic interactions and the probability of its decay. The corresponding decay and interaction lengths are randomly determined, and the shorter one is taken as the actual path length.

As the energy of the particle varies along its trajectory, our simulation employs at present two different packages to reproduce at the best the hadronic interactions: QGSJET-II (quark-gluon string model) for high-energy interactions [Kal97] and FLUKA for low-energy interactions [Fer05].

Most of the particles produced in high-energy interactions are unstable: π^0 and other neutral mesons have such a short lifetime that their interaction with the atmosphere before the decay is neglected. On the other hand, neutrons are treated as stable particles due to their long lifetime and muons are prevented from penetrating the whole atmosphere only by decay.

Electromagnetic interaction models: The interactions of electrons and photons are simulated using the EGS4 (Electron Gamma Shower System version 4) package [Nel85].

For electrons or positrons, EGS4 treats bremsstrahlung and multiple scattering, Bhabha and Møller scattering and annihilation, while Compton scattering, electron-positron production and photoelectric reactions are considered for γ-rays.

EGS4 also reproduces the photoproduction of muon pairs and the interactions with protons and neutrons of atmospheric nuclei.

Particle tracking through the atmosphere: The propagation of particles along the track between two interaction points accounts for the ionization energy loss (with the Bethe-Bloch formula), the deflection by the Earth's magnetic field and the Coulomb multiple scattering.

As the atmosphere nuclei are much more massive than the EAS charged particles, CORSIKA treats this scattering as a possible change in direction of the incident particle, but not in its energy.

Moreover, the Coulomb multiple scattering is considered for each tracking step only once in the middle position.

There are different atmosphere models implemented in CORSIKA: the composition referred to in MAGIC-II simulation consists of a mixture of N_2 (78.1%), O_2 (21.0%), Ar (0.9%) and an atmosphere density profile recently optimized for MAGIC observations [Bil06].

Čerenkov radiation: CORSIKA treats Čerenkov photons within a wavelength band defined in the input card: the Čerenkov production threshold ($v > c/n$) for charged particles is checked

at every step of the trajectory, using the following approximated expression for the refraction index: $n_h = 1 + 0.000283(\rho(h)/\rho(0))$, where $\rho(h)$ is the atmosphere density value (in g/cm^3).

Once the total number of emitted photons N_C has been computed for a given tracking step, CORSIKA subdivides them in small bunches, which are emitted from shorter sub-steps along a straight line, defined by the emission angle θ_C and a random value for the azimuthal angle around this direction.

Each photon bunch is treated as a unit, rather than as a group of single Čerenkov photons to reduce the computational steps and time.

The information about Čerenkov photons arriving at the observation level is recorded in the cer****** output file, namely the total number of Čerenkov photons, the individual x and y position coordinates at the observation level, the direction cosines u and v, the arrival time and the height of production above sea level.

3.1.2 Reflector-II

The Reflector-II program [Mor03, Bil06] accounts for the Čerenkov light absorption and scattering in the atmosphere and the reflection of the surviving photons on the mirror dish.

The present version, adapted for the stereoscopic production, reads in the cer****** files produced by Mmcs6501 and writes two output files, one for each telescope, with information about all the photons which reach the telescope focal plane within the camera position.

The Reflector-II production is steered by a specific input card, which includes also the path to the reference input files involved in the reconstruction (files magic.def, axis_dev.dat and reflectivity.dat) and the model of atmosphere to be accounted for.

The simulation of Čerenkov light absorption has been originally introduced in Reflector because it was not yet available in previous versions of CORSIKA. Even after its introduction in more recent versions, the default atmosphere model (US standard atmosphere, [COR, US]) and geometry do not allow the accuracy sought for by MAGIC.

For that reason, the Čerenkov light absorption is still treated separately from CORSIKA: moreover, new atmospheric models have been introduced in Reflector-II on the basis of thorough studies performed on the atmosphere over La Palma [Mor03].

In more detail, a comparison of the default model used by CORSIKA with the more accurate NRMLSISE-00 [MSI] atmosphere modeling based on rocket and satellite measurements pointed out significant differences [Bil06].

When lateral distribution plots of the resulting photon densities on the ground at La Palma were computed to compare the two models, a decrease of $10 - 15$ % was observed with respect to the US standard atmosphere model (see figure 3.1.a), while the results are close to the NRMLSISE-00 model within 2%.

To make the simulation closer to the real situation, two new atmospheric models have been obtained averaging on six-month intervals, respectively called MagicSummer and MagicWinter (see figure 3.1.b).

Present MAGIC-II simulation include therefore MagicWinter atmosphere density profile instead of US standard one.

The physical processes considered within Reflector-II to simulate the atmosphere effects on Čerenkov light propagation are the Rayleigh scattering by the air molecules, the scattering by aerosols and the absorption by ozone molecules.

A further tool to make multiple use of the hadronic showers has been introduced in present version of Reflector-II to optimize the CPU time employed in the overall simulation: once a hadronic

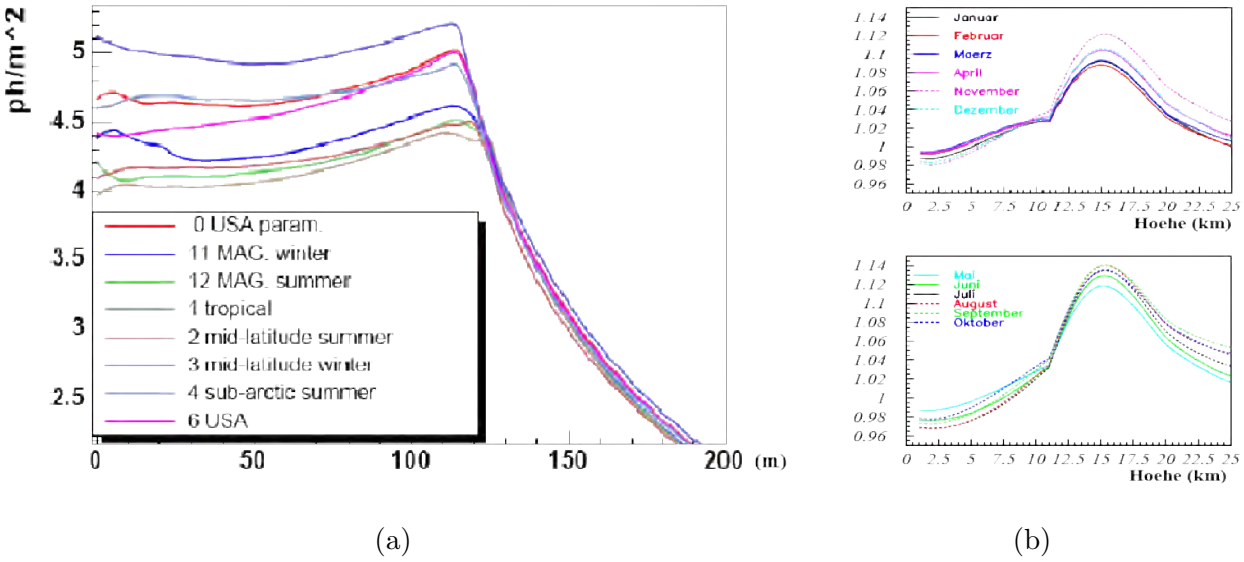

(a) (b)

Figure 3.1: *(a) Lateral distribution of Čerenkov photons with various atmosphere models (primary γ-rays of energy = 50 GeV). (b) Deviation of monthly measured density profiles on MAGIC site from US standard atmosphere model [Bil06].*

shower has been simulated by CORSIKA, Reflector-II allows to change the incident hadron direction at random within a cone of semi-amplitude 5° for each event up to 20 times.

This option results in a "fast production" of multiple "independent" showers from each single CORSIKA generated event.

The number of randomizations used for present production is 10: together with the multiple telescope configuration introduced in CORSIKA, a total multiplicity of 160 for each primary hadron event is obtained.

Reflector-II produces two separate output data files (*.rfl files) with the information about all photons reaching the cameras: these files can also be used independently to simulate the response of each single telescope.

3.1.3 Camera

The Camera program [Bla04] simulates the behaviour of the MAGIC photomultipliers, trigger system and data acquisition electronics.

Pulse shapes, noise levels and gain fluctuations obtained from the MAGIC real data have been implemented in the new Camera 0.8 version, including the detailed features of the two present MAGIC-II cameras.

A steering card sets all the relevant parameters of the simulation and the input files to be used.

In more detail, different PMT models can be chosen, corresponding to different QE files, as well as the light collection efficiency of single pixels with regard to angle of incidence of the photon.

The Camera software package also includes a program, called Starrespo, which generates a set of random signals from the PMTs to simulate the NSB, one of the main factors limiting the IACT's energy threshold.

Another program in the package, StarFieldAdder, can be used on demand to add a specific sky field of view to the camera image, in order to simulate at the best the real observations in presence of stars or bright objects in the field of view.

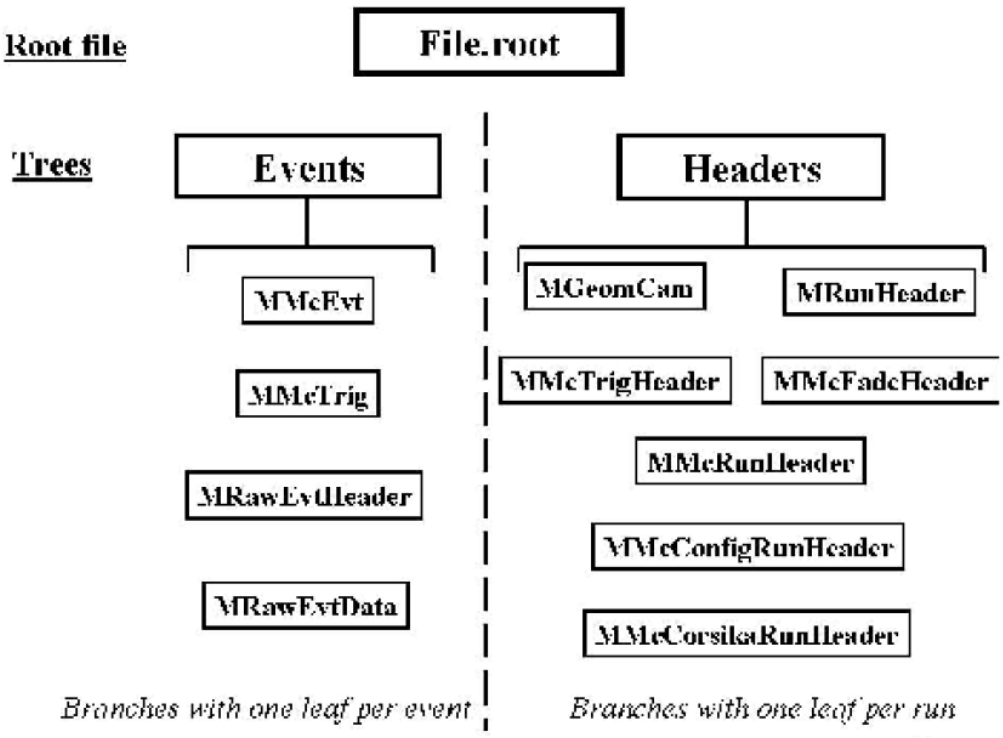

Figure 3.2: *Diagram of a MAGIC simulated data *.root file [Bla04].*

The output of camera 0.8 program is stored in a *.root file [ROO] for each telescope analyzed, in a format corresponding to the real raw data files, but with one more branch with the information specific of the simulation (see figure 3.2).

3.2 The MC simulation database for MAGIC-II

The stereoscopic detection of the Čerenkov signals is essentially different from the single telescope one: the new solutions introduced in the design of the second telescope make it impossible even to test separately the new clone using the simulated data produced for MAGIC. A completely new database of simulated events is thus required to test MAGIC-II. Its production required plenty of CPU power, generation time and storage facilities: the choice to locate it at CNAF [CNA] allowed to deal with such task.

CNAF is the Italian TIER-1 computational centre recently enhanced to support the LHC data production within a GRID system: the facility is presently (end of 2008) reaching 5000 MSi2K [CNA], roughly corresponding to 12000 Xeon@2.4 GHz CPUs.

Since 2007 the Udine group of the MAGIC collaboration has dynamical access to CNAF CPU power, which has been widely used for the production (see figure 3.3).

The CPU power assigned to MAGIC for the year 2009 is 80 KSi2K, to be increased to 125 KSi2K from 2010 on, meaning that in case of conflicting requests and overbooking, possible with the "full engine" LHC production, this is the minimum granted quota. A dynamical access allows to overcome this assignment on short periods whenever more CPUs are available due to minor use by other experiments.

As the access to CNAF resources is restricted to authorized operators, a mirror repository has

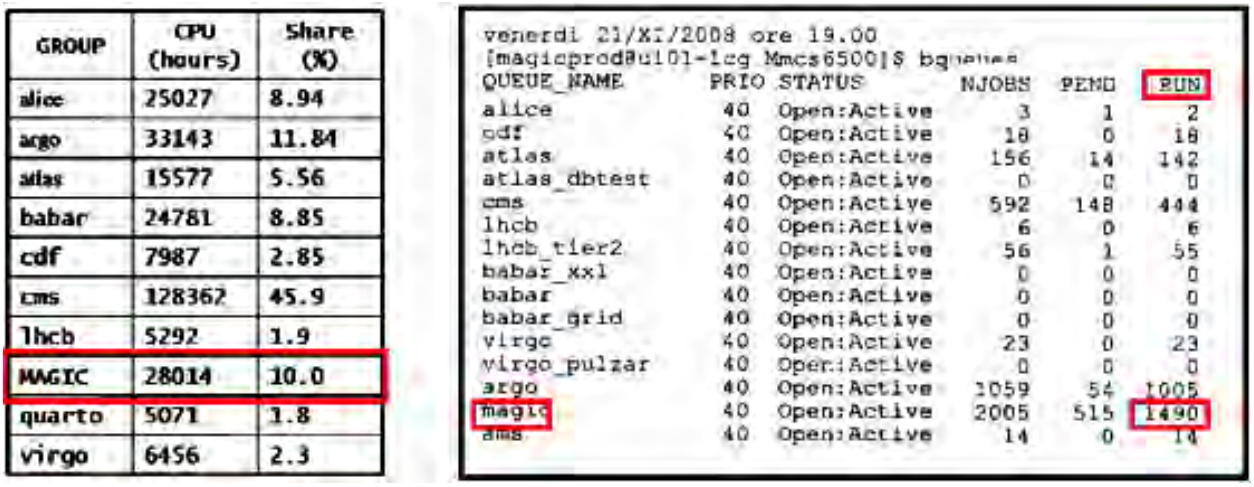

GROUP	CPU (hours)	Share (%)
alice	25027	8.94
argo	33143	11.84
atlas	15577	5.56
babar	24781	8.85
cdf	7987	2.85
cms	128362	45.9
lhcb	5292	1.9
MAGIC	28014	10.0
quarto	5071	1.8
virgo	6456	2.3

(a)

```
venerdi 21/XI/2008 ore 19.00
[magicprod@ui01-lcg Mmcs6500]$ bqueues
QUEUE_NAME      PRIO STATUS          NJOBS  PEND  RUN
alice             40  Open:Active        3     1    2
cdf               40  Open:Active       18     0   18
atlas             40  Open:Active      156    14  142
atlas_dbtest      40  Open:Active        0     0    0
cms               40  Open:Active      592   148  444
lhcb              40  Open:Active        6     0    6
lhcb_tier2        40  Open:Active       56     1   55
babar_xxl         40  Open:Active        0     0    0
babar             40  Open:Active        0     0    0
babar_grid        40  Open:Active        0     0    0
virgo             40  Open:Active       23     0   23
virgo_pulzar      40  Open:Active        0     0    0
argo              40  Open:Active     1059    54 1005
magic             40  Open:Active     2005   515 1490
ams               40  Open:Active       14     0   14
```

(b)

Figure 3.3: *Examples of dynamical use of CNAF resources: (a) Averaged CPU share at the end of april 2008 (b) Top value reached in batch queue share.*

been created at the URL http://www.UD_MAGIC2.pd.infn.it to make all the *.root files produced by Camera and a set of the reflector files directly accessible by all the MAGIC physicists.

Since the configuration of MAGIC-II cameras will change over the time, the whole Reflector-II production is stored at CNAF to allow the production of updated Camera files, while primary CORSIKA production is left after use to optimize the storage resources.

The database includes at present 8×10^8 proton events and 12×10^6 gamma events for a rough total of 80000 *rfl files, corresponding to a storage occupation of more than 20 TBytes, and camera files in different configurations for a total of more than 6 TBytes.

A balanced production of proton and gamma files has been sought, in order to allow a ratio of 100:1 between hadron and gamma samples to be used in the analysis.

With regard to the average CPU time required and the size of the resulting *rfl files, 500 primary events were generated for each cer****** file, corresponding to a size of 80 MB and a CPU time of 10 hours for each gamma file, while 500 MB and 30 hours of CPU were needed for each proton file.

Up to date (end of 2008), three sets of 10000 cer****** files each have been produced, one of protons and two of gamma showers for ON-OFF and wobble observations, plus some gamma samples on demand for specific studies.

The main parameter values fixed for CORSIKA generation are

- the energy, ranging from 10 GeV and 30 TeV for gammas and from 30 GeV and 30 TeV for protons;

- the energy distribution, a pure power law with a spectral index of -1.6 for gammas, whereas index -1.78 was fixed for protons. This spectral index is set a unit higher than the real observed spectra to get more statistics at higher energy. A simple scale factor introduced in the analysis allows the comparison of results with real data.

- the zenith angle, ranging within 0° and 30° for the three main data sets. A further set of gamma files has also be produced with high zenith angles, i.e. in the range 30° to 45°.

- the azimuth angle, varying on the whole circle, from 0° to 360°. The full azimuth generation allows the "reazimuthing" of the sample, important to study the effects of geomagnetic field

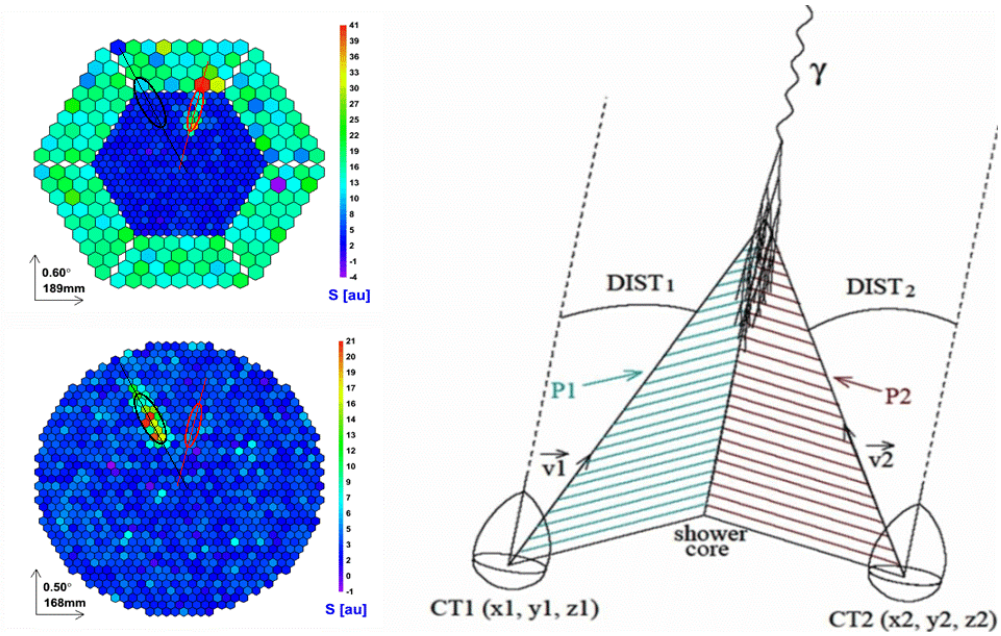

(a) (b)

Figure 3.4: *Stereoscopic imaging of the showers. (a) Images produced by the same simulated shower on the two MAGIC cameras. (b) The single-image informations are geometrically combined to give the incoming direction of the shower and core distance.*

on lower energy showers.

- the maximum impact parameter, fixed in 300 m for gammas and about 850 m for protons. In more detail, the γ-ray showers have been generated within a circle of $r = 300$ m, while for proton showers a square of side $l = 300$ m centered on the array reference position has been accounted for. This choice, combined with the multiple positioning of the arrays introduced in CORSIKA, allowed to estimate the effect of proton showers with impact parameters up to 850 m.

The differences between proton and γ-ray parameters equalize the different efficiency in Čerenkov production by hadronic EAS and purely electromagnetic showers.

3.3 Stereoscopic Analysis of the events

In principle, the two telescopes in the MAGIC-II system can be independently operated to observe two different sources or sky regions at the same time. However, the best performance of the system is achieved with the simultaneous observation of the same air showers with the two telescopes.

As illustrated in paragraph 2.2.3, only showers triggering both telescopes are considered under the *Stereoscopic Analysis* (SA hereon).

The image reconstruction, obtained in the same way MAGIC alone did until 2008 for each telescope separately, is the first step of SA. As usual in the Čerenkov shower imaging, the Hillas parameters [Hil85] of the single ellipses are computed at this stage: the two images are then combined [Hof99b] to obtain the stereoscopic Hillas parameters of the shower. In particular, the

intersection point of the two ellipse's major axes provides the location of the source on the camera for each triggering shower (figure 3.4.a).

Once this information is obtained, the important parameter θ^2, defined as the square of the angular distance between the reconstructed source direction and the nominal one (the center of the camera) can be calculated. This parameter sharply peaks around zero for γ-rays coming from a point-like source, while it spreads evenly for an isotropic flux like that of hadronic cosmic rays (see figure 3.8.a).

The location of the shower core on the ground is obtained by intersecting the image axes from the telescope positions on the ground. The height of the shower maximum (H_{max}) can also be reconstructed (see figure 3.4.b).

The quality of the stereoscopic imaging depends on the amplitude of the recorded images and on the angle between the axes: however, SA gives direct answers to the problems which affect the single telescope reconstruction. In particular, a single telescope can hardly resolve the ambiguity between the signals generated by a close-by and low-energy shower and a more distant, high-energy one, while SA removes it in most cases.

The geometrical merging of the stereoscopic images allows to evaluate the distance and direction of the shower more precisely than the single telescope reconstruction.

Relying on a single image, the position and impact parameter of the shower must be calculated with the DISP method [Dom05].

This method assumes that the source position is located along the major axis of the Hillas ellipse at a certain distance DISP from the image centre of gravity: the calculated eccentricity of the Hillas ellipse gives an estimate of the distance between the shower and the source position in the camera.

The DISP parameter is calculated using a parametrization DISP = a+b·Width/Length, where a and b are second order polynomials of $\log_{10}(SIZE)$.

The energy reconstruction is based on lookup-tables where MC energy of gamma showers is tabulated as a function of shower impact parameter, H_{max} and $SIZE$.

The shower energy is calculated in SA averaging the values independently obtained for each telescope.

3.3.1 Image cleaning

When a shower triggers, the whole camera picture is taken: the resulting raw image needs a previous cleaning before it can be properly analyzed (see figure 3.5).

The image cleaning identifies the pixels carrying information about the shower and rejects the pixels corresponding to NSB or electronics noise signals.

The selected pixels are classified as "core pixels", representing the main part of the shower, and "boundary pixels", which define the image edge.

Their selection holds in particular on two thresholds, n_{core} and n_{neigh}, which define the image pixels with regard to the corresponding photoelectron number. A"10–5 cleaning" is adopted in present simulation, classifying as core pixels those giving a signal above 10 phe, and as boundary pixels those giving a signal above 5 phe.

This is an absolute cleaning, and the chosen values fit well a high-energy source analysis, but result in a rejection of many low-energy showers, which should be treated with less conservative cleaning (e.g. "7–5").

A further selection rule which defines a core pixel is the presence of at least two neighbouring core pixels, in order to discard isolated pixels wich give a possible spurious signal.

The effect of a proper image cleaning is shown in figure 3.6.

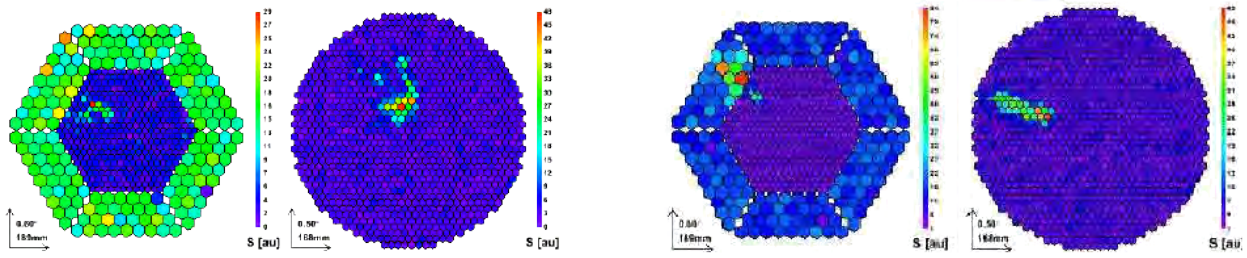

(a) (b)

Figure 3.5: *MAGIC-II simulated raw images: (a) Images of a shower generated by a 400 GeV proton on the two cameras. (b) Images of a shower generated by a 500 GeV γ-ray on the two cameras.*

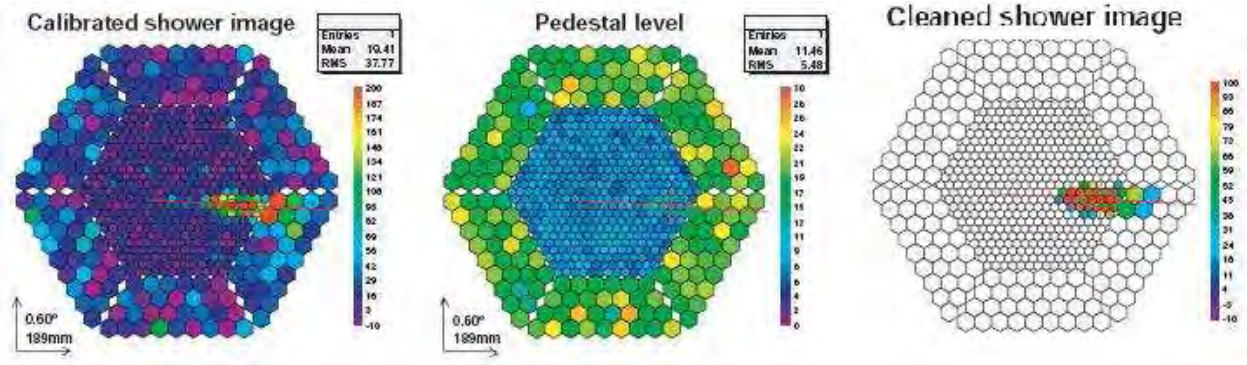

(a) (b) (c)

Figure 3.6: *Example of cleaning 10–5 on a real shower image: (a) Raw image from the MAGIC camera; (b) Pedestal level corresponding to this run; (c) Shower image after a 10–5 cleaning.*

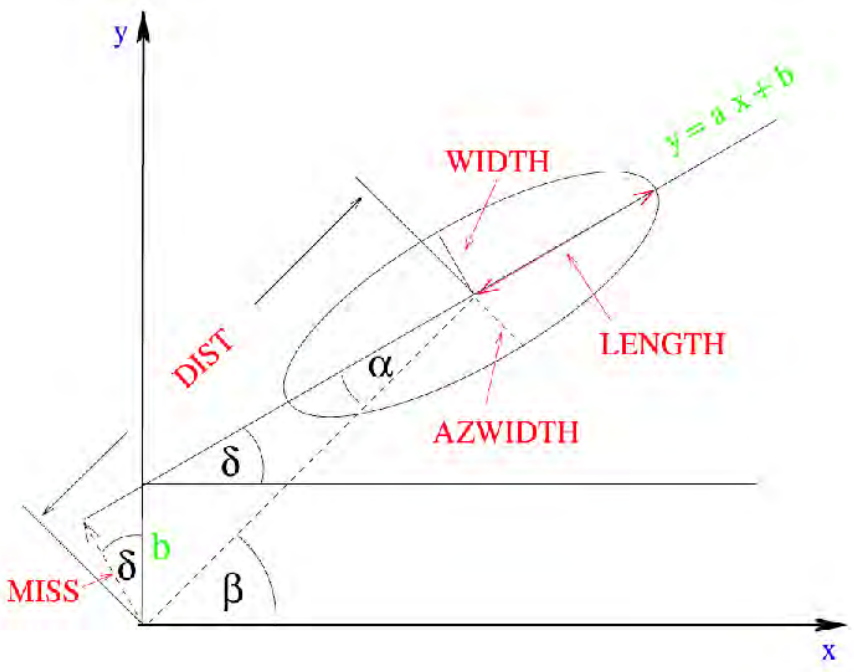

Figure 3.7: *Image parameters: an ellipse is drawn to represent a shower image. The most important Hillas parameters are displayed. Point (x_0,y_0) represents the centre of the camera.*

3.3.2 Image reconstruction

The Čerenkov shower images are rough ellipses usually parametrized following Hillas [Hil85] (other forms of semi-analytical fitting are rarely used): physical information on the shower are extracted with the moment analysis of the recorded image.

The zero-order momentum gives the image amount of light, the 1st-order momenta give the image gravity centre, the 2nd-order momenta give the shape and direction of the ellipse and the 3rd-order momenta give the image asymmetry.

The ellipse parameters can be grouped with respect to the shape or the orientation [Wit02]. The following characterize the size and shape of the image (see figure 3.7):

- *SIZE*: the total integrated light content of the shower. It gives information on the total energy of the shower.

- *CONCN*: the ratio between the sum of light of the first n pixels with higher signal and the sum of light for all pixels in the image.

- *LENGTH*: the RMS spread of light along the major axis of the image. It gives information of the longitudinal development of the shower.

- *WIDTH*: the RMS spread of light along the minor axis of the image. It gives information of the lateral development of the shower.

- *LEAKAGE*: the ratio between the photon number in the two outer rings of pixels and the total amount of photons for all pixels in the image.

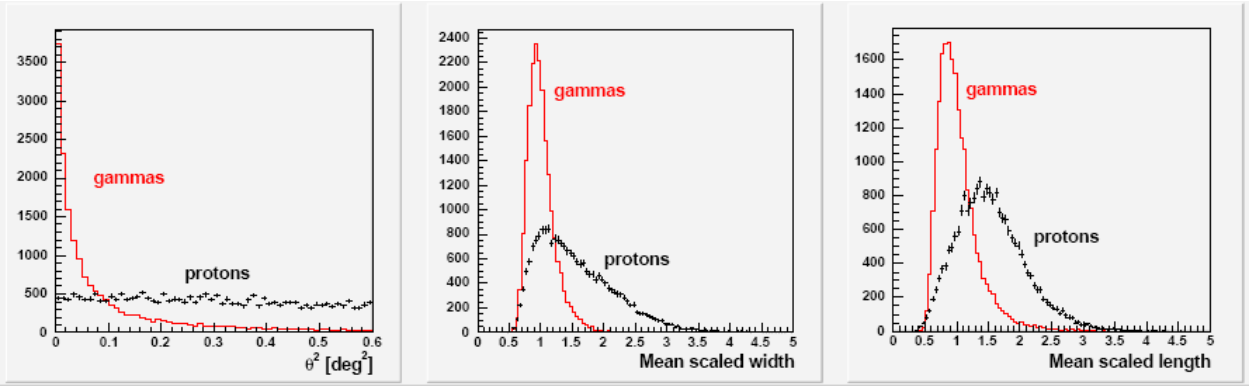

(a) (b) (c)

Figure 3.8: *Example of Hillas parameter plots [Mor04]: (a) θ^2; (b) Mean Scaled WIDTH; (c) Mean Scaled LENGTH.*

- *M3LONG*: the asymmetry of the light distribution (third moment) along the major axis. It is positive when the image is pointing towards the source position in the camera.

- *ASYM*: the distance from highest pixel to centre, projected onto the major axis of the ellipse.

On the other hand, these are the main orientation parameters:

- *ALPHA* (α): is the angle between the major axis of the image and the radius drawn from the source position in the camera to the image centre. It is related to the angle between the shower axis and the telescope axis.

- *DIST*: the distance from the image centroid to the centre of the camera FoV. It gives information about the impact parameter of the shower.

- *MISS*: the perpendicular distance between the major axis of the image and the source position in the camera.

- *AZWIDTH*: the RMS spread light perpendicular to the line which connects the image centroid to the source position in the camera. It gives a measure of both the image shape and orientation.

These crude elliptical images of the Čerenkov light pool are very useful to reject the large cosmic-ray background, as γ-showers and hadronic ones are well identified by different combinations of Hillas parameters.

The shower parameters are computed analyzing the second moments of the images recorded by the single telescope cameras. Among the parameters obtained, *WIDTH* and *LENGTH* are the most effective in discriminating the signal from the background (γ/hadrons).

More parameters can be calculated for analysis purposes: the *MEAN SCALED LENGTH* (MSL) and the *MEAN SCALED WIDTH* (MSW) [Kon97, Dau97] are defined by subtracting the mean value and dividing by the RMS of the simulated γ-ray parameter distribution as a function of *SIZE*.

MSW and MSL distributions have a mean value of 0 and RMS of 1 for gamma showers and are broader for proton showers (see figure 3.8).

3.3.3 Hadronic background rejection

The separation between hadronic background ("hadron-like" events) and γ-induced showers ("gamma-like" events) in MAGIC relies on the *Random Forest* (RF) technique [Bre01, RAN], which proved to be the fastest and most efficient in classifying images as gamma-like or hadron-like [Boc04, MAG08b].

First, two set of simulated gamma proton events are used to train the RF. The training is done by feeding the algorithm with a set of variables for each event, e.g. some of the Hillas parameters which most differ from hadron- to γ-induced events.

The RF trainig returns for each event a single output variable, called *HADRONNESS*, ranging from 0 to 1. A *HADRONNESS* value close to 0 means the event is gamma-like, while a value close to 1 points very likely to a hadronic origin (see also figure 3.10).

After the growing of the RF, the data set to be classified is driven through the program and the *HADRONNESS* of each event is determined.

The background discrimination is obtained by applying a cut in *HADRONNESS*, which keeps a substantial fraction ε_γ of gamma-like events and a fraction $\varepsilon_h < \varepsilon_\gamma$ of hadron-like (protons in present MC analysis) events.

A very tight cut is generally not convenient because it would reduce too much the number of gammas, while a loose cut will result in poor sensitivity.

A usual choice is to take the cut which provides the highest *quality factor* $Q = \varepsilon_\gamma/\sqrt{\varepsilon_h}$ (see also figure 3.11).

Since the fluctuations of the number of background events follow Poisson's distribution, the statistical significance of the detection of a given γ-ray source is expected to be increased roughly by a factor Q when this cut is applied.

The γ-induced showers are eventually selected by coupled cuts on *HADRONNESS* and other Hillas parameters (usually θ^2): the surviving images are then analized to obtain physical information about their source.

3.3.4 MARS, the analysis software for MAGIC

The simulated data files produced by Camera 0.8 have the same structure of the future raw data taken with MAGIC-II telescope: in principle they should be treated the same way along the analysis chain to undergo the image treatment described above.

Turning from a single telescope to a stereoscopic system requires changes in the analysis software at almost all levels: the present situation (end of 2008) is in rapid evolution, but not all the programs needed for the SA have been completed yet.

For this reason, the present SA of the simulated data for MAGIC-II has been carried out in some parts by equivalent programs which allow the coupling with the existing software for single telescope analysis.

The existing MAGIC standard Analysis and Reconstruction Software (MARS) [Mor08] is a collection of programs written in C++ in the framework of the ROOT data analysis software developed at CERN [ROO].

The different tasks are performed by various executable programs to be applied in cascade. The correspondence between input and output root files is traced by the file naming, which keeps almost the same form along the chain except for a label: _D_ denotes raw data files, _Y_ the *Callisto* outputs, _I_ the *Star* outputs, _Q_ the *Melibea* outputs...

The MARS executable *Callisto* performs the data calibration, i.e. the conversion of the FADC reading of each pixel into a number of photoelectrons and an arrival time.

The image cleaning and parametrization are performed by the *Star* program, which produces the so-called "star files".

Like their progenitor calibrated files, the star files contain ROOT trees, the main difference being in the contents of the Events tree: instead of storing the whole event image, each entry of the Events tree in a star file contains just the image parameters, grouped in different containers like MHillas, MHillasSrcDep, MHillasExt...

The training of the RF needed to optimize the analysis is carried out by the *Osteria* program: as this procedure is different for source-dependent and source-independent analyses, *Osteria* performs them both in parallel.

Osteria is fed with two training samples of star files (*_I_*.root) as input, one of gamma events, the second of hadron events. The gamma training sample is usually a MC one, chosen to match at the best the real data to be analyzed.

Osteria selects from the input hadron sample as many events as there are in the γ-ray MC sample. This selection is not completely at random, rather depending on the *SIZE* and the zenith angle of the events, and it is adjusted such that the final hadron sample has the same distribution as the gamma sample on these two parameters.

If *Osteria* did not apply this sort of "equalization", e.g. if the training sample happened to have a larger fraction of large zenith angle events than the hadron sample, then the RF might identify the larger zenith angle events as gamma-like.

Although the optimization of all parameters is possible within the same execution of *Osteria*, it is more convenient to run separately the program to optimize the γ/hadron separation and the Energy (and DISP) estimate.

Once the training has been completed, the RF grown by *Osteria* are stored in two files, one for the source-dependent random forest (RF.root) and another for the source-independent random forest (RFSrcIndep.root).

The algorithms optimized by *Osteria* are then used by the *Melibea* program to determine the main features of the primary particle (nature, energy, incoming direction) in the data sample.

Melibea needs two inputs, namely:

- The outputs of *Osteria* containing the RF parameters of the algorithms to be applied to the data for γ/hadron separation, for energy estimation and possibly for the DISP method (used to evaluate the incident direction with a single telescope).

- The star files (*_I_*.root) to be processed, containing either real data to be analyzed, or simulated events used e.g. as "test" sample to evaluate the performance of MAGIC-II.

The main output of *Melibea* consists in a "star-like" file for each one of the input star files, containing the same ROOT trees, but with two important differences:

- The Events tree now includes extra containers: MHadronness, MEnergyEst, and, for the case of source-independent analysis, MImageParDisp.

- The events not fulfilling the prior cuts "SkipNonShowers" and "FilterCuts, set in osteria.rc, will be skipped.

The events in the *Melibea* files are then a subsample of those in the corresponding input star files.

The most interesting parameters in the new containers are MHadronness.fHadronness, MEnergyEst.fEnergy and MImageParDisp.fX, MImageParDisp.fY.

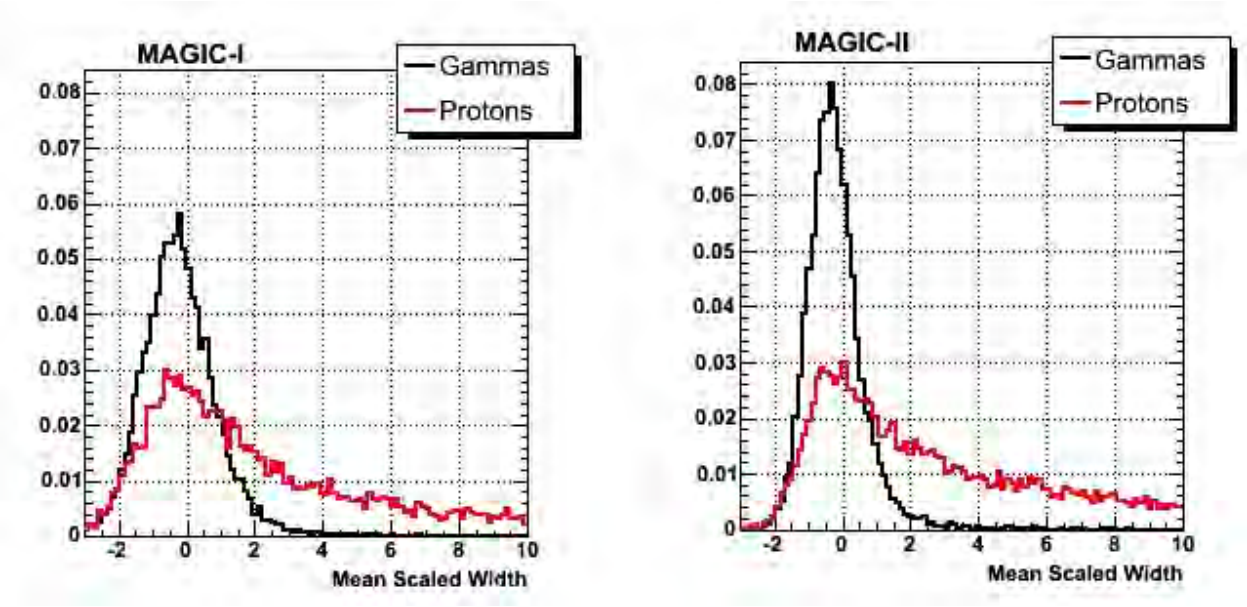

Figure 3.9: *The MSW distributions obtained on the simulated sample (a) with single MAGIC and (b) with MAGIC-II SA reconstruction.*

They are, respectively, the *HADRONNESS* of the event, its reconstructed energy, and the shower direction on the camera obtained with the DISP method, to be used in the study of the sources.

The physical information is eventually extracted by the selected events with fast programs as *fluxlc* or ROOT macros.

3.4 Performance estimates for MAGIC-II

The whole set of proton and no-wobble gamma events in the database (8×10^8 "proton" events and 5×10^6 "gamma" events, respectively) have been used for this study.

A fraction of 10% of the produced events has been used to train the RF, the remaining 90% has been used to estimate MAGIC-II performance.

3.4.1 Random Forest input parameters

The RF parameters considered for present analysis are:

- *SIZE*, i.e the average amplitude of the shower;
- N_{island}, the average number of islands (an island is defined as any cluster of two or more pixels surviving the image cleaning);
- H_{max}, i.e. the core distance;
- MSL, i.e. the *MEAN SCALED LENGTH*;
- MSW, i.e. the *MEAN SCALED WIDTH*.

Alternative parameter choices have been considered (with further or alternative constraints), giving only slight differences in the resulting *HADRONNESS*.

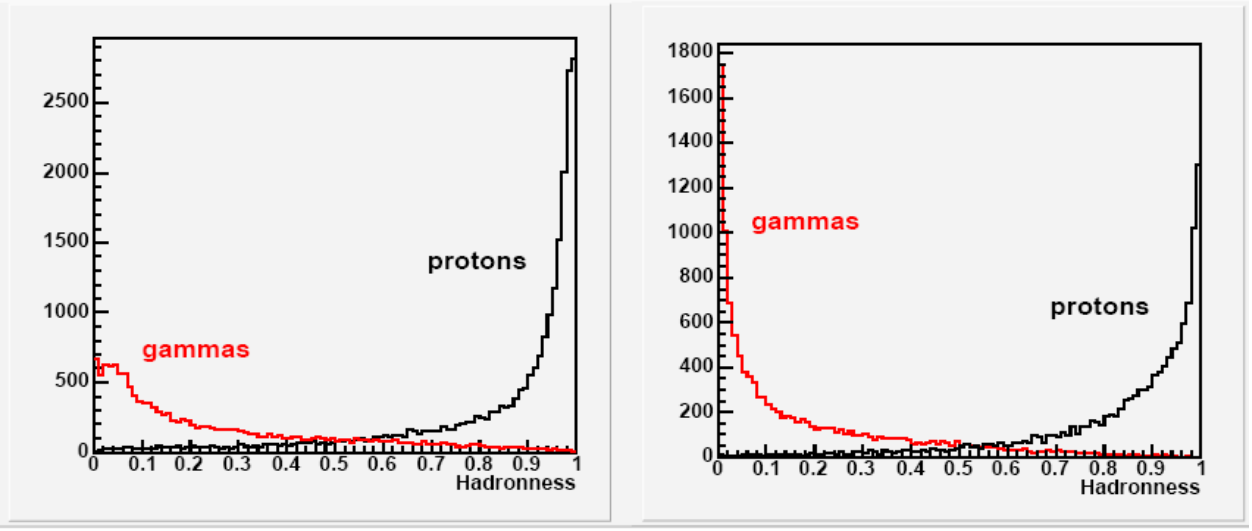

(a) (b)

Figure 3.10: *Comparison between the HADRONNESS distributions for hadron and γ events quality factors obtained (a) with MAGIC alone and (b) with MAGIC-II on an equivalent sample of events.*

3.4.2 Simulation results

The background rejection in present study is based on the *HADRONNESS* and θ^2 parameter is used to extract the signal events.

To get a direct comparison between the existing and future situation, an equivalent analysis has been carried out for the single MAGIC telescope.

In order to keep the same energy distributions (within the statistical uncertainties) for gamma events in both cases, and in particular the same value of the peak energy $E_{peak} \simeq 40$ GeV, an additional cut $SIZE > 130$ phe$^-$ has been imposed to the single telescope data.

A glance to the single parameter distributions obtained with MAGIC-I standard analysis and MAGIC-II SA already shows th potentialities of the latter (see e.g. figure 3.9).

The performance improvement introduced by the second telescope is better quantified by the *HADRONNESS* distributions and quality factors in the two cases (see figures 3.10 and 3.11).

The coincidence requirement introduced in L3 trigger produces various differences between the MAGIC-I and MAGIC-II performance.

A first effect, apparently negative, is that the effective area of MAGIC-II is smaller than that of any of the two telescopes: however, at energies above 300 GeV it matches the effective area of MAGIC, which is slightly lower than that of the new telescope because of their different QE.

On the other hand, the coincidence requirement provides a higher background rejection: this in turn improves the reconstruction of almost all parameters with respect to the single telescope analysis.

The SA in particular produces a better sensitivity below 100 GeV and also a reduction of the analysis threshold. The sensitivity of a IACT is usually defined as "The integral flux resulting in gamma excess events, in 50 hours of observation, equal to 5 times the standard deviation of the background".

The estimated sensitivity of MAGIC-II is shown in figure 5.16, plotted against the corresponding values of MAGIC and other existing experiments. A clear overall improvement is seen, which can be evaluated in a factor ~ 3 times with respect to the single MAGIC telescope: in particular, the

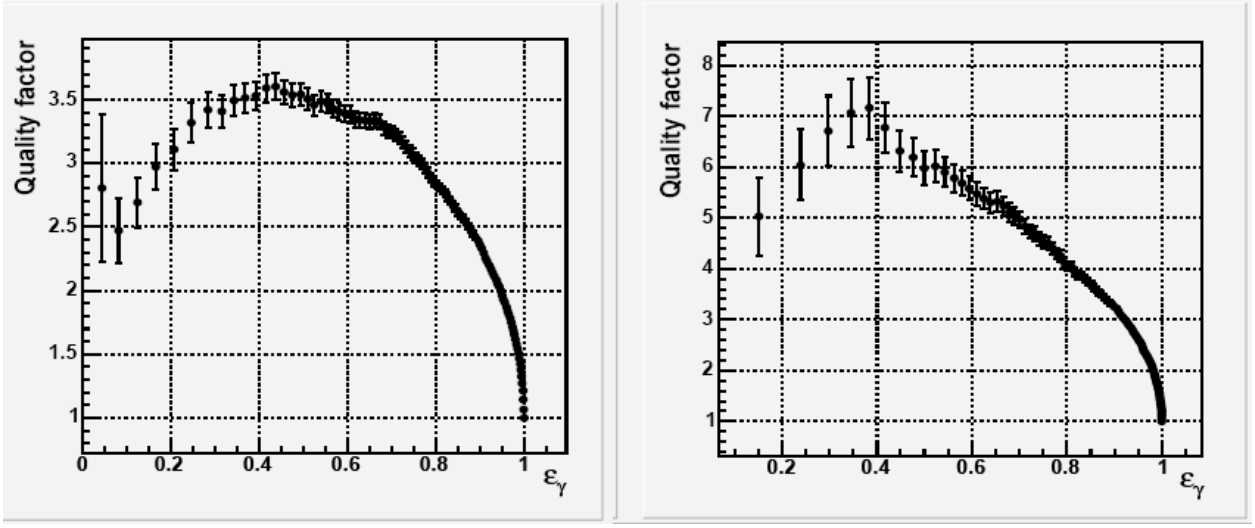

(a) (b)

Figure 3.11: *Comparison between the quality factors obtained (a) with MAGIC alone and (b) with MAGIC-II on an equivalent sample of events.*

sensitivity will significantly improve at energy values below 100 GeV. As indicated in figure 5.16, the MAGIC-II system is expected to achieve a sensitivity of 1% Crab in 50 hours above 150 GeV.

The SA also results in a better energy determination due to the improved reconstruction of the shower axis and to the double sampling of the light pool. The energy resolution for γ-rays as a function of primary energy is shown in figure 3.13. The energy resolution of MAGIC-I is also shown for comparison. An energy resolution better than 20% is achieved for γ-ray energy above 40 GeV, with values reaching 13 – 14% over 200 GeV, while in the same energy range the single telescope shows an energy resolution greater than 24% and rapidly approaching 30% and more at lower energies.

The same figure points out that the energy threshold reachable by MAGIC-II can be estimated within 20 – 30 GeV.

The angular resolution of a IACT is defined as the angle which contains 50% of the reconstructed γ-rays from a point source.

When analyzing the data taken with a single telescope, the angular resolution is computed using the DISP method, relying on the asymmetry along the major axis of the image to identify the shower head and tail. This procedure often results in a wrong head-tail assignment that degrades the overall angular resolution.

On the contrary, when observations are done by two telescopes this drawback is easily overcome, since the source direction is clearly determined as the intersection of major axes of the images in the camera.

The angular resolution computed for the stereoscopic telescope as a function of γ-ray energy is shown in figure 3.14, plotted together with the resolution obtained for the single MAGIC: the improvement obtained in angular resolution by MAGIC-II is outstanding. This improvement is at least of the order of 30% at energies close to the threshold value and even greater at greater energies.

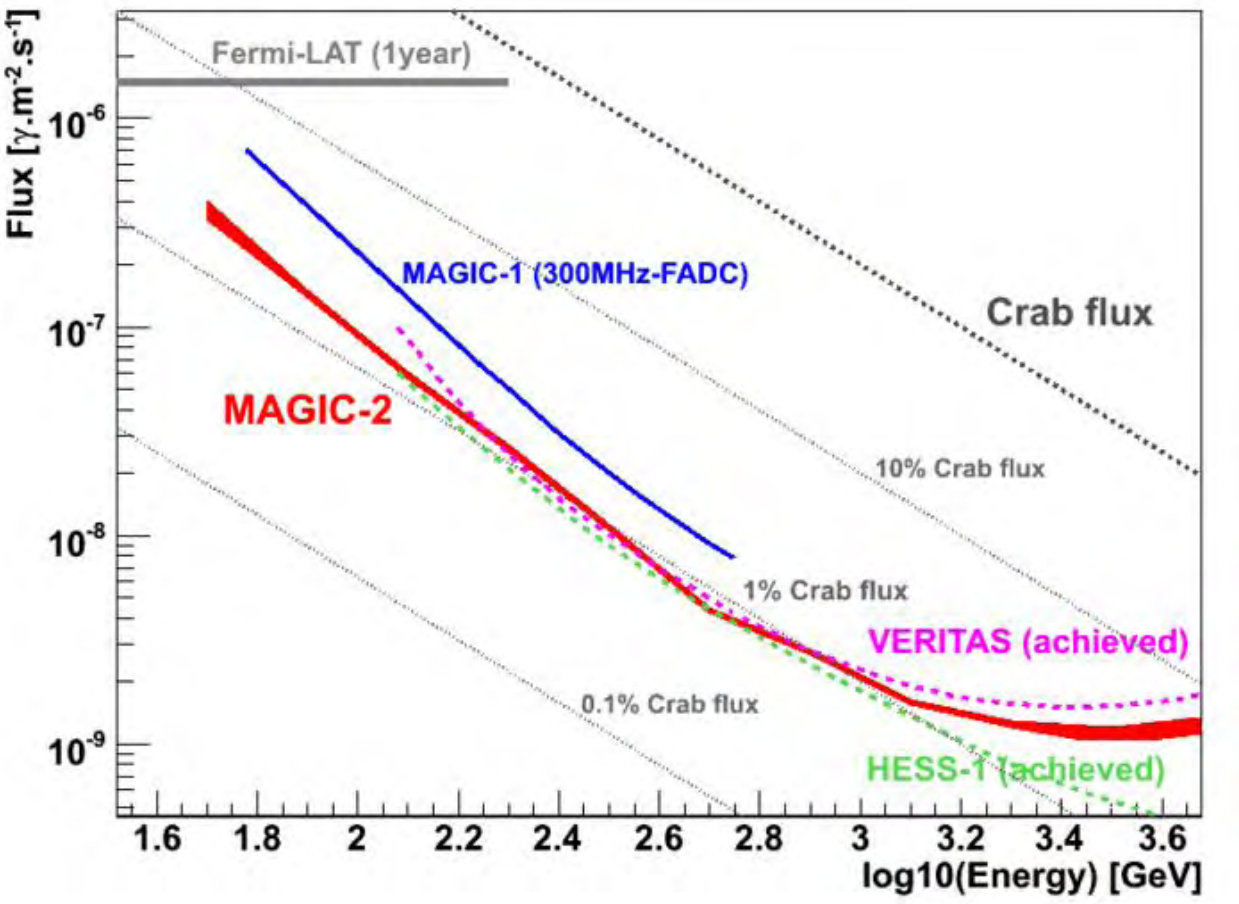

Figure 3.12: *MAGIC-II system sensitivity compared with the Crab flux and other existing experiments (MAGIC-I, HESS and VERITAS).*

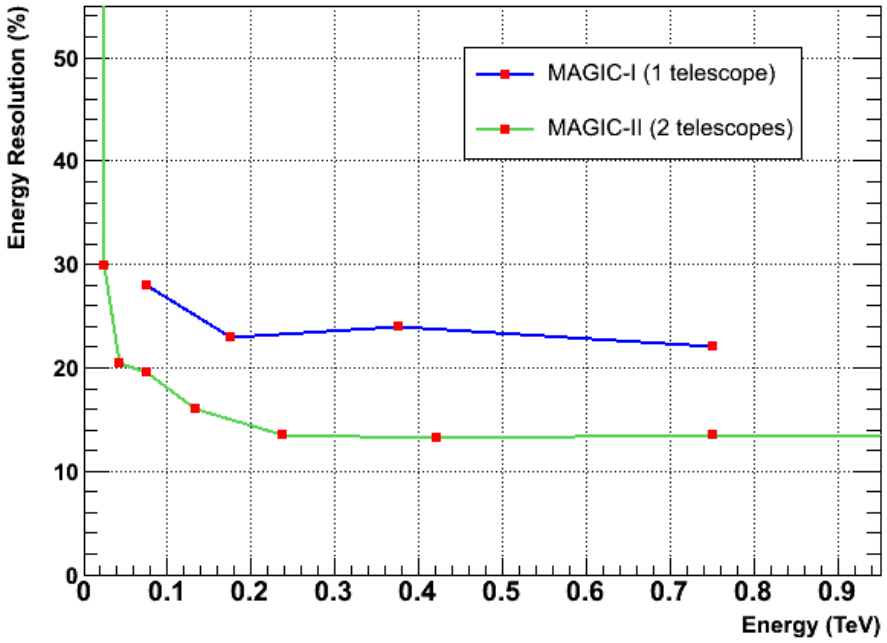

Figure 3.13: *Energy resolution of the MAGIC-II system (green line) compared with MAGIC-I (blue line).*

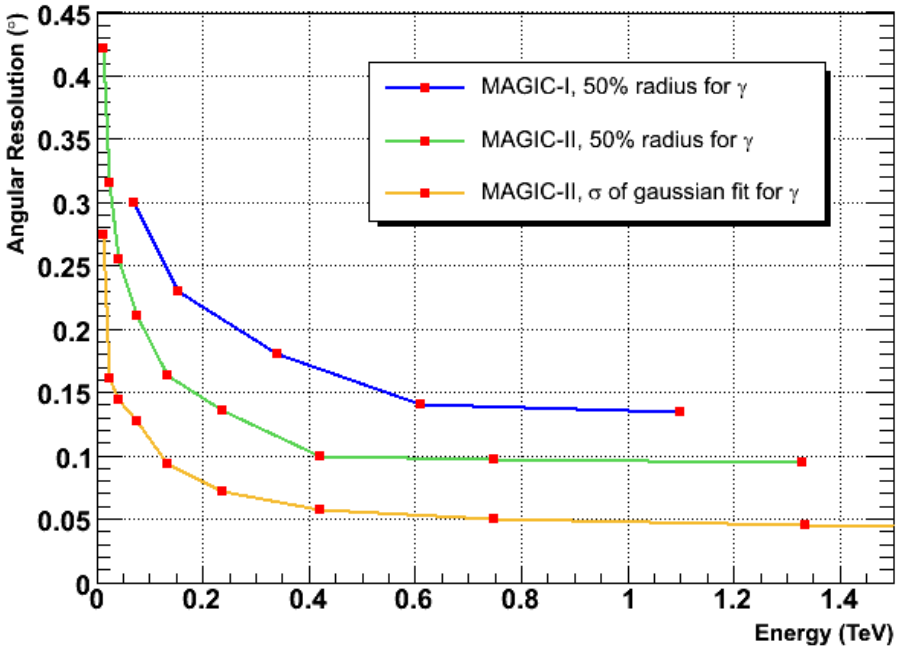

Figure 3.14: *Comparison of the angular resolution between MAGIC (blue line) and MAGIC-II (green line). The plot includes also the angular resolution obtained for MAGIC-II fitting the data with a 2-dimensional gaussian (yellow line).*

3.5 Summary

The potential of MAGIC-II has been tested using a wide database of simulated events, produced by the MAGIC Udine group using the CNAF facility. In particular, the set employed for this study included $5 \cdot 10^6$ primary gamma showers and $8 \cdot 10^8$ proton induced showers, with energies varying between 10 GeV and 30 TeV.

The functioning of the stereoscopic telescope has been simulated in detail by specific algorithms developed on the basis of the existing software for the single telescope and the simulation outputs have been analyzed with the current MARS analysis software or with equivalent subprograms for those parts presently under development.

The performance estimates clearly point out that MAGIC-II will allow a more precise reconstruction of the showers and a significant reduction of hadronic background below 100 GeV with respect to MAGIC. This will make possible an improved angular and energy resolution as well as a reduction of the analysis threshold. All together it will give to MAGIC-II a sensitivity increased of a rough factor 3 with respect to the MAGIC telescope.

Chapter 4

Intensity Interferometry: the road to Quantum Astronomy

Quantum Mechanics has been closely connected with light phenomenology since its very beginning, from Planck's hypothesis on the light quantization to Einstein's theory of photoelectric effect and Bohr's hypotheses on light emission by atoms [Pla00, Ein05, Boh13].

The quantum mechanical framework, developed by Schrödinger [Sch26, Dir30] and many other scientists in the mid-1920's, established the wave-like properties of matter particles. Features already investigated within a classical framework, such as light interference and indetermination, were also included in the newborn theory.

Only a year has passed since the publication of Schrödinger's theory when Dirac [Dir27] introduced the first quantization of the electromagnetic fields, pointing out the way for a quantum description of the light.

Nevertheless, the following theoretical developments in this direction (Feynman's QED theory [Fey50, Fey61], Glauber's theory of optical coherence [Gla63]) came only after some decades.

A possible reason for this delay is that the optical experiments performed up to the 1950's still allowed a description within a classical framework, and even first proofs of QED involved only few properties of single photons.

Many questions about the quantum nature of light, related to its statistical properties and distribution, independence of the emitted (or detected) photons, quantum noise and so on, were left open until maser and laser sources were available in the laboratory.

In the same decade, the pioneering measurements of R. Hanbury Brown [Han56, Han57, Han58] gave the first access to the (later named) domain of quantum astronomy.

Theorists then developed a full quantum optics framework to deal with these new experimental situations, for which classical and quantum predictions differ.

The main contributions came in the early 1960's from R. Glauber and L. Mandel: in particular, R. Glauber, who was awarded the Nobel Prize in 2005, developed the quantum theory of optical coherence [Gla63, Gla06] presently recognised as the most adequate theoretical framework.

The road to quantum astronomy will be reviewed in this chapter, starting from some classical interference effects and concepts, illustrating the results of R. Hanbury Brown and ending with some topics of Glauber's theory useful for understanding the present research scenario.

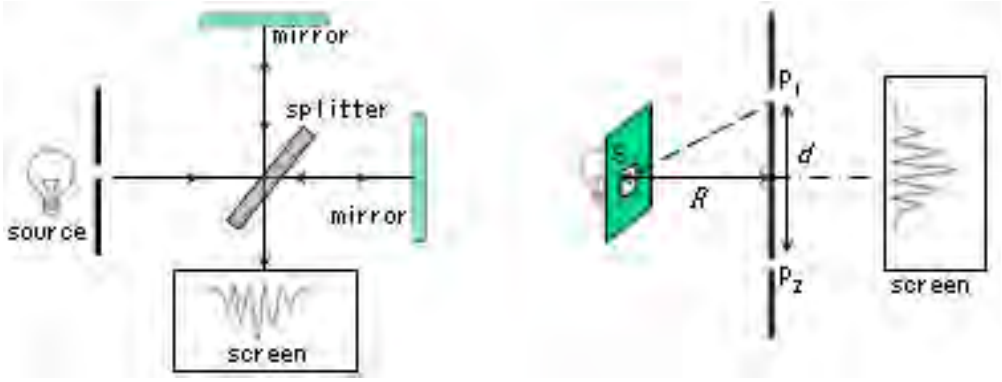

(a) (b)

Figure 4.1: *(a) sketch of Michelson interferometer and (b) of Young's two-pinhole apparatus.*

4.1 Interference effects and concepts: the classical background

Most optical experiments, from Young's early ones on, measured light intensity, usually averaged over time intervals: the main differences among them are in the design realized to overlap the fields with different t and $\vec{r}$ values arriving at the detector.

Once the wavelike behaviour of the light was established, the explanation of the experimental results in terms of interfering classic waves and phase differences turned out spontaneously for all those phenomena classified as "physical" optics (the alternative being "geometrical").

Following the Maxwell's theory and the unification between electromagnetism and optics, the interfering waves were then identified with oscillating electromagnetic fields.

The intensity of interfering light fringes formed in a Michelson interferometer or a Young's two-pinhole device depends on the coherence of the incident light: interference effects can also be described by means of light coherence and correlation functions for a classic electric field $\vec{E}(\vec{r}, t)$.

4.1.1 Temporal coherence

The concept of temporal coherence can be illustrated with reference to a Michelson interferometer (see figure 4.1.a).

If a light beam is split along two paths differing by Δl and then recomposed, the superpositions of the two components will produce interference fringes on a screen, provided that $\Delta t = \Delta l/c$ is sufficiently small, i.e. that it fulfils the condition

$$\Delta t \Delta \nu \leq 1 \tag{4.1}$$

The formation of the interference pattern can be explained in terms of temporal correlation of the two beams, depending on the delay Δt introduced by the different paths.

The *coherence time* parameter can be derived from 4.1 in the form:

$$t_{coh} \simeq 1/\Delta\nu \tag{4.2}$$

The corresponding length $l_{coh} = ct_{coh}$ is called *longitudinal coherence length* of the light. An equivalent statement of the coherence length in terms of λ is

$$l_{coh} \simeq \bar{\lambda}^2/\Delta\lambda \tag{4.3}$$

where $\bar{\lambda}$ is the average (nominal) wavelength of the light.

4.1.2 Spatial coherence

Young's two-pinhole experiment can illustrate the concept of spatial coherence when dealing with an extended source (see figure 4.1.b), e.g. a square of Δs sides on the symmetry axis of the apparatus.

The formation of the interference pattern on the screen shows a spatial correlation between the two components coming from the pinholes, as it can be related to the spatial separation of the light passing through the pinholes.

Experiments with thermal sources show that the fringe pattern will form on the screen provided the following condition is satisfied (see e.g. [Man95]):

$$\Delta\theta\Delta s \leq \bar{\lambda} \tag{4.4}$$

where $\Delta\theta$ is the angle subtended at the source by the pinhole distance d, and $\bar{\lambda} = c/\bar{\nu}$ is the mean wavelength of the light.

A new coherence parameter can be derived from 4.4 in the form

$$A_{coh} \simeq (R\Delta\theta)^2 \sim (R\bar{\lambda})^2/S \tag{4.5}$$

where R is the distance between the source and the pinholes plane ($R \gg d$) and $S = (\Delta s)^2$ is the source area.

A_{coh} is called *coherence area* of the light around the symmetry point Q of the two pinholes; its square root $trans_{coh} = \sqrt{A_{coh}}$ is called *transverse coherence length*.

The coherence area can also be expressed with reference to the solid angle $\Delta\Omega$ subtended by the source at the symmetry point Q of the two pinholes: a straightforward derivation from 4.5 gives

$$A_{coh} \simeq \bar{\lambda}^2/\Delta\Omega \tag{4.6}$$

It is worth noting that the solid angle $\Delta\Omega = \Delta A/R$ is an invariant quantity, while the coherence area depends on the source distance.

As the coherence area depends on the inverse of the solid angle subtended by the source, its value becomes experimentally detectable for pointlike (i.e. more distant) astronomical objects.

A. Michelson first measured A_{coh} for a "pointlike star" using an interferometer [Mic21]. The value obtained for Betelgeuse (α Orionis) was $A_{coh} \sim 6\,\mathrm{m}^2$, giving $\Delta\Omega \sim 4.15 \cdot 10^{-14}\,\mathrm{sr}$, which led to the determination of its diameter[1].

4.1.3 Correlation functions and interference

Correlation functions are useful in optics to describe the statistical and coherence properties of an electromagnetic field. The normalized correlation function of an electric field is called the *degree of coherence*.

[1] Some experimental values of t_{coh}, l_{coh}, A_{coh} and $trans_{coh}$ are quoted here as numerical examples.

Typical values for highly monochromatic light ($\Delta\nu \geq 10^8\,\mathrm{s}^{-1}$) emitted from a thermal source are $t_{coh} \sim 10^{-8}\,\mathrm{s}$ and $l_{coh} \sim 3\,\mathrm{m}$, while the beam light of a well stabilized laser ($\Delta\nu \simeq 10^4\,\mathrm{s}^{-1}$) is characterized by $t_{coh} \sim 10^{-4}\,\mathrm{s}$ and $l_{coh} \sim 30\,\mathrm{km}$.

With reference to the Sun, the wavelength value for a quasi-monochromatic beam of sunlight can be estimated at around $\bar{\lambda} = 500$ nm: as the solid angle subtended by the Sun on the Earth's surface is $\Delta\Omega \sim 6.8 \cdot 10^{-5}$ sr, the resulting value from 4.6 is $A_{coh} \sim (5 \cdot 10^{-7})^2/(6.8 \cdot 10^{-5}) \simeq 3.67 \cdot 10^{-9}\,\mathrm{m}^2$, the corresponding tranverse coherence length being $trans_{coh} \simeq 0.061$ mm.

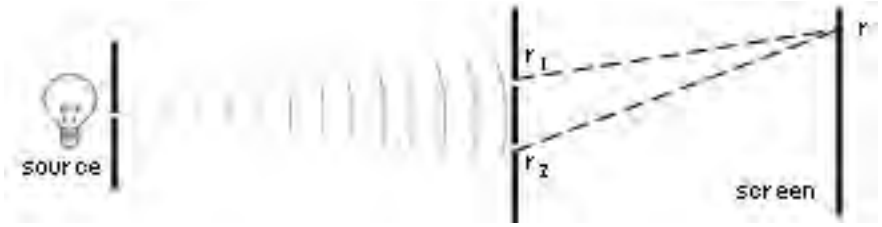

Figure 4.2: *Young's two-pinhole experiment: the two prepared pointlike sources in $\vec{r}_1$ and $\vec{r}_2$ emit in phase towards the screen on which interference pattern is observed.*

When dealing with a generic oscillating electric field $\vec{E}(\vec{r},t)$, it is mathematically useful to split it into two complex conjugate components

$$\vec{E}(\vec{r},t) = \vec{E}^{(+)}(\vec{r},t) + \vec{E}^{(-)}(\vec{r},t) \tag{4.7}$$

where $\vec{E}^{(+)}(\vec{r},t)$ includes only positive frequency terms (varying as $e^{-i\omega t}$ with $\omega > 0$), while $\vec{E}^{(-)}(\vec{r},t)$ includes the negative frequency components, so that

$$\vec{E}^{(+)}(\vec{r},t) = (\vec{E}^{(-)}(\vec{r},t))^* \tag{4.8}$$

Within a classical light description, this separation holds only in formal terms, since the two fields $\vec{E}^{(+)}(\vec{r},t)$ and $\vec{E}^{(-)}(\vec{r},t)$ are physically equivalent, while in a quantistic framework it also acquires a precise physical meaning, as will be shown further on.

The field intensity at fixed t and $\vec{r}$ is given by

$$I(\vec{r},t) = \frac{1}{2}\epsilon_o c|\vec{E}^{(+)}(\vec{r},t)|^2 = \frac{1}{2}\epsilon_o c\vec{E}^{(-)}(\vec{r},t)\vec{E}^{(+)}(\vec{r},t) \tag{4.9}$$

Young's two-pinhole experiment (figure 4.2) can be referred to as an archetype of optical interference to discuss in some detail the resulting light intensity, introducing a field correlation function $G^{(1)}$ as follows:

$$G^{(1)}(\vec{r}_1,t_1;\vec{r}_2,t_2) = \langle E^{(-)}(\vec{r_1},t_1)E^{(+)}(\vec{r_2},t_2)\rangle \tag{4.10}$$

where the angular brackets $\langle ...\rangle$ indicate the average evaluation of the quantity (usually over the observational time interval). The measured field intensity $\mathrm{I}(\vec{r},t)$ is then linearly dependent to $G^{(1)}(\vec{r},t;\vec{r},t)$.

As the field $E^{(+)}(\vec{r},t)$ is given by the sum of $E^{(+)}(\vec{r_1},t_1)$ and $E^{(+)}(\vec{r_2},t_2)$, the intensity measured at $\vec{r}$ depends on four correlation terms[2]

$$G^{(1)}(\vec{r}_1,t_1;\vec{r}_1,t_1) + G^{(1)}(\vec{r}_2,t_2;\vec{r}_2,t_2) + G^{(1)}(\vec{r}_1,t_1;\vec{r}_2,t_2) + G^{(1)}(\vec{r}_2,t_2;\vec{r}_1,t_1) \tag{4.11}$$

where the two latter cross terms in 4.11 lead to the interference pattern (intensity fringes) on the screen.

Just applying the Schwarz inequality to 4.10, it can be shown that the maximum value of $G^{(1)}$ is achieved if

$$|G^{(1)}(\vec{r}_1,t_1;\vec{r}_2,t_2)|^2 = G^{(1)}(\vec{r}_1,t_1;\vec{r}_1,t_1)\cdot G^{(1)}(\vec{r}_2,t_2;\vec{r}_2,t_2) \tag{4.12}$$

[2]Considering that the component fields $E^{(+)}(\vec{r_1},t_1)$ and $E^{(+)}(\vec{r_2},t_2)$ propagate to the point $\vec{r}$, the corresponding intensity should be fully quoted as $I(\vec{r},t) = \frac{1}{2}\epsilon_o c(|k_1|^2G^{(1)}(\vec{r}_1,t_1;\vec{r}_1,t_1)+|k_2|^2G^{(1)}(\vec{r}_2,t_2;\vec{r}_2,t_2)+k_1k_2^*G^{(1)}(\vec{r}_1,t_1\vec{r}_2,t_2)+k_2k_1^*G^{(1)}(\vec{r}_2,t_2;\vec{r}_1,t_1)$, where the k_i are the complex transmission factors for the field E along these specific optical paths. For the sake of simplicity, hereafter the k_i factors will be dropped, rather concentrating on the $G^{(1)}$ features.

which corresponds to the maximum fringe contrast, i.e. to the usual definition of relative coherence between the two sources in $\vec{r}_1$ and $\vec{r}_2$.

The condition for optical coherence can be equivalently stated as follows: once a positive frequency electric field $\mathcal{E}(\vec{r},t)$ is found, satisfying the appropriate Maxwell equations and such that $G^{(1)}$ can be factorized as

$$G^{(1)}(\vec{r}_1,t_1;\vec{r}_2,t_2) = \mathcal{E}^*(\vec{r}_1,t_1)\cdot\mathcal{E}(\vec{r}_2,t_2) \tag{4.13}$$

then an equivalent statement of optical coherence at first order is [Tit65]

$$|G^{(1)}(\vec{r}_1,t_1;\vec{r}_2,t_2)|^2 = |\mathcal{E}(\vec{r}_1,t_1)|^2\cdot|\mathcal{E}(\vec{r}_2,t_2)|^2 \tag{4.14}$$

The amplitude (and phase) interference between light waves as discussed for Young's experiment, or using other linear optical interferometers like Michelson's or Mach-Zender's, collectively referred to as "first-order interference experiments", is then described by the $G^{(1)}$.

The corresponding degree of coherence is commonly expressed by the normalized first-order correlation function

$$g^{(1)}(\vec{r}_1,t_1;\vec{r}_2,t_2) = \frac{\langle E^{(-)}(\vec{r_1},t_1)E^{(+)}(\vec{r_2},t_2)\rangle}{\sqrt{\langle E^{(-)}(\vec{r_1},t_1)E^{(+)}(\vec{r_1},t_1)\rangle\langle E^{(-)}(\vec{r_2},t_2)E^{(+)}(\vec{r_2},t_2)\rangle}} \tag{4.15}$$

which can assume values between 0 (complete incoherence) and 1 (full coherence), any intermediate value indicating a partially coherent state.

When dealing with stationary states for an incident plane wave, the resulting $g^{(1)}$ depends only on the time delay $\tau = t_1 - t_2$, (or $\tau = t_1 - t_2 - (r_1 - r_2)/c$, if $r_1 \neq r_2$), taking the form

$$g^{(1)}(\tau) = \frac{\langle E^{-}(t)E^{(+)}(t+\tau)\rangle}{\langle|E(t)^2|\rangle} \tag{4.16}$$

for which the properties $g^{(1)}(0) = 1$ and $g^{(1)}(\tau) = \left(g^{(1)}(-\tau)\right)^*$ hold.

As $g^{(1)}(\tau)$ takes different forms with reference to the kind of light, its shape can be used to discriminate among those situations (see figure 4.3.a).

In more detail, its explicit expression is:

- $g^{(1)}(\tau) = e^{-i\omega_0\tau}$ for light of a single frequency ω_0 (e.g. laser light);
- $g^{(1)}(\tau) = e^{-i\omega_0\tau-(|\tau|/\tau_{coh})}$ for Lorentzian chaotic light (e.g. collision broadened);
- $g^{(1)}(\tau) = e^{-i\omega_0\tau-\frac{\pi}{2}(\tau/\tau_{coh})^2}$ for Gaussian chaotic light (e.g. Doppler broadened);

When dealing with the coherence between pairs of fields, a normalized second-order correlation function $g^{(2)}$ is defined as:

$$g^{(2)}(\vec{r}_1,t_1;\vec{r}_2,t_2) = \frac{\langle \vec{E}^{(-)}(\vec{r}_1,t_1)E^{(-)}(\vec{r_2},t_2)E^{(+)}(\vec{r_2},t_2)\vec{E}^{(+)}(\vec{r}_1,t_1)\rangle}{\langle E^{(-)}(\vec{r_1},t_1)E^{(+)}(\vec{r_1},t_1)\rangle\langle E^{(-)}(\vec{r_2},t_2)E^{(+)}(\vec{r_2},t_2)\rangle} \tag{4.17}$$

Equation 4.17 includes a quartic term in $\vec{E}(\vec{r},t)$, pointing out that it is not a mere generalization of the first-order coherence; $g^{(2)}$ is typically involved in probing the statistical character of intensity fluctuations.

It should also be stressed that the second-order coherence is independent of the first-order one, just as the validity of equations4.13 or 4.14 does not necessarily imply an analogous statement being valid at second order.

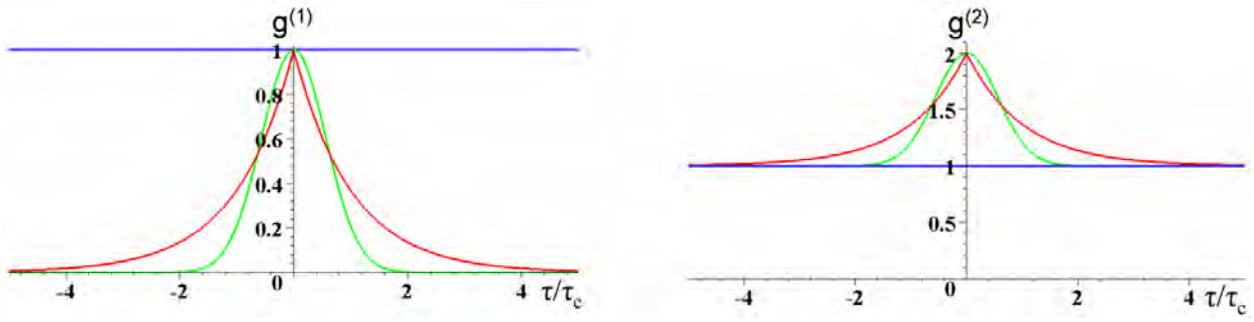

(a) (b)

Figure 4.3: *(a) $g^{(1)}(\tau)$ plot as a function of the delay τ for ideal laser light (blue line), Lorentzian chaotic light (red line) and Gaussian chaotic light (green line). (b) $g^{(2)}(\tau)$ plot as a function of the delay τ for ideal laser light (blue line), Lorentzian chaotic light (red line) and Gaussian chaotic light (green line). Note that the chaotic light is bunched (image credit: J. S. Lundeen).*

This independence turns out to be crucial to discriminate between states of light that require a quantum mechanical description and those for which classical fields are sufficient, as will be clarified further on.

Under the hypothesis of stationary states for an incident plane wave, the $g^{(2)}$ function depends only on the time delay τ and can be directly expressed as a function of the light intensities measured in $\vec{r}_1$ and $\vec{r}_2$, taking the simpler form

$$g^{(2)}(\tau) = \frac{\langle I(t)I(t+\tau)\rangle}{\langle |I(t)^2| \rangle} \tag{4.18}$$

As the $g^{(2)}$ function quoted in 4.18 is even, $g^{(2)}(\tau) = g^{(2)}(-\tau)$ holds. The application of the Cauchy-Schwarz inequality to the light intensity expressions gives also $1 \leq g^{(2)}(0)$ and $g^{(2)}(\tau) \leq g^{(2)}(0)$.

The possible value of $g^{(2)}$ (see also figure 4.3.b) turns out to be $g^{(2)}(\tau) = 1$ for laser light, while for chaotic light (of all kinds) $g^{(2)}(0) = 2$.

A remarkable relationship holding for chaotic light is

$$g^{(2)}(\tau) = 1 + |g^{(1)}(\tau)|^2 \tag{4.19}$$

which can be used (as R. Hanbury Brown did) to calculate the first-order light coherence of the light from its $g^{(2)}$ measured value.

A generalization of the coherence concept to the n-th order was also introduced, but its illustration exceeds the purposes of present work.

Moreover, their measurement by experiments on n-fold delayed coincidences is still to come.

4.2 The Hanbury Brown experiments on photon correlation

At the beginning of the 1950's, R. Hanbury Brown measured the diameter of some astronomical radio sources with a new type of interferometer, which worked on a radically different principle from Michelson's instruments [Han54].

That device detected independently the signals from two aerials, but only the correlation in fluctuations of the low-frequency detector's outputs was recorded, not the relative phases necessary to describe it as a classical wave interference measurement.

That technique directly measured the second order correlation function $g^{(2)}$: the $g^{(1)}$ could then be determined from 4.19 to express the results in terms of intensity interference.

The two different kinds of intensity interferometry were soon proved to be equivalent, but the new technique is peculiar in that the two signals do not really interfere with each other.

An optical instrument working on the same principle would then allow to loosen the optical precision and mechanical stability requirements which form the ultimate limit to the Michelson's interferometer.

Moreover, the signal detected with such an instrument is hardly affected by atmospheric scintillation.

Despite the success of the detections at radio wavelengths, which showed the correlation later named Hanbury Brown-Twiss effect (HBT), it was only with some hesitation that this method was turned to the optical domain, where the HBT effect had never been observed.

Indeed, at that time it was not even proved that the correlation would have been preserved by the photoelectric conversion in the detector.

As the experiment involves the correlation between photons detected by different counters, a quantum description suits the process much more than the classical interference formalism: again, it is worth noting that such a quantum optical theory had not been developed yet.

4.2.1 The laboratory optical test of HBT effect

To probe this new feature on visible light, a first laboratory experiment was carried out in 1955 on the correlation between photons in two coherent beams of light [Han56]: a new optical interferometer based on the same principle was tested immediately after on Sirius, to show the astronomical potentialities of this technique [Han56, Han58].

The laboratory experiment was then repeated with improved components and greater precision [Han57], in view of the controversy which surrounded the first published results.

The experimental apparatus is sketched in figure 4.4.a: the optical system consisted basically in a thermal source of light (the source employed was a mercury arc lamp, whose 435.8 nm line was properly selected and then divided into two coherent components), which illuminated two matched photomultipliers (R.C.A. 6342) following tunable optical paths.

The correlator, built with a bit of radioastronomer's knowhow, was able to resolve the tiny correlated signal component (the "wave noise", in classical language) embedded in a 10^5 times larger uncorrelated noise at the input of the photomultipliers.

The experimental results (see figure 4.4.b) showed the consistence of the HBT effect for optical photons and at the same time pointed out its quantum origin.

Nevertheless, their implications were at first skeptically considered by many physicists, although intensity interferometry had already been used in radioastronomy (relying on Maxwell's equations).

This negative reaction was due at first to the apparently equivalent experiments made as a check by different teams, which gave no evidence of the effect.

The need for a new quantum framework in a field where classic extensions of the theory seemed to give equally correct predictions (at least up to this result) found even stronger opposition.

Some misunderstanding could also arise from the misleading name of "interferometry" historically given to the HBT technique and its corresponding mental picture, although the detected photons did not really interfere with each other.

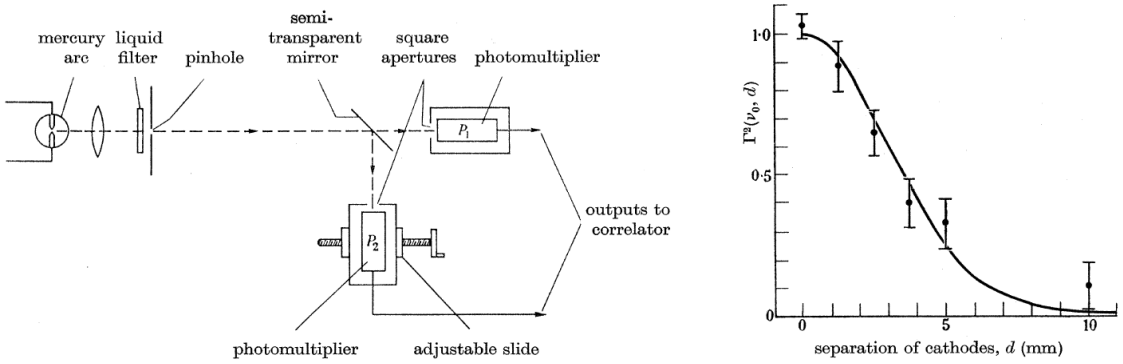

(a) (b)

Figure 4.4: *(a) Outline of the laboratory interferometer used by R. Hanbury Brown and R. Twiss. (b) The experimental correlation between photons measured with the photocathodes in different positions, superimposed to the theoretical dependence predicted [Han57].*

The experimental dispute was rapidly resolved by R. Hanbury Brown and R. Twiss themselves, who first pointed out the experimental limits of other teams which led to their negative results [Han56] and then also obtained new experimental evidences.

In particular, an experiment performed by R. Twiss and A. Little [Twi57, Twi59] first showed the time correlation between individual photons, better supporting the need for a quantum description of the HBT effect.

4.2.2 The quantum explanation of the HBT effect

Even when the correlation between the detected photons has been established experimentally and a first quantum explanation has been given, the validity of its theoretical foundations was questioned on a different basis.

The objections which seem to invalidate the model and which worth a more detailed illustration are as follows:

1. provided the model works, would it really give results equivalent with the classic treatment of intensity interference in the same situations?

2. as a description of light coherence in terms of the classical theory of wave interference has already been developed, why should a quantum framework be sought for?

3. if the quantum perspective had to be accepted, then the apparent conflict between a "two-photon interference effect" and Dirac's assertion that

   "...each photon (then) interferes only with itself.
   Interference between two different photons never occurs."

   quoted when discussing the Michelson interferometer results [Dir30, cap.1, pag. 9] must be resolved.

R. Hanbury Brown and R. Twiss directly answered to the first point [Han57], showing that their quantum-mechanical description of the effect gives identical results of the classical theory in which the photocathode is regarded as a suitable square-law detector.

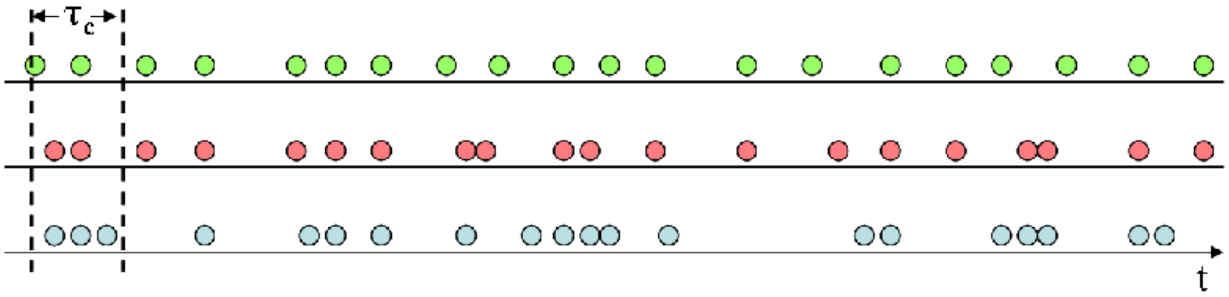

Figure 4.5: *Photon arrival time statistics (image credit: J. S. Lundeen).*

They argued that the phenomenon shows the wave rather than the particle aspect of the light, which allows an easy interpretation in terms of interference between different frequency components of the light.

In the same paper, they also proved that the particle picture holds, i.e. that the correlation measured by the two photocathodes is directly related to the so-called bunching of the photons, provided they are treated as undistinguishable quanta subject to Bose-Einstein statistics.

It is worth recalling that the clumping of bosons is just the manifestation of an effect already known in statistical mechanics at that time. As a consequence of the wave-particle duality of the light, both approaches are correct, pointing out the quantum nature of the system.

The answer to the second question was first overshadowed by the fact that the optical HBT effect was detected using a thermal light source, for which a positive correlation (photon bunching) holds: in that case, the quantum theory gives just the same predictions of the classical wave description.

Nevertheless, as E. M. Purcell soon pointed out [Pur56], this was not the only theoretical possibility when dealing with generic quantum systems: for instance, fermions systems would have exhibit opposite features (electron antibunching).

Even photon states differently originated, like laser or resonance fluorescence produced states, would have shown respectively null or negative correlation (see figure 4.5).

In particular, three reference situations can be distinguished (see figure 4.5):

- an antibunched distribution is possible, as detected in fluorescence emission [Kim77];
- a random (neither bunched nor antibunched) distribution, which is typical of a stimulated emission mechanism (laser) [Are65];
- a bunched distribution in time, which reflects quantum-random (i.e. chaotic for bosons) statistics, indicating the thermodynamic equilibrium of the source, which was the one first detected by R. Hanbury Brown [Han56, Mor66].

While the classical wave interference description would fail for systems different from thermal light, the quantum description gives correct predictions for the HBT effect in its various possibilities, as experimentally confirmed in the following years [Are65, Kim77, Hen99].

The relation between source emission mechanism and photon correlation features will be recalled further on, as it is of some importance in present quantum astronomy topics.

The third objection was first answered by U. Fano [Fan61], who pointed out that the "two-photon interference" accredited for the HBT effect can be dealt with in quantum mechanics once

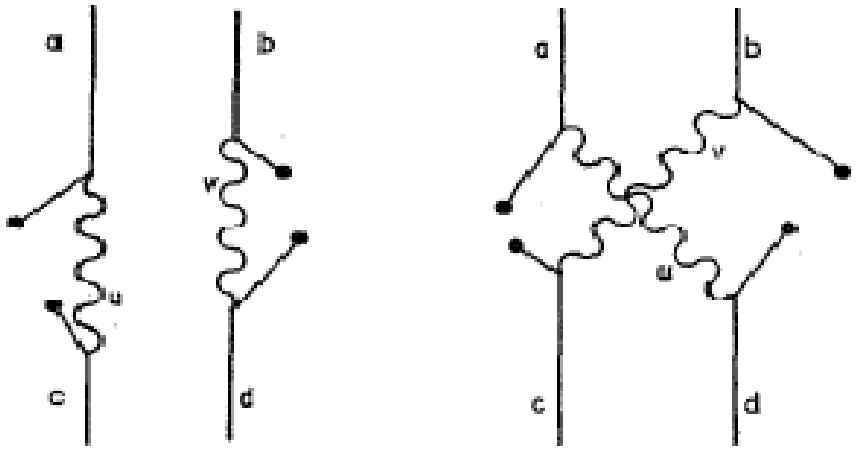

Figure 4.6: *The two lowest-order Feynman diagrams representing the emission of two indistinguishable photons (u, v) by a couple of atoms (a, b) and their absorption by a second couple (c, d) of atoms [Fan61].*

it is clear that the system has to be described by a two-boson state, not by two single-photon wavefunctions.

If u and v denote two photons emitted from two points a and b of a source and c and d the two detectors of a HBT inteferometer (see figure 4.6), a joint detection takes place whenever a photon u is absorbed by c and a photon v is absorbed by d, or when a photon u is absorbed by d and a photon v is absorbed by c.

Let the probability amplitudes for these two possibilities be denoted by $< u|c >< v|d >$ and $< u|d >< v|c >$ respectively.

If the photons are indistinguishable, the two amplitudes interfere constructively to give a joint detection probability greater than that for two independent events, originating the correlation effect.

Moreover, the sum over all possible pairs u,v in the source washes out the interference, unless the distance between the detectors is sufficiently small.

Differently from the first order interference experiments, a correct description of HBT effect in terms of single photon states is not possible: its quantum treatment requires at least the use of a two-photon state wavefunction.

To summarize, although the HBT effect can be predicted for thermal light just by treating the incident electromagnetic radiation as a classical wave, the quantum interpretation not only mimics the classical description, but turns out to be effective in many situations which have no classical wave analogue.

A quantum description is also required to reproduce the statistical distributions of photons generated by different mechanisms, like laser or resonance fluorescence, which are correctly predicted in a quantum perspective, while a classical wave description of these systems would fail.

It is worth noting that the experimental proofs on the cited quantum systems required new technological progress and came only some years later the first results on photon correlation, and also the quantum theory of optical coherence needed some years to be established: the work of R. Hanbury Brown had really been ahead of its time from both the theoretical and the experimental perspective.

Figure 4.7: *The Narrabri Intensity Interferometer [Han74a].*

4.3 The intensity interferometry at Narrabri and the dawn of a new astronomy

In the early 1960's, R. Hanbury Brown and R. Twiss further developed the second-order intensity interferometry technique with the construction of a device which, following Hanbury Brown's own expression

"...must be the most incomprehensible instrument in all of astronomy." [Dra08a]

A new stellar Intensity Interferometer (HBTII) was built at Narrabri (New South Wales), with the primary goal of determining the stellar diameters measuring the spatial correlation between photons coming from an astronomical source.

The same authors had previously showed that the correlation function $g^{(2)}$ amplitude for photons coming from a coherent source varies with the distance between the photomultipliers.

They also demonstrated that the $g^{(2)}$ amplitude is proportional to the squared modulus of Fourier transform of the intensity distribution of the source, and directly detectable measuring the correlation between the output currents of the two photomultipliers [Han57].

It is then possible, although the derivation is not trivial (see e.g. [Lou00]), to determine the angular size of a star from the variation of spatial correlation with the baseline of the photomultipliers.

The formulas describing a practical stellar interferometer were established by R. Hanbury Brown and R. Twiss in their fundamental papers [Han57, Han58] (for a plain re-elaboration, see also [Han74a]): only the final formulas related to the measured quantities expressed with reference to the quantum particle interpretation will be quoted in the present work.

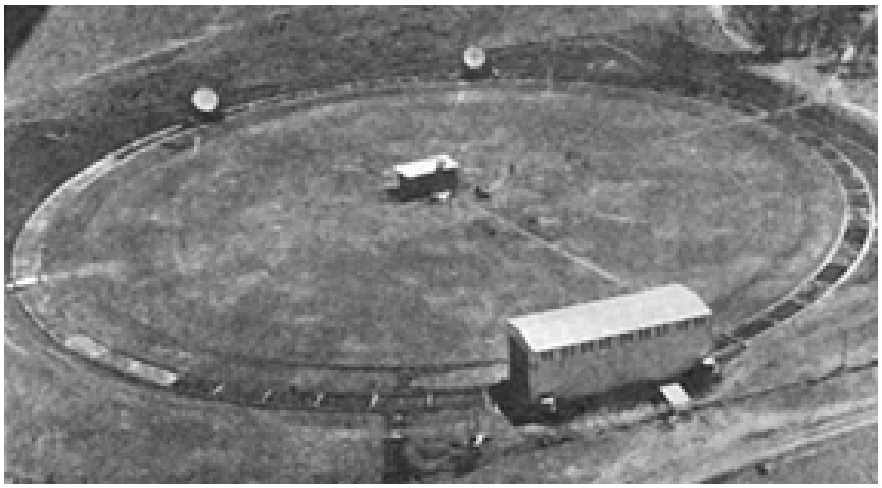

Figure 4.8: *Aerial view of the Narrabri interferometer [Han74a].*

Their determination required many factors to be accounted for, among them the dependence of correlation from the finite size and the quantum efficiency of the light detectors, the correct representation of response time of the apparatus, a thorough evaluation of the noise introduced by the photocatodes and electronics and a precise determination of the signal to noise ratio.

Considering a simple intensity interferometer correlating the output currents of two identical photomultipliers at distance d exposed to coherent light, the signal to be detected (cfr. eq. 4.35) can be expressed as [Han74a]

$$S(d,0) = <\Delta I_1 \Delta I_2> = e^2 A^2 \alpha^2 n^2 |g^{(2)}(d,0)|^2 \Delta\nu \Delta f \tag{4.20}$$

and the r.m.s. noise N in the multiplier output is given in the form

$$N(T_0) = \sqrt{2} e^2 A \alpha n \Delta\nu \sqrt{\Delta f / T_0} \tag{4.21}$$

In equations 4.20 and 4.21, T_0 is the time interval over which the multiplier output is averaged, e is the electron charge, A is the light collecting area of each detector, α is the quantum efficiency of the photodetectors, n is the photon intensity (per unit optical band, unit area and time), $\Delta\nu$ is the optical bandwidth and Δf the electrical bandwith of the instrument.

A straightforward calculation leads to the signal to noise ratio in the form:

$$(S/N)_{r.m.s.} = A \alpha n \sqrt{\Delta f \cdot T_0/2} |g^{(2)}(d,0)|^2 \tag{4.22}$$

R. Hanbury Brown and collaborators could then properly choose the features of the instrument to be built (see figures 4.7 and 4.8), which employed two photodetectors mounted at the focus of two large reflectors on movable trucks, whose distance could be varied from 10 m up to 188 m.

Each reflector (figure 4.9.b) was a mosaic of 252 hexagonal glass mirrors with 44 cm across and spherical curvature, made by Officine Galileo in Florence; the overall profile was paraboloidal, roughly 6.5 m in diameter and 30 m^2 of total area.

The employed phototubes changed over the years, raising the quantum efficiency at 440 nm from the initial 13% (R.C.A. type 7046) to the 25% of the last type (R.C.A. type 8850).

The fluctuating and the steady output components of the anode current signals were separated and carried to the correlator in the control room by low-loss coaxial cables.

The overall bandwidth between 3 dB for the whole system was about 55 MHz.

(a) (b)

Figure 4.9: *(a) A single hexagonal mirror (image: court. Sydney Powerhouse Museum) and (b) one of the reflectors of the stellar interferometer [Han74a].*

The correlator was designed (figure 4.10) to give input photocurrents of about 0.1 mA to the multiplier, the correlation being recorded each 100 s, together with a measurement of the total flux on each photomultiplier.

The signal formation and extraction technique required the development of a new linear multiplier [All70], whose performance turned out to be crucial in reducing the electronic noise.

Further improvements in the apparatus were also tried with the construction and test of a different, amplitude-limited, correlator [Yer68]. Although not integrated in HBTII, this novel component showed its potential for interferometers which could afford the small S/N loss introduced.

A rough estimate of the signal to noise ratio dealt with by R. Hanbury Brown at Narrabri can be calculated inserting the proper values $A = 30\,\mathrm{m}^2$, $\alpha = 0.2$ (for $\lambda = 430\,\mathrm{nm}$), $\Delta f = 100\,\mathrm{MHz}$ in equation 4.22.

A further factor $\Sigma \sim 0.2$ accounts for the comprehensive instrumental loss.

The S/N value corresponding to one hour of observation ($T_0 = 3600$ s) of an unresolved star (i.e. with $|g^{(2)}(d,0)| = 1$) of visual magnitude $m_V = 0$ in the zenith ($n \simeq 5 \cdot 10^{-5}\,\mathrm{photons\,m^{-2}\,s^{-1}\,Hz^{-1}}$) is

$$(S/N)_{r.m.s.} = 127\Sigma \sim 25 \tag{4.23}$$

Equation 4.23 summarizes the ultimate limit of the HBTII interferometer: despite its large (for that time) reflectors and even working with $S/N \sim 3$, only stars brighter than magnitude V = +2 could be fruitfully investigated.

The main experimental results obtained at Narrabri were the measured diameters of many different stars, quoted in figure 4.11, and other features of specific sources (Altair, Sirius, Spica...) [Han74b]. These results were used to establish the temperature scale for stars hotter than the Sun.

The optical configuration of the Narrabri interferometer allowed to measure the diameters of bright stars ranging from 0.0006" to 0.011" without resolving the star surfaces or detecting effects

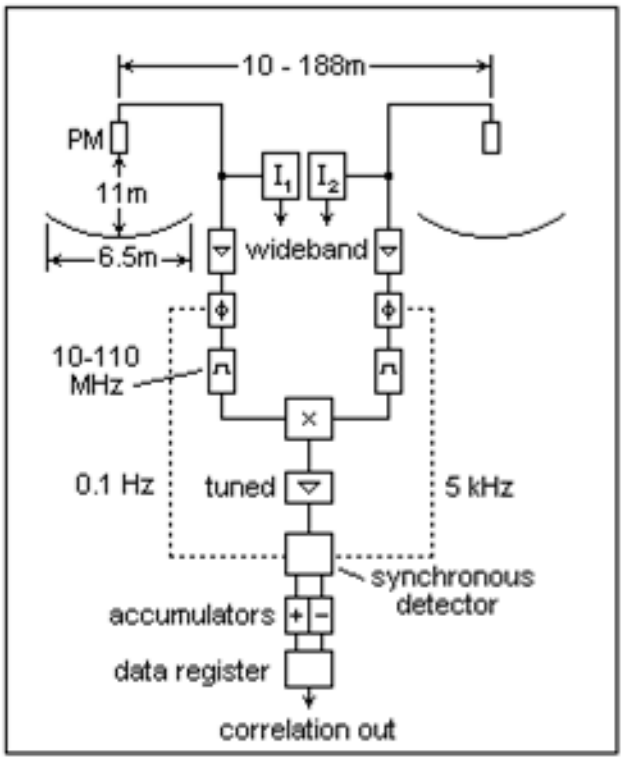

Figure 4.10: *Outline of the HBTII correlator [Han74a].*

related to the limb darkening or the rotational velocity.

An unexpected fallout of Hanbury Brown's observations was the detection of Čerenkov light pulses due to cosmic rays penetrating the atmosphere [Han69].

These measurements, taken to estimate the effects of Čerenkov radiation as a possible error source when observing stars, were recognised as due to primary cosmic rays of energy exceeding 1 TeV, while the conclusion was that their effect on interferometric investigations at Narrabri was negligible.

Even before the construction of HBTII, R. Hanbury Brown and R. Twiss already considered the possibility of measuring the $g^{(2)}$ correlation function with a single-photon counting interferometer.

This theoretical study was developed up to the determination of the corresponding signal to noise ratio in the form [Han57, Han74a]

$$(S/N)_{r.m.s.} = \frac{1}{2}\tau_{coh}\sqrt{R_1 R_2 T_0/2\tau_{coinc}}|g^{(2)}(d,0)|^2 \tag{4.24}$$

where τ_{coh} is the coherence time of the incident light, R_1 and R_2 are the photon counting rates of the two photocathodes, T_0 is the time interval considered and τ_{coinc} is the time interval which defines the coincidence between the two photons detected.

Although a series of measurements with such a device was obtained in laboratory experiments [Twi59], an analogous instrument for astronomical measurements was not created even after HBTII ended its working. The feasibility of that project was severely limited by the finite resolving time of the practical detectors and counters available in those years.

The intensity interferometer built at Narrabri remained so far the only astronomical instrument that investigated the second-order coherence properties of the light: nevertheless, it can be considered a cornerstone for the discipline now called quantum astronomy.

Star number	Star name	Type	Zero-baseline correlation $c_N \pm \sigma$	Angular diameter $\times 10^{-3}$ sec of arc $\theta_{UD} \pm \sigma$	$\theta_{LD} \pm \sigma$	Temperature $[T_e(F) \pm \sigma]$/K
472	α Eri	B 3 (Vp)	0·98 ± 0·05	1·85 ± 0·07	1·92 ± 0·07	13 700 ± 600
1713	β Ori	B 8 (Ia)	0·98 ± 0·08	2·43 ± 0·05	2·55 ± 0·05	11 500 ± 700
1790	γ Ori	B 2 (III)	1·03 ± 0·07	0·70 ± 0·04	0·72 ± 0·04	20 800 ± 1300
1903	ϵ Ori	B 0 (Ia)	0·86 ± 0·07	0·67 ± 0·04	0·69 ± 0·04	24 500 ± 2000
1948	ζ Ori	O 9·5 (Ib)	0·60 ± 0·06	0·47 ± 0·04	0·48 ± 0·04	26 100 ± 2200
2004	κ Ori	B 0·5 (Ia)	1·18 ± 0·09	0·44 ± 0·03	0·45 ± 0·03	30 400 ± 2000
2294	β CMa	B 1 (II–III)	1·07 ± 0·08	0·50 ± 0·03	0·52 ± 0·03	25 300 ± 1500
2326	α Car	F 0 (Ib–II)	0·75 ± 0·22	6·1 ± 0·7	6·6 ± 0·8	7500 ± 250
2421	γ Gem	A 0 (IV)	1·17 ± 0·09	1·32 ± 0·09	1·39 ± 0·09	9600 ± 500
2491	α CMa	A 1 (V)	0·91 ± 0·06	5·60 ± 0·15	5·89 ± 0·16	10 250 ± 150
2618	ϵ CMa	B 2 (II)	0·89 ± 0·06	0·77 ± 0·05	0·80 ± 0·05	20 800 ± 1300
2693	δ CMa	F 8 (Ia)	0·93 ± 0·18	3·29 ± 0·46	3·60 ± 0·50	— —
2827	η CMa	B 5 (Ia)	0·99 ± 0·09	0·72 ± 0·06	0·75 ± 0·06	14 200 ± 1300
2943	α CMi	F 5 (IV–V)	0·98 ± 0·10	5·10 ± 0·16	5·50 ± 0·17	6500 ± 200
3165	ζ Pup	O 5 (f)	1·04 ± 0·08	0·41 ± 0·03	0·42 ± 0·03	30 700 ± 2500
3207	γ^2 Vel	WC 8 + O 9 (I)	—	0·43 ± 0·05	0·44 ± 0·05	29 000 ± 3000
3685	β Car	A 1 (IV)	1·01 ± 0·06	1·51 ± 0·07	1·59 ± 0·07	9500 ± 350
3982	α Leo	B 7 (V)	1·12 ± 0·07	1·32 ± 0·06	1·37 ± 0·06	12 700 ± 800
4534	β Leo	A 3 (V)	1·17 ± 0·10	1·25 ± 0·09	1·33 ± 0·10	9050 ± 450
4662	γ Crv	B 8 (III)	0·97 ± 0·10	0·72 ± 0·06	0·75 ± 0·06	13 100 ± 1200
4853	β Cru	B 0·5 (III)	0·88 ± 0·03	0·702 ± 0·022	0·722 ± 0·023	27 900 ± 1200
5056	α Vir	B 1 (IV)	—	0·85 ± 0·04	0·87 ± 0·04	22 400 ± 1000
5132	ϵ Cen	B 1 (III)	1·02 ± 0·07	0·47 ± 0·03	0·48 ± 0·03	26 000 ± 1800
5953	δ Sco	B 0·5 (IV)	0·75 ± 0·07	0·45 ± 0·04	0·46 ± 0·04	— —
6175	ζ Oph	O 9·5 (V)	1·01 ± 0·12	0·50 ± 0·05	0·51 ± 0·05	— —
6556	α Oph	A 5 (III)	0·94 ± 0·09	1·53 ± 0·12	1·63 ± 0·13	8150 ± 400
6879	ϵ Sgr	A 0 (V)	1·02 ± 0·06	1·37 ± 0·06	1·44 ± 0·06	9650 ± 400
7001	α Lyr	A 0 (V)	0·99 ± 0·04	3·08 ± 0·07	3·24 ± 0·07	9250 ± 350
7557	α Aql	A 7 (IV, V)	0·94 ± 0·06	2·78 ± 0·13	2·98 ± 0·14	8250 ± 250
7790	α Pav	B 2·5 (V)	1·01 ± 0·07	0·77 ± 0·05	0·80 ± 0·05	17 100 ± 1400
8425	α Gru	B 7 (IV)	1·11 ± 0·08	0·98 ± 0·07	1·02 ± 0·07	14 800 ± 1200
8728	α PsA	A 3 (V)	1·02 ± 0·08	1·98 ± 0·13	2·10 ± 0·14	9200 ± 500

1. Bright star catalogue number (Hoffleit, 1964).
2. Star name.
3. Spectral type and luminosity class (in brackets).
4. Zero-baseline correlation normalized by the value expected from a single unresolved star and corrected for partial resolution ($\Delta\lambda$=1) (§ 10.3.1).
5. Angular diameter of equivalent uniform disc with r.m.s. uncertainty (§ 10.3.1).
6. True angular diameter allowing for the effects of limb-darkening (§10.3.2 and § 11.2.1).
7. Theoretical effective temperature of star computed by Webb (1971).

Figure 4.11: *Stellar angular diameters measured with HBTII [Han74a].*

HBTII worked on a simple application of the basic spatial coherence concept, but its conception required theoretical speculations and new technical solutions investigations which raised the interest in quantum optics theory and in various fields of applied physics, from photodetection to electronics.

For this reason, the contribution of R. Hanbury Brown to astronomy in terms of new ideas and knowhow may be considered of more worth than the experimental one.

4.4 Elements of quantum optics

Before concluding this chapter on the historical development of quantum optics which led to present quantum astronomy, it is useful to introduce at least the basic elements of Glauber's quantum theory of optical coherence.

First of all, the usual statements of a quasi-monochromatic light have to be assumed, i.e. that the bandwidth $\Delta\nu$ is small compared to its mean frequency $\bar{\nu}$ and that the light is macroscopically steady, meaning that no fluctuations are shown on a macroscopic time-scale.

Turning now to a quantum optics perspective (see e.g. [Lou00]), the separation between positive and negative frequency components of $\vec{E}(\vec{r},t)$ introduced in equation 4.7 leads to a straightforward interpretation of $\vec{E}^{(+)}(\vec{r},t)$ as annihilation operator and $\vec{E}^{(-)}(\vec{r},t)$ as creation operator with respect to the system state vector.

Acting on a n-photon state $|\psi_n>$ $(n>0)$, the operator $\vec{E}^{(+)}(\vec{r},t)$ lowers by one unit the number of quanta, pushing the system in the $(n-1)$-photon state, $|\psi_{n-1}>$.

Repeated applications of $\vec{E}^{(+)}(\vec{r},t)$ will eventually lead to the vacuum state $|\psi_0>$, with no quanta left: if $\vec{E}^{(+)}(\vec{r},t)$ is applied to this state, it then gives $\vec{E}^{(+)}(\vec{r},t)|\psi_0>=0$.

The operator $\vec{E}^{(-)}(\vec{r},t)$, adjoint of $\vec{E}^{(+)}(\vec{r},t)$, follows a similar rule: starting from vacuum state, for which $<\psi_0|\vec{E}^{(-)}(\vec{r},t)=0$ holds, it raises by one unit the number of quanta present in the system:
,

$$\vec{E}^{(-)}(\vec{r},t)|\psi_0>=|\psi_1>,\ \ldots,\vec{E}^{(-)}(\vec{r},t)|\psi_n>=|\psi_{n+1}> \tag{4.25}$$

To discuss the measurements of $\mathrm{I}(\vec{r},t)$ in a quantum optics framework, the detector's action on the field must be described in terms of operators.

An ideal detector is assumed with negligible size and with a photoabsorption probability independent of the frequence, also neglecting the photoelectric chain following the absorption.

A photon counter works by absorbing single quanta of the field and emitting photoelectrons: its action on the field is then described by the $\vec{E}^{(+)}(\vec{r},t)$ operator: the transition from an initial state $|i>$ to a final state $|f>$ is then described by the matrix element

$$\mathcal{M}_{fi}=<f|\vec{E}^{(+)}(\vec{r},t)|i> \tag{4.26}$$

To obtain the total transition probability, the squared modulus of 4.26 must be evaluated on a complete set of final states $(\Sigma_f|f><f|=1)$:

$$\begin{aligned}\mathcal{P}_{fi}=\Sigma_f|<f|\vec{E}^{(+)}(\vec{r},t)|i>|^2=\\ =\Sigma_f|<i|\vec{E}^{(-)}(\vec{r},t)|f>\cdot<f|\vec{E}^{(+)}(\vec{r},t)|i>|=<i|\vec{E}^{(-)}(\vec{r},t)\vec{E}^{(+)}(\vec{r},t)|i>\end{aligned} \tag{4.27}$$

As very few sources produce a pure quantum state when emitting light, the initial state $|i>$ in 4.27 is better described as a mixture, depending on uncontrolled or unknown parameters of the source.

The introduction of a density operator ρ, defined as $\rho = \{|i><i|\}_{av}$ can take into account the random properties of the state $|i>$. The average value of $\mathcal{P}_{fi}$ on repeated measurements of $\mathrm{I}(\vec{r},t)$ is then given by

$$\{\mathcal{P}_{fi}\}_{av} = Tr\{\rho\vec{E}^{(-)}(\vec{r},t)\vec{E}^{(+)}(\vec{r},t)\} \tag{4.28}$$

4.4.1 First order correlation

The light intensities measured in interference experiments depend on the overlapping of fields with different arguments, as already expressed by equation 4.10: the corresponding quantum correlation function is then defined as

$$G^{(1)}(\vec{r}_1,t_1;\vec{r}_2,t_2) = Tr\{\rho\vec{E}^{(-)}(\vec{r}_1,t_1)\vec{E}^{(+)}(\vec{r}_2,t_2)\} = \langle E^{(-)}(\vec{r_1},t_1)E^{(+)}(\vec{r_2},t_2)\rangle \tag{4.29}$$

The normalized expression of $G^{(1)}$ set in equation 4.29 is commonly used in practice; all "one-photon experiments" can be described by means of the correlation function $g^{(1)}$: special cases are those for which time and/or space parameter values are coincident.

In more detail, $\vec{r}_1 = \vec{r}_2$ and $t_1 \neq t_2$ characterize spectrometric devices, while $\vec{r}_1 \neq \vec{r}_2$ and $t_1 = t_2$ denote interferometric devices; finally, both $\vec{r}_1 = \vec{r}_2$ and $t_1 = t_2$ indicate a bolometric measurement. They are collectively referred to as first order correlation experiments.

4.4.2 Second order correlation

Glauber's theory shows its power when dealing with systems which involve more than one photon, e.g. to test the time distribution of arrivals to the photon counter or the spatial correlation of signals detected in different places, as first achieved by R. Hanbury Brown in his experiments.

In order to describe a detector with two different photon counters, the following matrix element is introduced

$$\mathcal{M}_{fi} = <f|\vec{E}^{(+)}(\vec{r}_1,t_1)\vec{E}^{(+)}(\vec{r}_2,t_2)|i> \tag{4.30}$$

corresponding to the absorption of two quanta from the initial state, one from each counter, here represented by the (commuting) destruction operators $\vec{E}^{(+)}(\vec{r}_1,t_1)$ and $\vec{E}^{(+)}(\vec{r}_2,t_2)$ respectively.

Following the same path of the previous definition of $G^{(1)}$, when $\mathcal{M}_{fi}$ in equation 4.30 is squared, summed over final states $|f>$ and averaged over the initial states $|i>$, a new correlation function of second order, $G^{(2)}$, is defined as

$$\begin{aligned} G^{(2)}(\vec{r}_1,t_1;\vec{r}_2,t_2;\vec{r}_2,t_2;\vec{r}_1,t_1) = \\ Tr\{\rho\vec{E}^{(-)}(\vec{r}_1,t_1)\vec{E}^{(-)}(\vec{r}_2,t_2)\vec{E}^{(+)}(\vec{r}_2,t_2)\vec{E}^{(+)}(\vec{r}_1,t_1)\} = \\ \langle E^{(-)}(\vec{r_1},t_1)E^{(-)}(\vec{r_2},t_2)E^{(+)}(\vec{r_2},t_2)E^{(+)}(\vec{r_1},t_1)\rangle \end{aligned} \tag{4.31}$$

The function $G^{(2)}$ quoted in equation 4.31 is a special case of the general second order correlation function (hereafter $x_j = \vec{r}_j, t_j$) $G^{(2)}(x_1x_2x_3x_4) = Tr\{\rho\vec{E}^{(-)}(x_1)\vec{E}^{(-)}(x_2)\vec{E}^{(+)}(x_3)\vec{E}^{(+)}(x_4)\}$.

The corresponding normalized form is

$$g^{(2)}(x_1,x_2;x_2,x_1) = \frac{G^{(2)}(x_1,x_2;x_2,x_1)}{G^{(1)}(x_1,x_1)G^{(1)}(x_2,x_2)} \tag{4.32}$$

It is worth noting that the first order coherence condition quoted in equation 4.14 does not imply any specific factorization property for $G^{(2)}$: an independent second order coherence can be set by the requirement that

$$G^{(2)}(x_1x_2x_3x_4) = \mathcal{E}(x_1)\mathcal{E}(x_2)\mathcal{E}(x_3)\mathcal{E}(x_4) \tag{4.33}$$

It can be derived from equations 4.33 or 4.32 that a quantum field is fully second-order coherent if the following factorization holds:

$$G^{(2)}(x_1x_2x_2x_1) = G^{(1)}(x_1x_1)G^{(1)}(x_2x_2) \tag{4.34}$$

With reference to the intensities $I(x_i) = |E(x_i)|^2$ of coherent fields, it was shown (for a full derivation, see [Man95]) that their fluctuations $\Delta I(x_i)$ are correlated too, following the rule

$$\langle \Delta I_1(x_i) \Delta I_2(x_j) \rangle = \frac{1}{2} \bar{I}_1 \bar{I}_2 g^{(2)}(x_1, x_2; x_2, x_1) \tag{4.35}$$

This leads to the relevant possibility of detecting the coherence degree of a field by means of intensity fluctuation measurements.

The full development of Glauber's theory naturally extends the definition of correlation functions G to the n-th order following the rule stated in 4.33 and defining n coherence conditions as in 4.12 and 4.34.

Here it will just be recalled that in principle there exist lots of fields that lead to the factorization of the complete set of $G^{(n)}$, some of them corresponding precisely to the fields generated by predetermined classic current distributions.

However, up to now the measurements of $G^{(n)}$ beyond second order have been inhibited by practical and technological limits.

A measurement of higher order $G^{(n)}$ will be possible within the Čerenkov Telescope Array (CTA) project, when many Čerenkov telescopes simultaneously operating in the same site can detect n-photon coincidences.

Present "two-photon experiments" are usually described by means of the correlation function $g^{(2)}$.

In more detail, $\vec{r}_1 = \vec{r}_2$ and $t_1 \neq t_2$ characterize a "correlation spectrometer", while $\vec{r}_1 \neq \vec{r}_2$ and $t_1 = t_2$ denote the intensity interferometer (like Hanbury Brown's); finally, both $\vec{r}_1 = \vec{r}_2$ and $t_1 = t_2$ indicate a "quantum spectrometer".

This field of research is often called "second-order interferometry".

Chapter 5

Quantum Astronomy: new goals for MAGIC-II

Many years have passed by since the Narrabri Intensity Interferometer was dismantled, and this kind of instrument has not been further developed, mainly because of the difficulties in improving such a device at a reasonable cost.

In the meanwhile, the quantum origin and the generality of the Hanbury Brown-Twiss effect was verified in many laboratory experiments on both bosonic and fermionic systems, in some case pushing the resolution up to single photon detection.

From the astronomical perspective, the last decades were enriched by many observations in various bands [Eli95, Tow97, Let02] which suggested the existence of laser emitting sources, i.e. objects whose character would be clarified at best by new instruments based on second-order time coherence measurements.

Merging with this evolving quantum optical and astronomical framework, the progress in electronics and optics technologies achieved in recent years has encouraged new studies and projects of photonic astronomy [Nal06, Dra08c] as a possible access key to a whole new class of phenomena.

It is worth noting that the present availability of optical devices with large mirrors and advanced electronics (like MAGIC or other IACT telescopes) has suggested the use of them also for time-correlation measurements.

In particular, the realization of some Čerenkov arrays, whose detection can be (at least in principle) extended to spatial-coherence measurements, has turned attention to a possible use of such telescopes as intensity interferometers [Dra06, Boh06].

In this chapter the use of MAGIC-II for quantum interferometric measurements will be discussed, starting from a brief review of the most recent instrumental achievements in quantum astronomy and keeping on with the identification of possible targets of interest. The project for the new instrument to be carried out will then be described in detail.

5.1 Present instruments for Q.O. astrophysical observations

To illustrate the presently available technology for quantum astronomy, two of the most recent instruments and measurements will be briefly described here: the AquEYE photometer and a test carried out in 2007 with two telescopes of the VERITAS array.

(a) (b) (c)

Figure 5.1: *(a) The Cima Ekar observatory; (b) the Copernicus telescope with AFOSC (blue) and (C) the AquEYE photometer (black) installed [Bar07].*

(a) (b) (c)

Figure 5.2: *(a) Optical outline of AquEYE; (b) the pyramidal splitter; (c) the mechanical design of AquEYE [Bar08].*

5.1.1 A modern time-correlator device: AquEYE

AquEYE (the Asiago QUantum EYE) [Bar07, Nal07, Bar08] is an ultra-fast photometer, installed at Cima Ekar (Italy) on to the 182 cm Copernicus telescope (see figure 5.1) as a prototype for the QuantEYE instrument studied for the ESO OWL in 2005 [Dra05].

AquEYE is coupled to the telescope through the imaging spectrometer AFOSC, which already provides an intermediate pupil and optical filters; the device can select a single object from the centre of the field of view and divide the telescope pupil into four parts (see figure 5.2).

Each sub-pupil is then focused on a SPAD (Single Photon Avalanche Diode [MPD], see figure 5.3), a quantum detector with an active area of 50 μm in diameter and efficiency exceeding 50% in the bandwidth from 500 to 600 nm [Bar08], tagging the incoming photons to better than 50 ps.

The four SPADs employed in AquEYE are integrated in self contained boxes with inner Peltier cooling stage and the time forming circuitry; the external dimensions of each unit are 50 mm $\times$ 98 mm $\times$ 40 mm.

The designed optical non-imaging solution of AquEYE concentrates all the light collected inside a 3 arcsec field on the detector sensitive area. Different filters can be inserted in the four optical paths (see figure 5.3.c).

The quantum efficiency achieved is remarkably high, but over a very tiny area: this is at present a limit to the astronomical employment of avalanche photodiodes like SPAD, which makes it difficult to collect extended images formed by large telescopes.

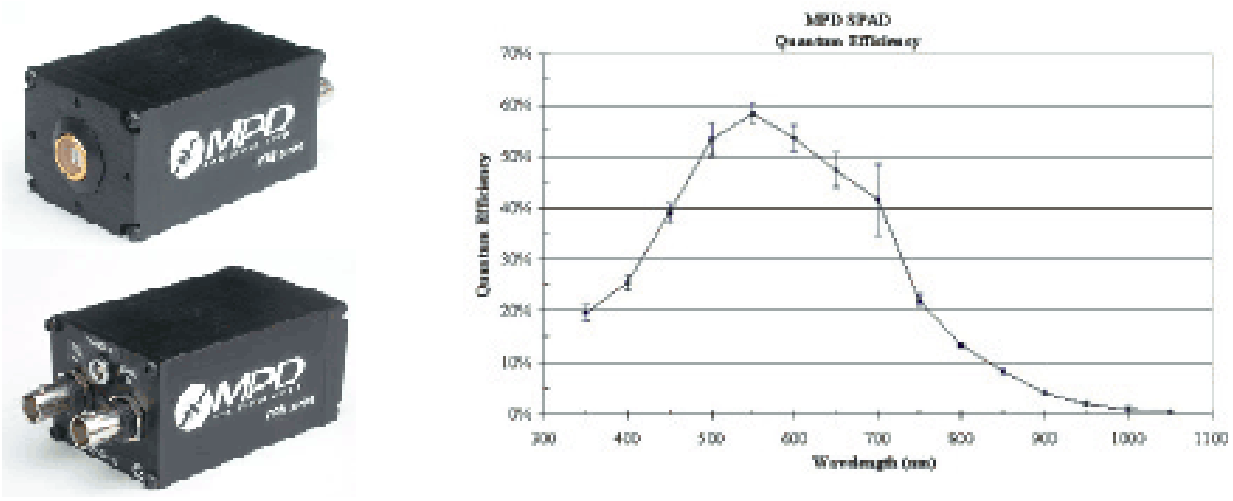

(a) (b)

Figure 5.3: *Spad: (a) external view and (b) quantum efficiency curve [Nal07].*

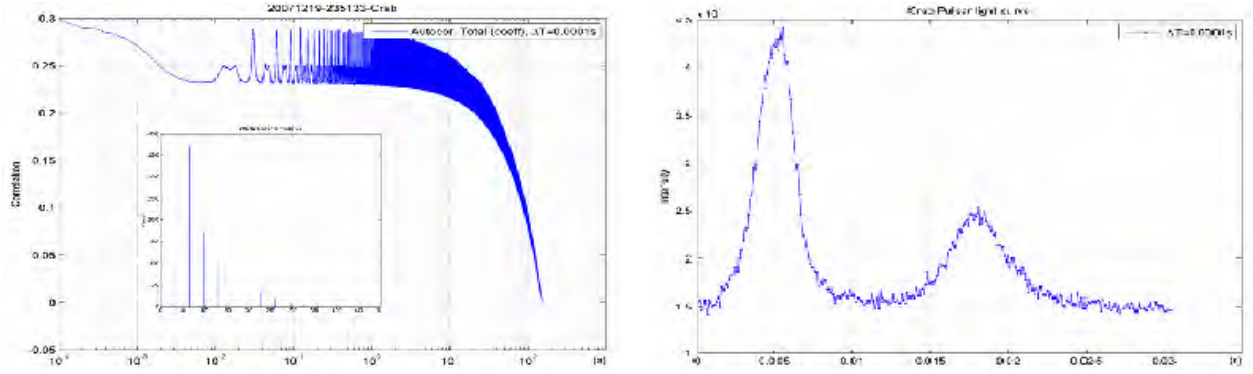

(a) (b)

Figure 5.4: *The AquEYE Crab optical observations: (a) the normalized autocorrelation function with 0.1 ms time bins with an example (inner window) of real time sampling used for the plot and (b) the obtained light curve (adapted from [Bar08]).*

The challenge becomes even higher if a wide range of wavelengths has to be focussed simultaneously, to exploit a detector's broad spectral response. In order to extend the size of the sensitive area, the production of SPAD in arrays is under study.

The counts are acquired via a Time to Digital Converter board and stored in four separate memories; in order to reach the time tagging precision required, the original TDC board built by CAEN was integrated with an external frequency reference Rubidium oscillator and provided with a GPS receiver for the UTC reference.

AquEYE was created to study different astrophysical objects characterized by rapid variability in time as pulsars, X-ray binaries, pulsating white dwarfs or neutron stars, etc.

The nominal performance would allow the observation of faint optical sources up to magnitude $m_V = 20$, the real limiting factor ($m_V \simeq 17$) being the Ekar average sky brightness.

Since the beginning of its activity, AquEYE repeatedly observed the 33 ms optical pulsar in the Crab Nebula ($m_V = 16$) for check and reference calibration purposes [Bar08].

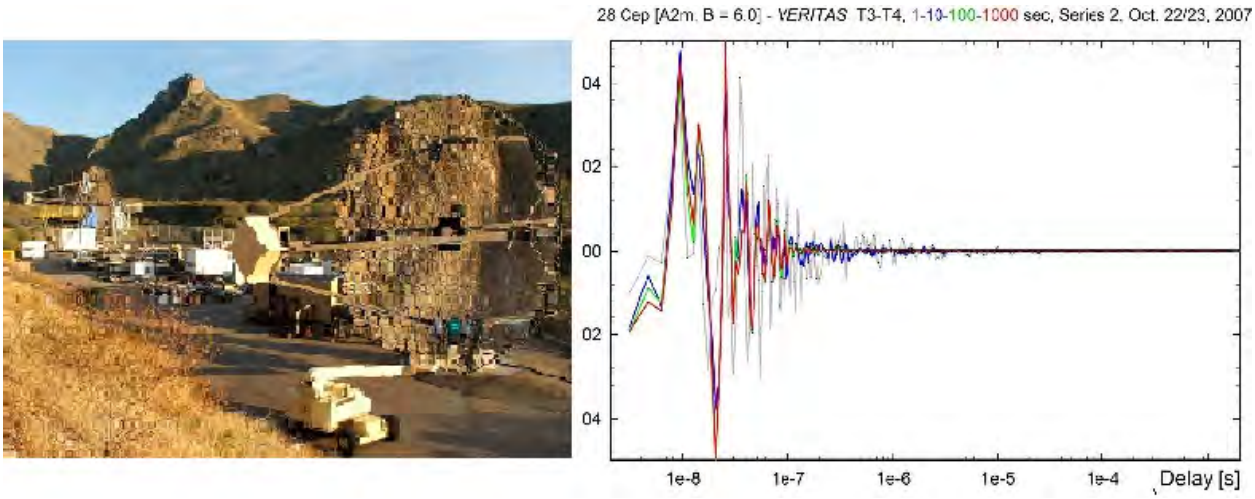

(a) (b)

Figure 5.5: *(a) A couple of VERITAS telescopes, used as flux collectors for this measurement [VER]; (b) the intensity cross-correlations measured between two VERITAS telescopes for the star 28 Cep (A2m; $m_V = 5.8$). The four curves illustrate how the signal converges as the integration times increase in steps of 1-10-100-1000 seconds [Dra08c].*

Some of the Crab signals measured in December 2007 are reported in figure 5.4 as an example of AquEYE potentialities.

5.1.2 A modern space-correlation test with VERITAS

The possibility of coupling digital electronics and existing Čerenkov telescopes to perform intensity interferometry on new time/space scales was successfully tested in October 2007, employing two of the 12 m diameter telescopes of the VERITAS arrays, for a baseline of 85 m [Dra08c].

During this test, a photon-counting photomultiplier in the central pixel of the regular Čerenkov-light camera was employed to detect starlight; the outgoing photon pulses were digitized using a discriminator, pulse-shaped to a width down to some 5 ns, and then transmitted from each telescope to a real-time digital correlator in the control house via optic fibres.

The cross-correlation function between the two signals was determined with a time resolution of 1.6 ns for different time delays (digitally introduced for the analysis), matching with a continuous count rate up to 30 MHz, limited by the digitization and signal-shaping electronics.

The effective measurement, as documented in figure 5.5, can be regarded as the first case of optical astronomical telescopes having been connected for real-time observations through e-interferometry by digital software rather than by optical links.

At the same time, this test encourages the development of new digital correlators as well as the study of different possibilities to couple intensity inteferometrical devices with the existing Čerenkov arrays [Boh06, Boh08], especially in view of the CTA realizations in the near future, which will provide an extended full range of baselines.

5.2 The possibilities of new CTA mirrors

The recent building of telescopes larger than 10 m in diameter, together with the great improvements in electronics made since the 1970's allows the construction of new intensity interferometers

Telescope diameter (m)	Intensity <I>	Second-order correlation <I²>	Fourth-order photon statistics <I⁴>
(TNG) 3.6 m	1	1	1
(HBTII) 2 × 6.5 m	6	42	1,800
(VLT) 4 × 8.2 m	21	430	185,000
(MAGIC-II) 2 × 17 m	44	1980	3,950,000
E-ELT 42 m	136	18500	343,000,000

Figure 5.6: *The Intensity dependence from the mirror surface.*

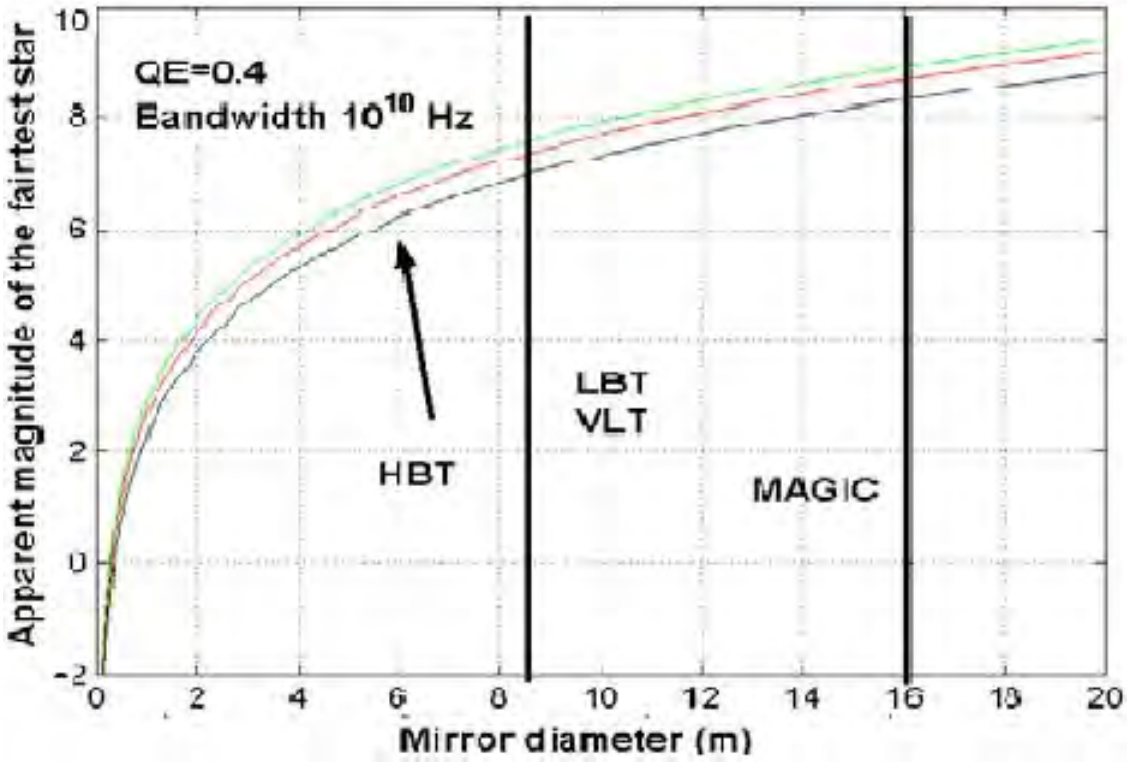

Figure 5.7: *The minimum mirror diameter needed to achieve S/N = 3 in 1h, 2h, 3h at a given m_V magnitude, assuming a QE of 0.4 and an electrical bandwidth of 10^{10} Hz. The curve show the capabilities of VLT, LBT and MAGIC. The arrow HBT indicates the maximum magnitude achieved by HBTII after a week-long integration [Dra05].*

much more effective than the original Narrabri one, which used fully analogic components.

The number of collected photons and the intensity $< I >$ depend on the square of the diameter, while the second order correlation term $< I^2 >$ depends on its fourth power.

Due to this strong dependence of the correlation parameters on the mirror area, the use of MAGIC two mirrors (as well as greater future ELTs) would open to observations a new range of sensitivity, as quoted in table 5.6.

The sensitivities presently reachable are illustrated in figure 5.7: the maximum value reached by HBTII is also shown for comparison.

A second improvement comes from the increased quantum efficiency of present photodetectors with respect to HBTII; the quantum efficiency of a SPAD or of the most recent PMTs [Goe07a] can roughly double the S/N ratio (cfr. eq. 4.22) with respect to Narrabri's photomultipliers.

It should also be mentioned that a further increase in MAGIC quantum efficiency is already planned, with the substitution of part of the PMTs with more sensitive HPDs detectors [Sai07] or SiPM presently under study [Tes07c].

Further improvements with respect to HBTII are also possible with the introduction of wider bandwidths and better optical elements; as a numerical example, a conservative[1] estimation of the sources within reach of the MAGIC telescopes used as Intensity Interferometer made via eqn. 4.22 gives a detectable (at 5σ level) visual magnitude $m_V \simeq 6$ for an unresolved star ($|g^{(2)}(d,0)|^2 = 1$) in the zenith in one hour of observation.

Last but not least, the simultaneous presence on the same site of two similar telescopes at a distance of 85 m, joined with a reliable timing source for synchronization and integrated with tunable digital time delays, makes the space correlation measurements possible on different nominal baselines up to the effective separation length (see figure 5.14).

All these considerations strongly encourage the implementation of quantum astronomy detectors on CTAs and notably on MAGIC-II, in view of extended observations and new astronomical perspectives.

5.3 Observational targets for quantum astronomy

When a light beam is treated as a photon stream it becomes evident that more information about the source can be extracted from experimental detection than the single photons properties: a further degree of freedom of such a quantum system is related to the statistics of photon arrival times.

As photons have integer spin, the beam can be properly described as a boson gas: the measurement of correlation in time (or space) between a couple of photons (or more) will then give an insight on the entropy of the beam, which is on its turn expression of the emission mechanism.

The different distributions are a collective property of the beam and they can not be attibuted to a single photon.

The measurement of the second order time correlation factor

$$g^{(2)}(\tau) = \frac{< I(t) \cdot I(t+\tau) >}{< I(t) >^2} = g^{(2)}(-\tau) \tag{5.1}$$

for an astronomical source would then give precious information on the emission mechanism, not available with other techniques.

The present scenario is rich in phenomena showing interesting quantum astrophysical features: a useful grouping can be introduced between time- and space-correlation effects to be detected.

[1] The values introduced for MAGIC-II are $A = 236\,\mathrm{m}^2$, $\alpha = 0.34$, $\Delta\mathrm{f} = 500\,\mathrm{MHz}$ [Goe07a]. An overall optical attenuation factor $\Sigma = 0.4$ has been quoted for.

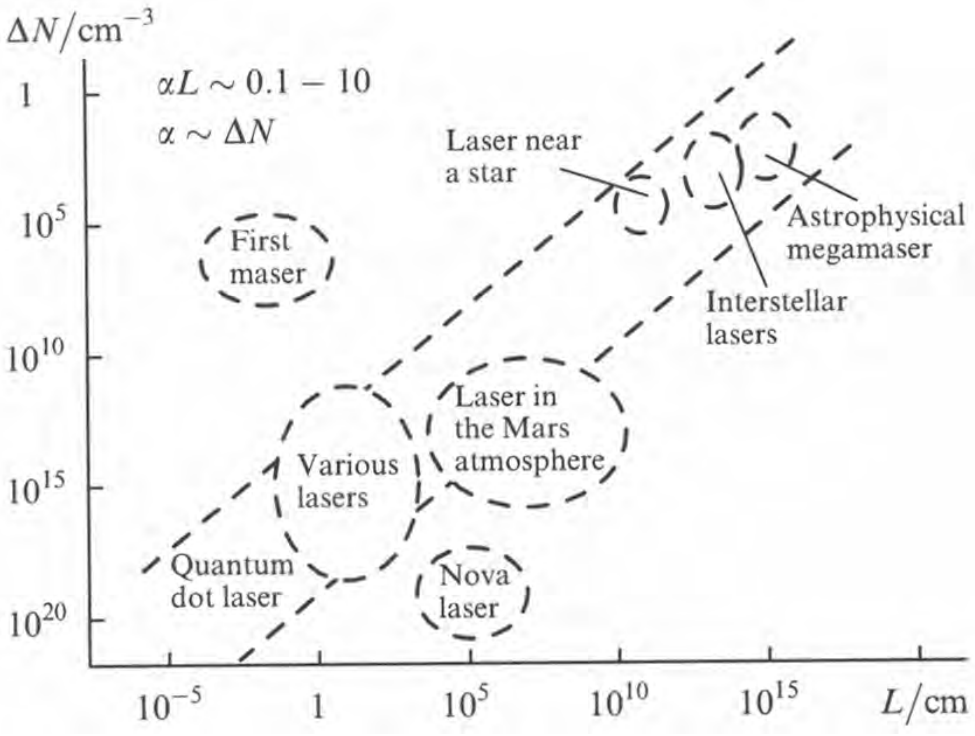

Figure 5.8: *Masers and lasers in the active medium particle-density vs dimension diagram [Let02].*

5.3.1 Time correlated targets

Many observations indicate the existence of different astrophysical laser sources (see figure 5.8): in particular, the gas cloud observed near Eta Carinae which acts as natural ultraviolet laser source [Joh02, Joh04, Joh07] (see figure 5.9). The possible use of correlation interferometry technique to measure the corresponding emission lines from this source both in UV and in visible has been suggested [Joh05].

As traditional methods of observation cannot discriminate the ultimate mechanism of light emission, these sources stand as immediate targets to be directly investigated by means of quantistic time-correlation effects. This technique would undoubtedly confirm the nature of the radiation, giving at the same time stringent indications on the production mechanisms.

Laser emission from astrophysical sources and from stable laboratory devices have different temporal features: while the basic processes are the same, the absence of mirrors in resonance cavities limits astrophysical lasering to short (with reference to coherence time) monochromatic emissions (partial laser action).

The beams triggered by one spontaneously emitted photon will be confined in narrow angles along its flight line out from the source, while the path where the photon train has passed becomes temporarily deexcited and remains so for perhaps a microsecond until collisions and other effects have restored the balance.

The stimulated emission from astrophysical sources requires the inversion of population in atomic levels, which can be induced by different mechanisms; partial laser action might occur in atomic emission lines from extended stellar envelopes or stellar active regions. Predicted locations are mass-losing high-temperature stars, where the rapidly recombining plasma in the stellar envelope can act as an amplifying medium. Analogous effects could exist in accretion discs.

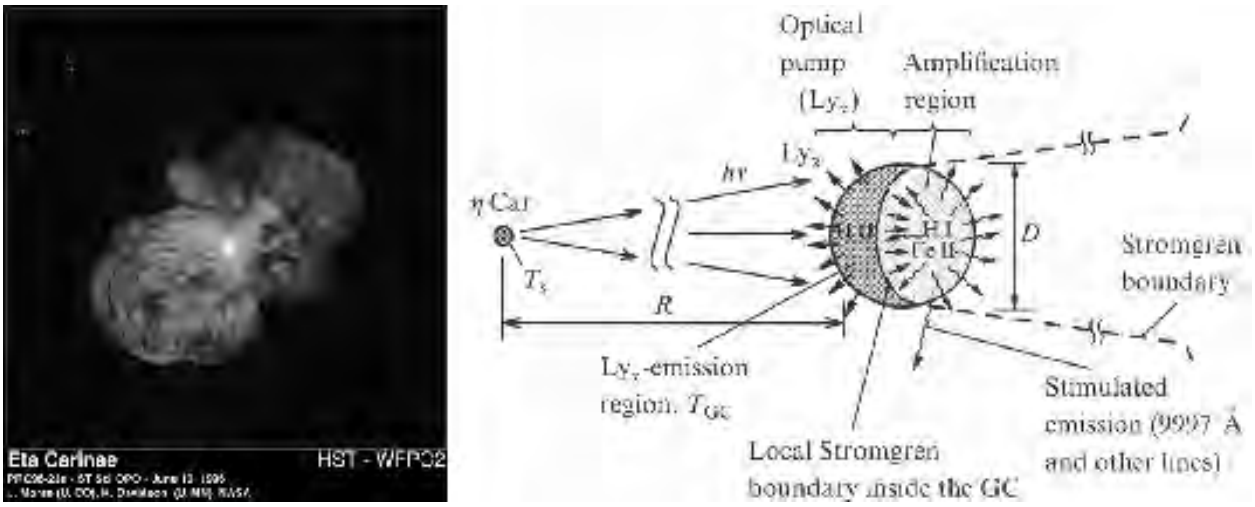

(a) (b)

Figure 5.9: *(a) Eta Carinae (image credit: NASA-HST) and (b) model of compact gas condensation near η Car with possible laser emission [Joh02].*

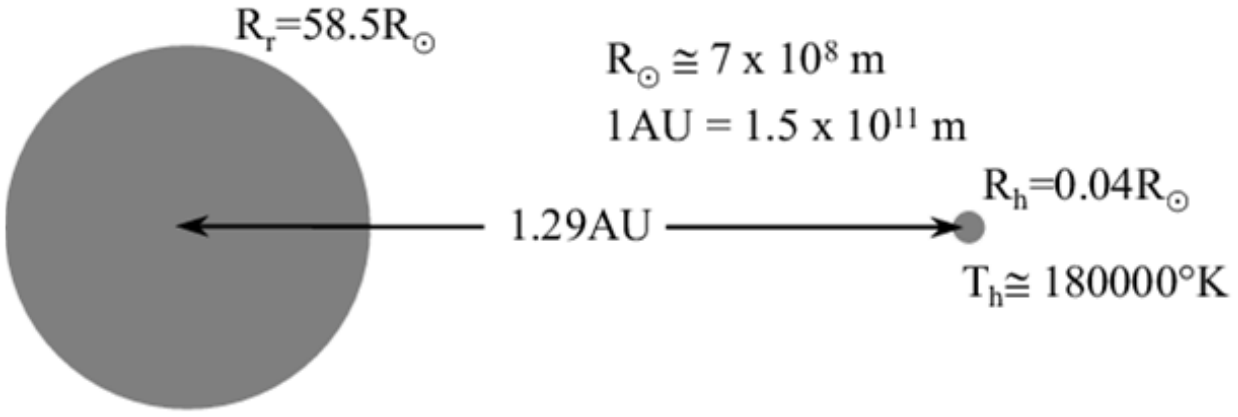

Figure 5.10: *Sketch of the symbiotic star RW Hydrae [Sor02].*

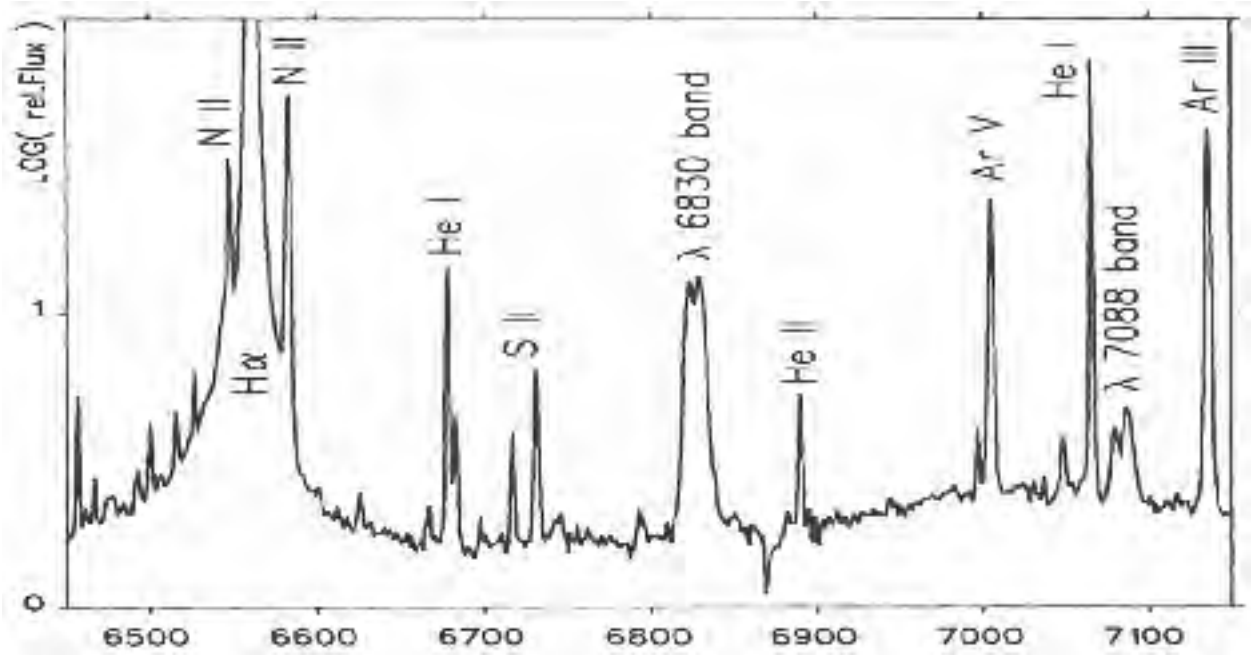

Figure 5.11: *Raman scattered emission bands in the symbiotic star V1016 Cyg [Sch89].*

Many Wolf-Rayet stars exhibit spectra with possible laser lines in various bands (see e.g. [Joh07]: the origin and spectral features of their emission makes could be better investigated by means of intensity interferometrical observations.

A somewhat similar geometry is found in symbiotic stars (e.g. RW Hydrae, see figure 5.10), which are close binary systems where a hot star ionizes part of an extended envelope of a cooler companion, leading to complex radiative mechanisms.

Their combined emission spectrum shows the superposition of absorption and emission features together with irregular variability.

Where strong ultraviolet emission lines of highly ionized atoms (e.g. O VI lines $\lambda = 103.2$ nm, $\lambda = 103.8$ nm) irradiate high-density regions of neutral hydrogen (with the Ly β line at $\lambda = 102.6$ nm), Raman-scattered lines may be observed [Sch89], like the $\lambda = 682.5$ nm and $\lambda = 708.2$ nm features in the symbiotic star V1016 Cygni (see figure 5.11).

With regard to pulsar emissions, proposed mechanism include stimulated synchrotron and curvature radiation (free-electron lasers) which should exhibit non-chaotic statistical features with $t_{coh} \sim$ ns.

Anyway, all evidence is still indirect, as the laser lines have not yet been spectrally resolved. These lines have been theoretically estimated to be extremely narrow, requiring spectral resolutions presently unachievable with ordinary spectroscopy.

On the contrary, a correlation spectrometer reaching the nanosecond timescale could measure the autocorrelation function of photon arrival times to obtain the coherence time and consequently the spectral linewidth.

Last but not least, an instrument with a nanosecond temporal resolution could clarify the relationship between the still unexplained giant radio bursts from the Crab pulsar [Han03] and the contemporary improved optical activity [She03].

It is worth noting that the Crab pulsar could be easily observed in a parasitical way with an intensity interferometer whenever it is pointed from MAGIC as gamma source, as already realized

with the optical observations with the MAGIC-I central pixel.

The same possibility stands for all the γ-ray observational targets for MAGIC which show at the same time interesting features to be studied in the optical range: this could have been e.g. the case of the recently observed Wolf-Rayet binary systems 146 and 147 [MAG08g].

To summarize, a first list of possible targets for MAGIC implemented with a correlation spectrometer working in the optical band could include:

- WR6 (visual magnitude $m_V \sim 6$) with regard to the He I ($\lambda = 492.1.2$ nm and $\lambda = 667.8$ nm) and He II ($\lambda = 468.6$ nm) lines;
- RW Hydrae or some other binary system with regard to laser emission;
- the symbiotic star V1016 Cygni, with regard to the Raman effect lines $\lambda = 682.5$ nm and $\lambda = 708.2$ nm
- the Crab pulsar, with regard to the temporal structure of its emission.

5.3.2 Space correlated targets

A new intensity interferometer would allow the resolution of stellar dimension and surfaces in details, thus leading to a deeper understanding of the mechanisms involved in stellar formation and evolution, like the mass accretion process, the continuum emission variability, the magnetic activity...

The imaging of stellar features like the hot spots gives direct information regarding the accretion of material onto the stellar surface; a precise resolution of the cool spots, which are the product of the slowly decaying rapid rotation of young stars, would constrain the models on rotation, convection and chromospheric activity, also probing the anomalous photometry observed in young stars.

Several young stellar groups have been identified within 50 pc from the Sun, e.g. the TW Hydrae and β Pictoris comoving groups; most of their stars belong to spectral types between A and G types, giving a sample of about 50 different young stars with magnitude $m_V \leq 8$ as possible targets.

Intensity interferometry on a more accurate scale with respect to HBTII would also allow the study of the fast rotators like the classical Be stars, well-known for being close to break-up rotational velocities as deduced from photospheric absorption lines.

Many questions remain open on the detailed physical processes related to those objects, e.g. the disc formation and dissolution activity, which is little understood. Photometric observations of star discs seem to indicate that they may actually evolve into ring structures before disappearing into the interstellar medium.

There are about 300 Be stars brighter than $m_V \leq 8$ on which such phenomena could be extensively probed by means of a new intensity interferometer.

The study of binary systems, most of them still visually unresolved, would also profit from intensity interferometry imaging; an instrument working with a resolution better than the milliarcsecond scale would result in the high precision imaging required to map for the first time the colliding-wind region between two symbiotic stars, possibly identifying the shock fronts with their instabilities and distortions.

It is worth noting that the precise angular measurements obtainable with an intensity interferometer are of main importance in the determination of the distance scale of the Cepheids.

A radius estimate of a Cepheid can be obtained using the Baade-Wesselink technique, which relies on the ratio of the star sizes at different times t_1 and t_2 based on luminosity and colour.

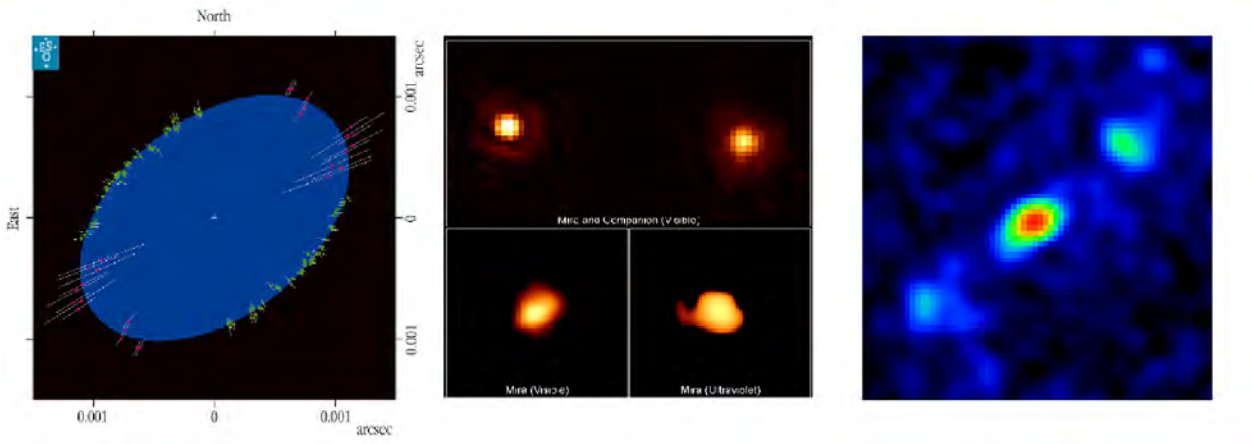

(a) (b) (c)

Figure 5.12: *Some of the possible targets for a new intensity interferometer: (a) Achernar (α Eri), (b) Mira Ceti, (c) CH Cygni.*

Once the radius has been calculated and combined with an independent measurement of the angular size, the distance to the Cepheid can be properly determined. This procedure allows the calibration of all the important Cepheid period-luminosity relations using local Cepheids.

To summarize, many stellar objects, interesting for peculiar features and unresolved questions, would be possible targets for a new intensity interferometer; a tentative list could be the following (see also figure 5.12):

- Achernar (m_V = -1.7) as archetype of Be stars (major axis 2.13 $\mp$ 0.05 mas, polar axis 1.51 $\mp$ 0.02 mas) for stellar surface studies;
- EG Andromedae ($m_V = 7.1$), a S-type symbiotic star, for possible resolution;
- Mira Ceti (present $m_V = 6.0$), for insights in the colliding-wind region;
- CH Cygni ($m_V = 7.1$), a symbiotic star showing peculiar features like jets in radio and optical band, X-ray emission, rich and complex mineralogy of the interstellar dust;
- a sample of Cepheids, for accurate probing of the Distance Scale (a fast survey of Hypparcos catalogue [HIP] gives at least 60 stars with $m_V \leq 8$ within reach of a precise intensity interferometer).

5.4 MAGIC possibilities in Quantum Astronomy

The present features and foreseen improvements of MAGIC-II encourage the development of its possible applications in the domain of Quantum Astronomy.

5.4.1 MAGIC-II features for time-correlation detection

As already illustrated in detail in section 2.2, the electronics chain for the second telescope of MAGIC-II has been projected to work with an overall bandwith of 500 Hz [Goe07a].

The present resolvable time is then 2 ns, with the possibility of reaching the nanosecond with adequate electronics upgrades. In analogy with the AquEYE solution, the 2 GHz internal clock of

Source	Emission line	Telescope diameter (m)
η Carinae ($m_V \sim 7$)	FeII (λ 9617$\mathring{A}$, λ 9913$\mathring{A}$) OI (λ 8446$\mathring{A}$)	~ 10
WR 6 ($m_V \sim 7$)	HeI (λ 4921$\mathring{A}$, λ 6678$\mathring{A}$), HeII (λ 4686$\mathring{A}$)	~ 10
WR 7 ($m_V \sim 12$)	HeI (λ 4921$\mathring{A}$, λ 6678$\mathring{A}$) HeII (λ 4686$\mathring{A}$)	~ 30

Figure 5.13: *Telescope diameters required for quantum interferometry on various sources. Several spectral lines of suspected laser emission are listed [Dra08b].*

the DOMINO Sample Ring ADC system [Tes07a] can fulfil the high precision timing required for time correlation at nanosecond scale.

The present quantum efficiency of MAGIC-II PMTs is $\alpha = 34\%$ in the selected optical band [Goe07a], but the improvement foreseen with the introduction of new HPDs should push it up to 50% [Sai07].

The mirror of MAGIC-II, with its 17 m diameter, is built with high isochronicity and an average reflectivity of 90% [Bas07].

A recent study [Dra08b] indicates that telescopes with the overall performance of MAGIC-II would suit the requirements to detect candidate sources for laser emissions both for specific stars, as indicated in table 5.13, and for general purpose photon spectrometry.

5.4.2 MAGIC-II features for space correlation measurements

The performance of present electronics allows the use of telescopes at fixed distance to span a multiple baseline interval with space-correlation measurements. The nominal baseline, which should be kept perpendicular to the distance from the star along its transit over the telescopes (see figure 5.14), is obtained once digital time delays are inserted in the correlation system to compensate for the varying path lengths to the two telescopes: a prolonged observation with proper delay tuning will then result in measurements spatially correlated on different baselines.

An intensity interferometer implemented on MAGIC-II will give possible baselines ranging from 10 to 85 m.

As the angular resolution of the intensity interferometer depends on the employed baseline, the range of resolutions achievable using MAGIC-II can be estimated in the scale of 0.1 mas (see figure 5.15). It is worth noting that the minimum baseline required to achieve the μas resolution scale is over 100 m.

The sensitivity achievable with such an interferometer would be superior to that of HBTII by a factor of 50, as can be seen in figure 5.16; the range of observable sources could be pushed up to m_V=9.6 with long-interval integrations, the limit being given by the PSF =0.05° (Point Spread Function) of MAGIC mirror, with its unavoidable integration of the night sky around the source.

The first MAGIC telescope was already implemented in 2005 with a single central pixel dedicated to optical observations, mainly on the Crab pulsar [Luc05a, Luc08].

The adopted solution, illustrated in figure 5.17, employed basically the same elements of the

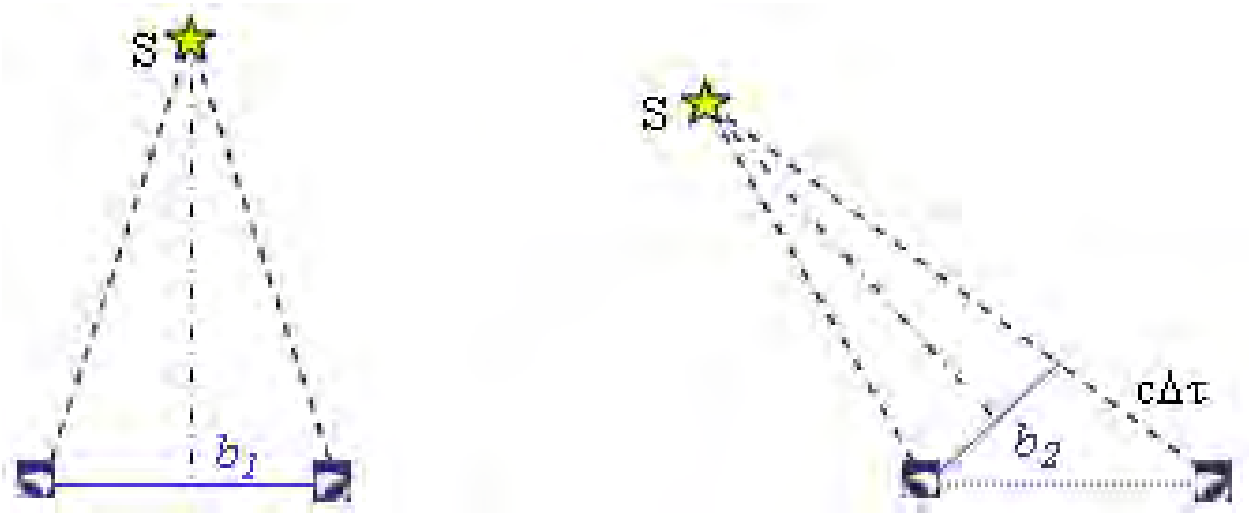

(a) (b)

Figure 5.14: *The same star S gives different baselines b_1 and b_2 for space-correlation measurements from different positions (a) and (b) along its transit, once the varying paths to the two telescopes are equalized by proper time delays $\Delta\tau$.*

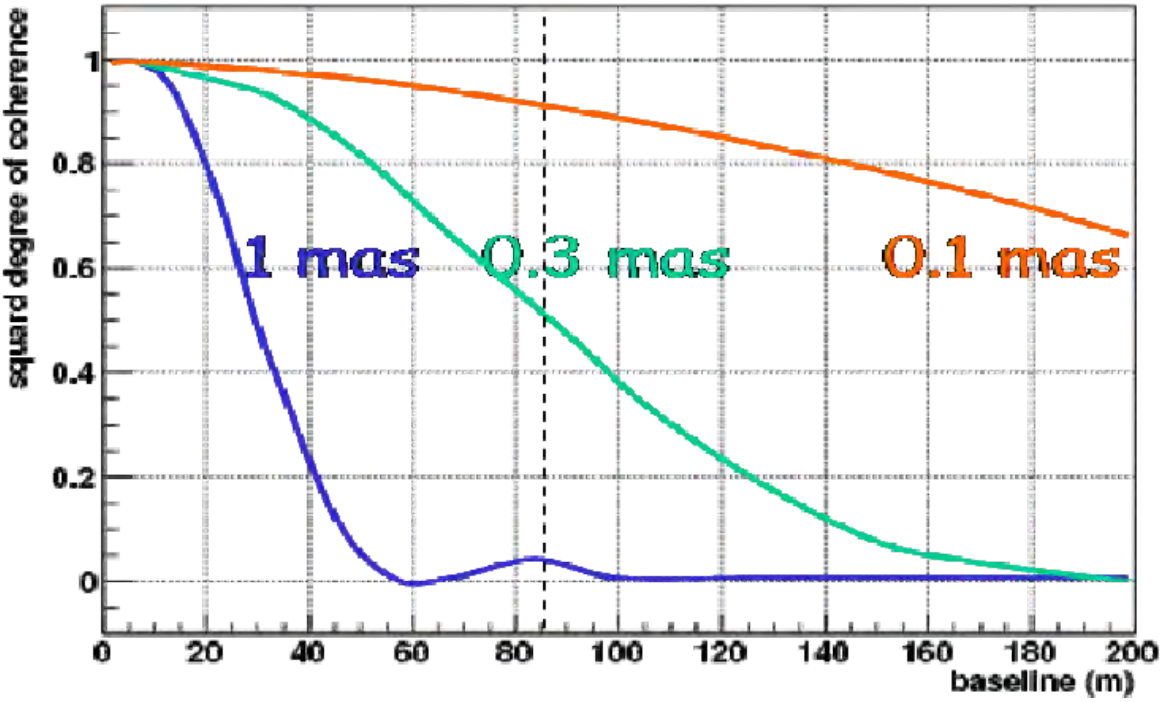

Figure 5.15: *The squared degree of coherence $|g^{(2)}|^2$ vs the baseline of a two telescope Intensity interferometer is plotted for different diameters of the sources (uniform disc model, $\lambda = 440$ nm), namely 1 mas (blue), 0.3 mas (faint green) and 0.1 mas (orange). The dashed line indicates the maximum baseline of MAGIC-II as intensity interferometer.*

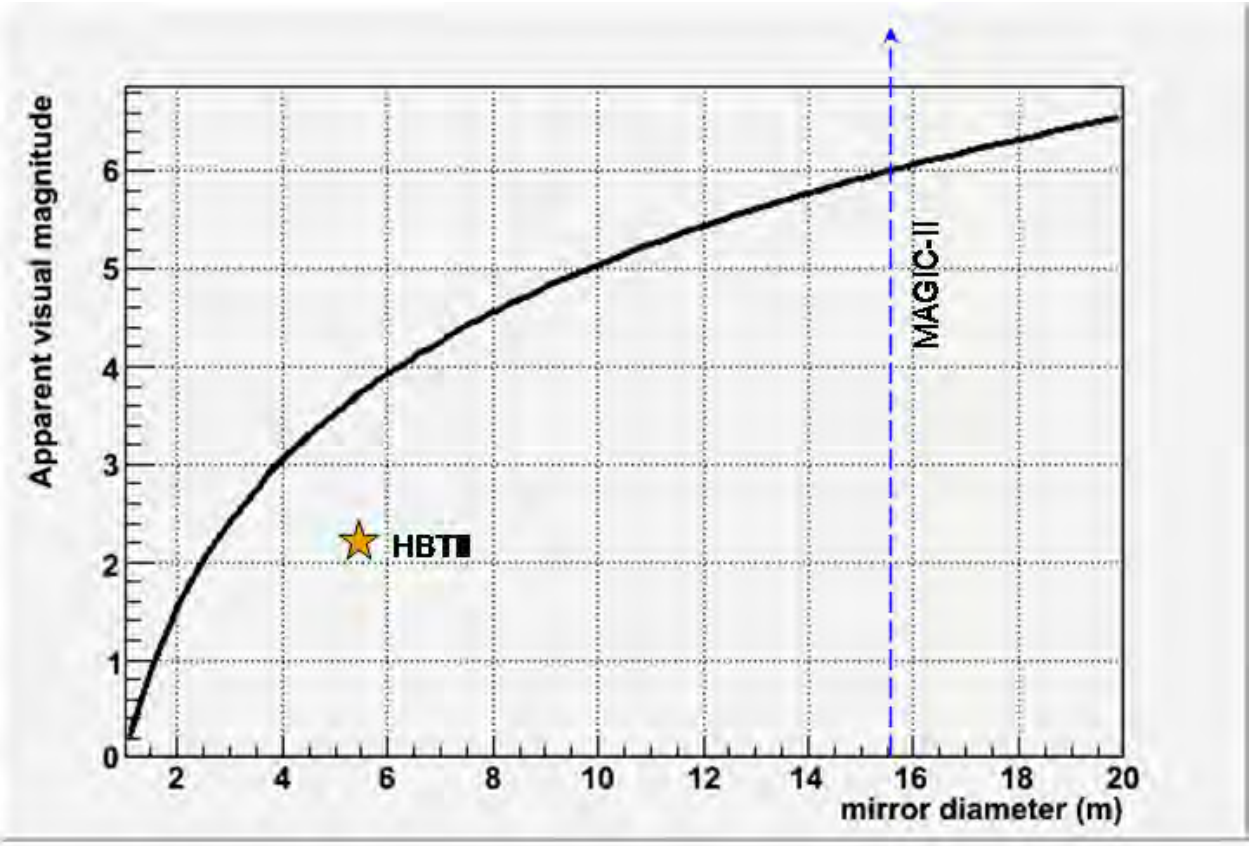

Figure 5.16: *The visual magnitude m_V of the source is plotted vs the mirror diameter: the curve represents the faintest source detectable in one hour at 5 σ level by an interferometer with electronic and optical features like MAGIC; the yellow star indicates the working point of HBTII, while the blue dashed arrow identifies the MAGIC detection range.*

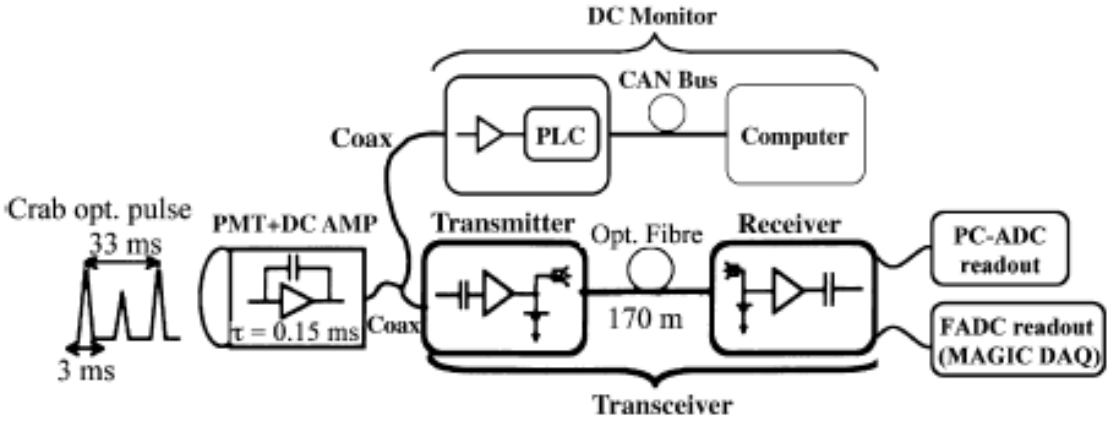

Figure 5.17: *Block diagram of the MAGIC-I optical central pixel and its readout [Luc08].*

other pixels (mirror, PMT, transmission line), while some modifications were required in the DC-branch of the preamplifier and in the transceiver bandwidth to optimize the performance in the millisecond scale, matching with the Crab pulsar periodicity.

The readout was performed independently by a standard FADC of MAGIC modified to cope with the slow signals (1 Hz – 10 kHz) of the central pixel and by a PC-ADC continuously sampling the signal up to 20 kHz.

The operating conditions were in part limited by various factors, such as the contemporary Čerenkov detection or the partial moonlight illumination: nevertheless, the Crab optical pulsar was always resolved at 5 σ level within 20 – 30 s, allowing precise determination of the lightcurve, as shown in figure 5.18.

5.4.3 Project of the new interferometer

This previous success, achieved some years ago by the first MAGIC telescope with worse performance in comparison with the present, confirm the reliability of the MAGIC system also for optical observations and encourages the introduction of the modifications needed to push the system towards the quantum measurements domain.

A straightforward solution for implementing a quantum interferometer on the MAGIC stereo system is the integration of a central pixel detector suitable for single-photon detection on both telescopes.

The Hamamatsu R10408 PMTs (see figure 5.19.b) fit the requests of quantum efficiency, fast response, low gain and linearity needed to record the Čerenkov fast light pulses [HAM]. These PMTs are presently mounted in MAGIC-II camera grouped by seven in a hexagonal socket (see figure 5.19.a), which allows fast integration or substitution, enhancing the single mounting in the "swiss cheese" support which characterized the first MAGIC telescope.

Due to its characteristics, the R10408 PMT is also suitable as an active element of the quantum interferometer central pixel (QIP in the following).

Quantum interferometry requires the selection of a narrow band $\Delta\lambda$ around the wavelength fixed for observations: an optical filter is needed to select the incident light.

Typical values of bandwith are in the range from 2 to 20 nm, with a transmission coefficient around 50% for commercially available filters. A suitable filter is e.g. 25 mm in diameter, 7 mm thick, with $\lambda = 490^{+10}_{-0}$ nm, bandwidth 10 nm and Tx = 55% [AND].

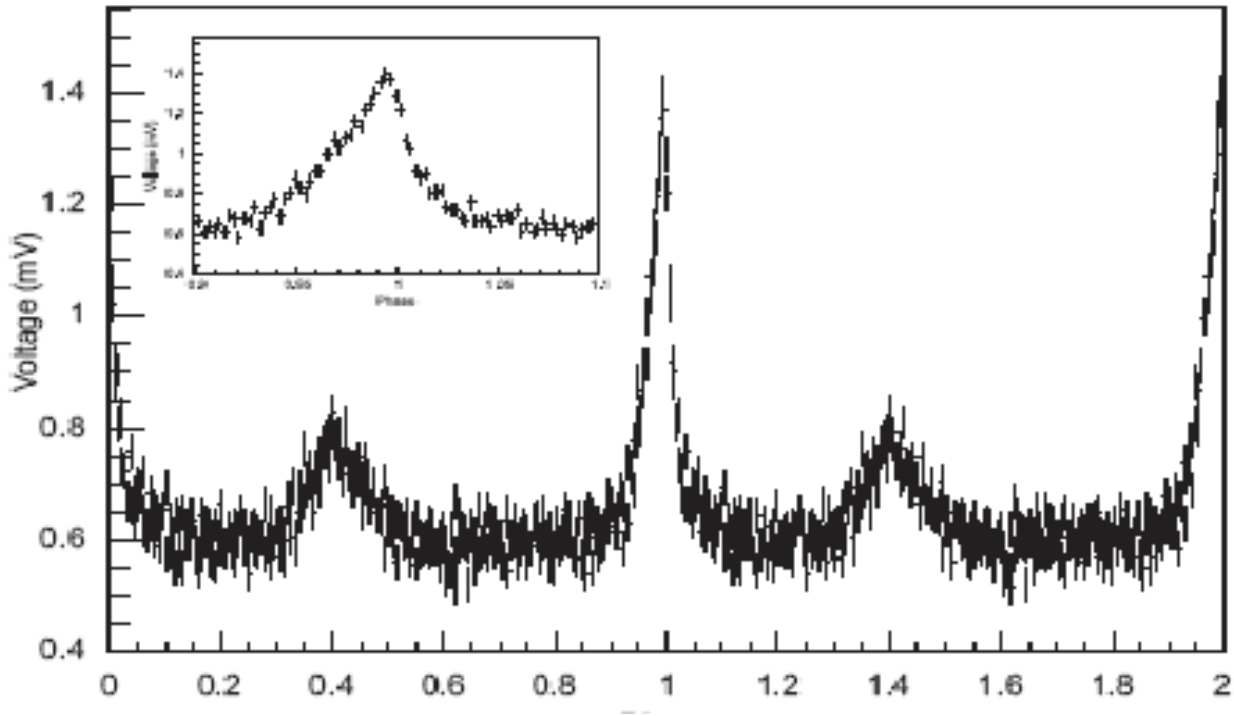

Figure 5.18: *The Crab light-curve obtained with the MAGIC-I central pixel for the frequency corresponding to the χ^2 maximum and for a duration of 40 min of observation. Inset picture shows a zoom of the lightcurve around its main peak (at phase 0)[Luc08].*

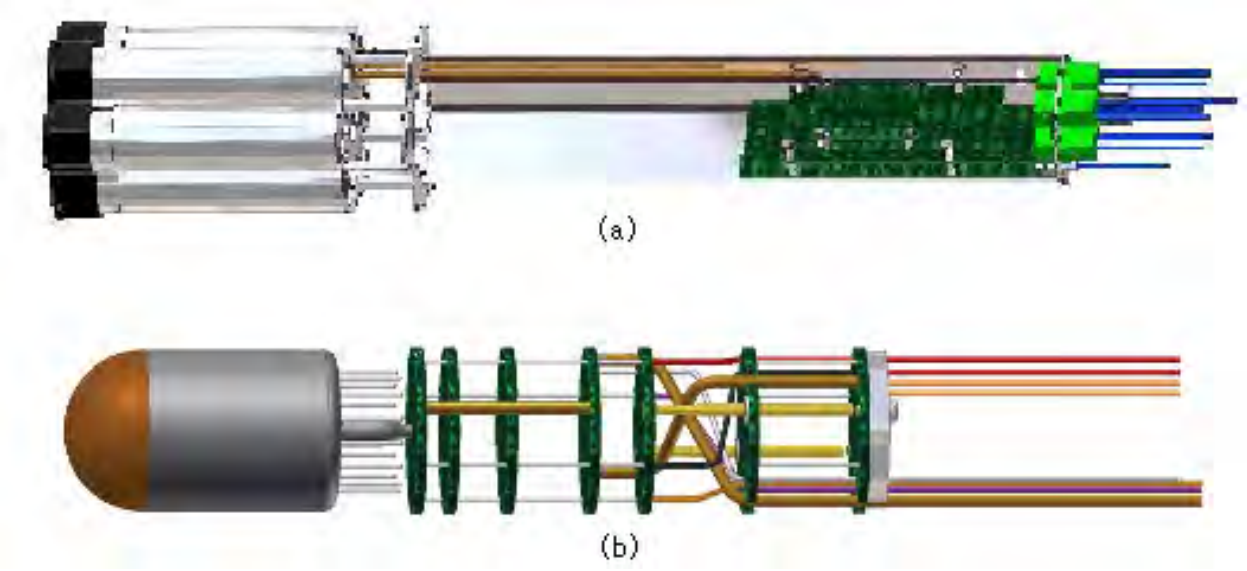

Figure 5.19: *The MAGIC-II PMT system: (a) outline of the 7 PMT hexagonal module and (b) of a single R10408 PMT [Goe07a].*

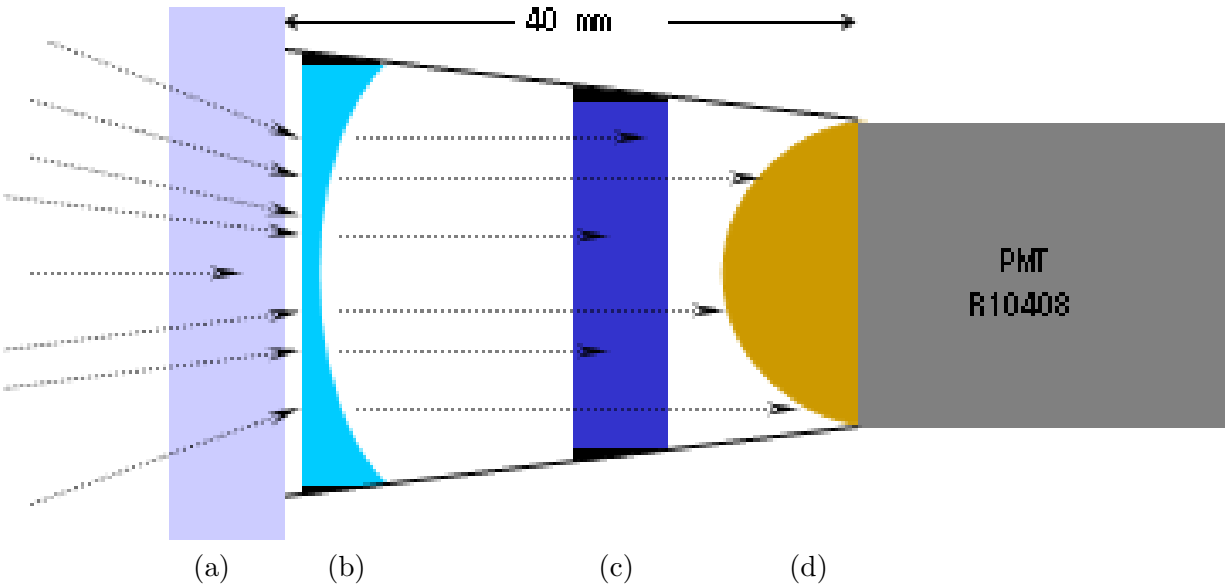

Figure 5.20: *Outline of the optical solution for the MAGIC-II central pixel: (a) plexiglas window of the camera; (b) negative lens; (c) optical filter; (d) photocatode.*

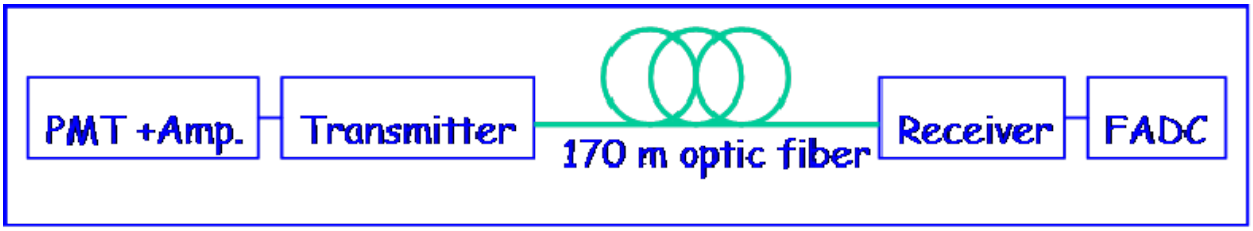

Figure 5.21: *Outline of the standard MAGIC-II electronics chain.*

As the filter response depends on the incidence direction of the light, which should be kept perpendicular to the filter surface, a negative lens is recommended to align the photons coming from the mirror with different incidence angles before they pass through the filter. The plexiglas foil protecting the Camera at the same time limits the space available in front of the PMT to 40 mm.

This gap is suitable to host both the filter and a lens properly designed: figure 5.20 is a sketch of the optical solution of the project.

In the standard MAGIC-II pixels, the light which comes in through the plexiglas window is concentrated on the PMT surface by a Winston cone to collect as many photons as possible on the active area. Even if photon reflections between the lens and the filter would not be recommended in the QIP, the cone is nevertheless useful as mechanical support for the optical added elements.

The electronic chain of MAGIC-II from the PMT to the control room is sketched in figure 5.21. It is worth noting that the 500 MHz value quoted for the overall bandwidth [Goe07a, Hsu07] is to be intended conservatively: the output bandwidth of R10408 PMTs is indeed wider (700 MHz), other components work on an even wider range, so future improvements in bandwidth up to 1 GHz can be realistically expected.

In order to avoid contaminations in data taking, a veto against Čerenkov photons must be set, which can be supplied by the pixels closely surrounding the QIP. Overlapping of more photons

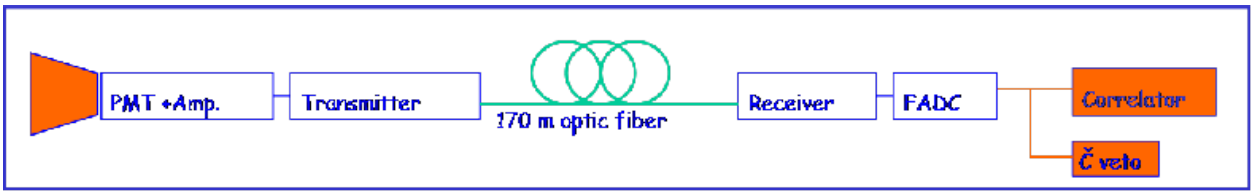

Figure 5.22: *Outline of a correlation spectrometer project for MAGIC-II: the orange bakground indicates the new elements to be integrated.*

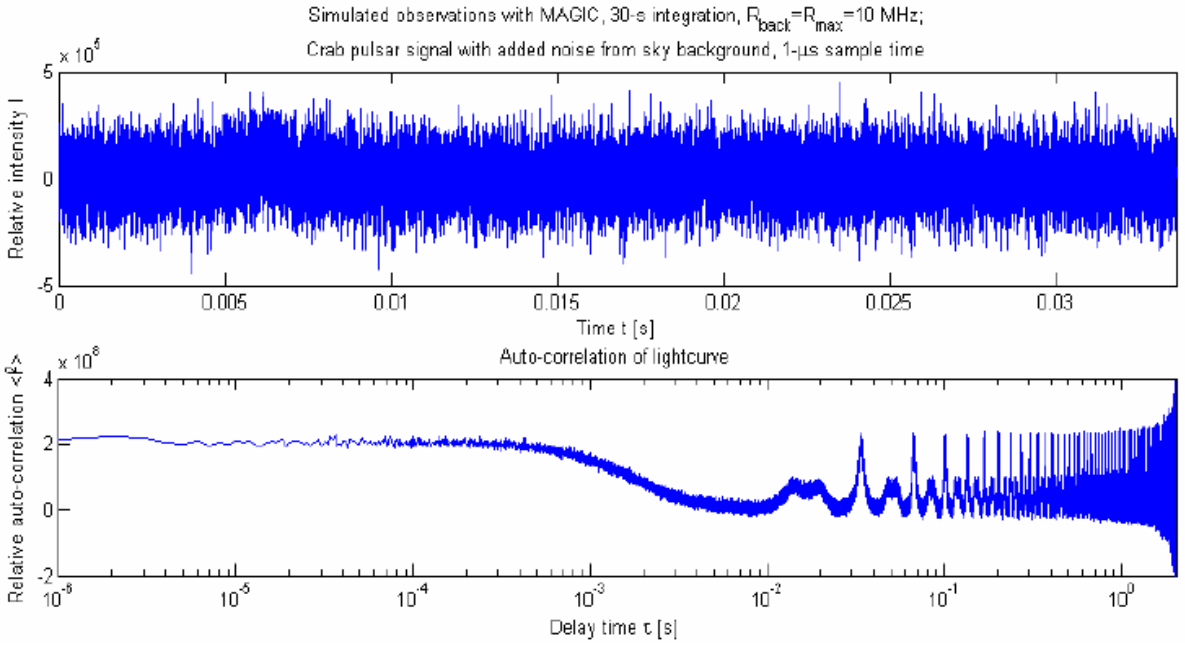

Figure 5.23: *Simulated MAGIC observations of the Crab pulsar integrated over 30 seconds. Top: The period-folded light curve shows only a subtle hint of the pulsar main peak around 5 ms at this 1 μs time resolution. Bottom: The autocorrelation extracts all timescales of systematic variability, averaging away the noisy but constant background [Dra06].*

from the source must also be rejected by a fast check of the pulse shape and intensity.

Once the single photon signal has been digitized, the most relevant information for the subsequent correlation analysis is the arrival time, which should be fixed with the maximum precision: present techniques allow time-tagging better than 100 ps [Nal07].

The project for such a correlation spectrometer is illustrated in figure 5.22: if the detector is intended only for time correlation analysis, then the output of a single QIP can be directed to a time-correlator.

The technical solutions available also include real-time signal processors with sustainable rates up to 500 MHz. The data storage on a reserved memory unit would also account for off-line analysis.

A possible solution would be the coupling with the already existing QVANTOS Mark-II correlator, built at Lund University and already tested in 2005 at the Skinakas Observatory (Crete) coupled with OPTIMA (MPI) photometer to detect the Crab pulsar.

On that occasion the limited telescope diameter (1.3 m) did not allow researchers to exploit at the best the correlator nanosecond resolution, for which a much larger telescope is required.

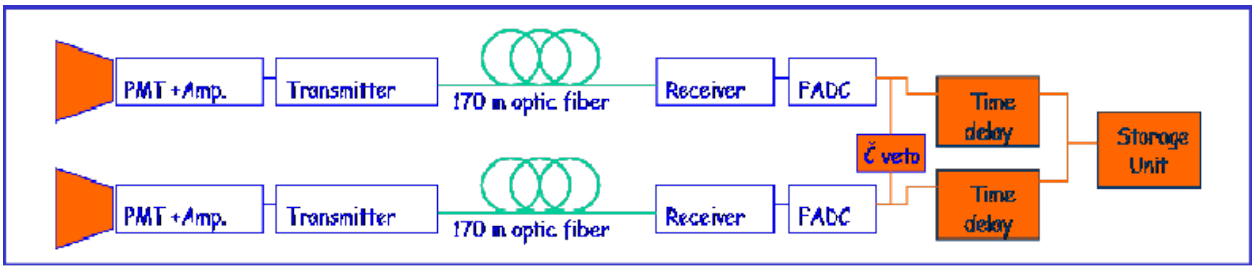

Figure 5.24: *Outline of an Intensity Interferometer project for MAGIC-II: the orange bakground indicates the new elements to be integrated.*

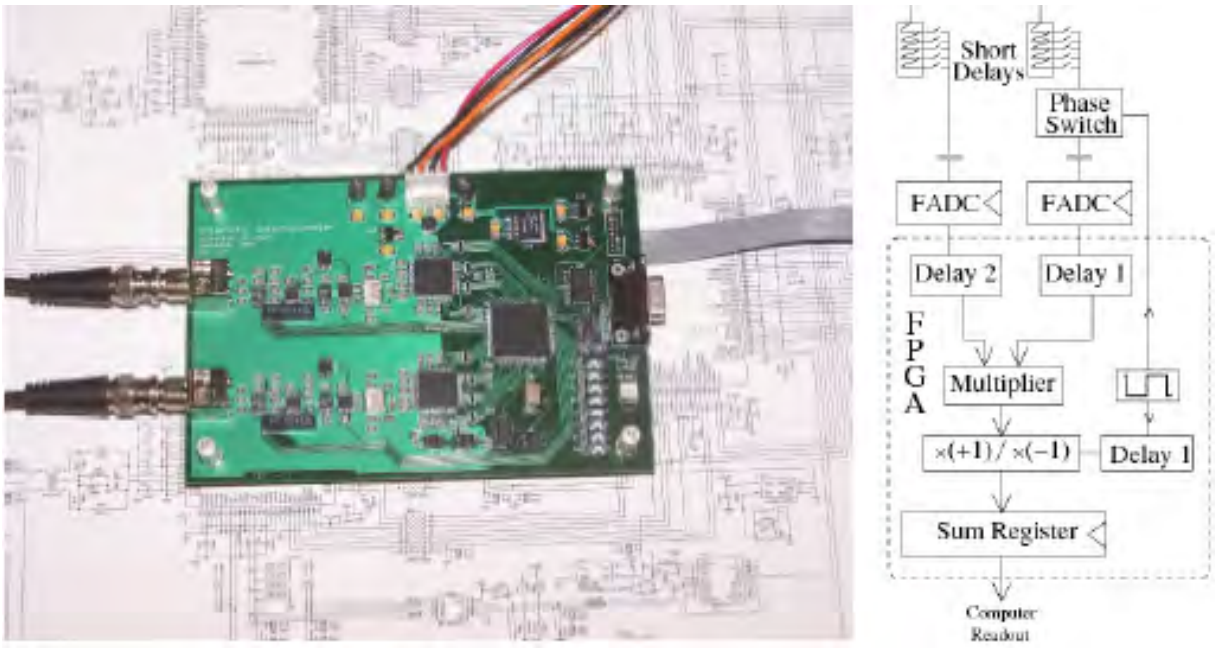

(a) (b)

Figure 5.25: *(a) A digital correlator prototype for Intensity Interferometry [Boh06] and (b) its system functional schematic.*

Under this perspective, the MAGIC-II system would easily fit the interfacing with the correlator [Dra06], resulting in a much more sensitive device, as shown by a preliminary simulation of the Crab autocorrelation (see figure 5.23): although the pulsar is many orders of magnitude weaker than the background [Ona04], the time integration over a period of seconds already reveals a sensible autocorrelation.

The achieved sensitivity would also allow the identification of unknown periodicities down to microsecond timescales with integration times of a few hours when observing analogous variable sources.

On the other hand, the realization of an Intensity Interferometer requires the use of the central pixels of both telescopes and an adequate synchronization between the two units: the Rubidium high precision atomic clock already present in the MAGIC control house fulfils this requirement.

Moreover, the Rub-GPS timing system employed by MAGIC [Luc05b] could also be used to synchronize these units with other distant interferometers, allowing much greater baselines in future.

The QIP and readout solution illustrated above, together with the insertion of tunable digital delays (see paragraph 5.4.2) to compensate for the nominal baselines, fit the requirements for space-correlation measurements.

The solution for such an istrument is sketched in figure 5.24.

The new electronic elements and the correlator can be modeled on the existing bibliography [Boh06, Boh08]: an outline is shown in figure 5.25. Short programmable delays can be used to set the relative timing of the two channels to a fraction of the digitization period. Larger time corrections can be introduced on the digitized samples.

The phase of one of the two signals is inverted with a 50% duty cycle before digitization. Digital samples are multiplied together. In order to demodulate the correlation signal, the sign of the product is inverted during phases when the phase of the analogical signal is inverted. The result is accumulated in a sum register.

As intensity interferometry requires more detailed and comparative off-line analysis, the storage of the output data in a reserved unit is strongly recommended.

5.4.4 Summary of the project

Considering present available technology and the present experiences with IACTs and other quantum optical devices, a project has been developed for a new Quantum Interferometer to be implemented on the MAGIC-II telescope.

The Intensity Interferometer is composed of two equivalent fast photocounting units (a Correlation Spectrometer corresponds to a single unit) based on the standard MAGIC-II PMT R10408 in the centre of each telescope (central pixel), plus a digital correlation system located downstream. The transmission optical line and the signal preamplification and formation electronics are the same used for all MAGIC-II camera pixels.

The two units are synchronized by a Rubidium atomic clock, while tunable time delays compensate for the path variations during the transit of the source, allowing different baselines for space correlation measurements.

The new interferometer, studied in collaboration with the Departments of Astronomy and Information Engineeerings of Padua University, can be integrated in MAGIC-II in two steps:

- the integration of a QIP in the new MAGIC-II camera central module, to test the new optics and correlation electronics measuring the time autocorrelation of suitable targets, then to hunt nanosecond pulsars or laser sources;

- the integration of a second QIP in the first MAGIC camera, to exploit the stereo system for space-correlation measurements on different stellar sources and other targets, with baselines continuously varying up to the fixed distance of 85 m between the two telescopes.

Relying on this project, the new interferometer is expected to reach a nanosecond sensitivity on the time-correlation measurements and a spatial resolution better than a milliarcsec on the sources, thus opening a new observational window on a still unexplored scale.

To end with, it is worth noting that the future integration of MAGIC-II in the CTA project would introduce new perspectives both on the number and length of the available baselines for intensity interferometry and on the higher order terms studies.

Appendix A

Communicating physics at school and to the public

Even if the importance of outreach activity for physics has been recently pointed out in Italy by specific studies [Arm06], some people in our country still consider communicating physics as a less worth activity for a scientist than direct engagement in the research.

On the contrary, an effective communication to the public is of the greatest value, as it results in funding, support and collaborations for present and future scientific developments.

A second issue presently under debate in our country is the motivation and basic formation of the secondary school students in view of their possible option for scientific faculties, specifically pursued with the national *Progetto Lauree Scientifiche* (PLS) (see e.g. [SIF08]).

Teaching can be considered as a specific form of communication, which requires furthermore the knowledge of learning mechanisms and a psychological background: an effective teaching would result not only in transmitting the disciplinary contents and techniques to the students, but also in raising their interest and motivating their study of a specific field of research.

Outreach and teaching activities have been a natural extension of my PhD studies, also in relation with to my previous experience as physics teacher in secondary schools.

A didactical project and some of the outreach materials which I developed during my training in the MAGIC collaboration are described in this appendix.

A.1 The MAGIC experiment as a guideline for a cycle of lectures on modern physics

Most people consider physics as one of the most difficult sciences to be approached and often drop the interest raised by some topics when faced to the conceptual instruments needed to its deeper understanding.

The main obstacle when approaching physics at school is often the student's fear of failing: the real challenge for the teacher is then to overcome this possibly negative feedback related to the evaluation, at the same time giving the students a real motivation to improve their knowledge.

A possible strategy for the teacher is then to reduce to the least the conceptual difficulties, dropping or oversimplifying the topics which require higher efforts to be dealt with.

A paradoxical consequence of this teaching approach is that the students, especially the gifted, lose their interest for the physics, as it appears as a plain (dull?) application of formulas to simple situations far from reality.

At the same time, a limited conceptual framework inhibits the communication of the major results and ideas typical of the physics, thus contributing to keep at distance the people from the continuous progress in the field.

If it is true that learning physics requires a formal teaching context, time and application, the basic concepts and ideas can also be communicated in less formal ways such as thematic lectures, or the guided reading or discussion of divulgative articles or books.

An alternative teaching approach is then the discussion of the main ideas, topics, and progress in some sector of the physics in contexts such as physics lectures, which do not require previous knowledge of formal instruments and leave the students free from the fear of being evaluated.

Once the students feel the importance or the beauty of the concepts on which physics is based, they are better motivated in developing their formal study: even the less engaged can at least save some general information which otherwise would have been lost.

At the same time, the direct contact with different speakers such as teachers, researchers or University professors realized in this context can vehicle direct information on the state of the art in the different research fields, allowing the students a more conscious choice in the possible prosecution of their studies.

I repeatedly experienced this possibility in the past, within the organization of physics lectures in my school [dS07a], open to every interested students: the material produced by the speakers on the main topics (Relativity, Quantum Mechanichs, Particle Physics) has been published by the school and is available in form of visual support (PowerPoint presentations).

Being involved in MAGIC collaboration, I planned some lectures on the telescope discoveries and results: as the topic is far from usual arguments developed in curricular physics studies, the argument had to be introduced by degrees.

The cycle of lectures held in 2008 at Liceo Scientifico Statale G. Galilei in Verona was focussed on the properties of the light, with the MAGIC telescope activity as a guideline.

Four lectures held by different speakers treated separately the main theoretical and experimental topics, namely:

- "Lux in the Sky with Diamonds", an introduction to the MAGIC telescope and its functioning starting from classical optics;
- "Celeritas", an overview of the strong relationship between light properties and the Theory of relativity ;
- "Vedere l'invisibile", a plain exposition of the basic principles of Quantum Mechanics and its applications in modern physics;
- "MAGIC, una finestra sull'Universo", an overview on some topics in astrophysics through the results of the MAGIC observations.

The activity involved roughly 200 students of Liceo "G. Galilei" aged from 16 to 19 year and some people from other secondary schools of Verona, with a high degree of participation: more than 120 students followed at least three out of four lectures of the cycle, being awarded with a "credito formativo" positively considered in their yearly scholar evaluation.

The consistence of the public suggested a statistical analysis of the results in terms of communication of physics concepts: a feedback test on the main topics of the lectures was then proposed at the end of the cycle to all the participants, in anonymous form to free the students from the feeling of being individually evaluated.

The test was structured in 20 items on different aspects of the four lectures (see figures A.1 and A.2), plus an open question on impressions and personal contributions of the student.

L. S. S. "GALILEO GALILEI" A. S. 2007/2008

AIUTACI A MIGLIORARE IL NOSTRO LAVORO! Ti preghiamo di compilare il presente questionario e riconsegnarlo al prof. DE SABATA al termine della conferenza o al centralino entro SABATO 16 MARZO).

Classe_____ Cognome e nome:_____

ET LUX FUIT (le conferenze di fisica al Galilei a.s 2007/2008)

I) A quale indirizzo di studi sei iscritto? □ tradizionale o linguistico □ sperimentale (PNI, tecnologico, sc. Brocca)

II) Quale classe frequenti attualmente? □ biennio □ terza □ quarta □ quinta □ università

III) Quali conferenze hai potuto seguire?
□ Lux in the sky with Diamonds... (ottica classica e telescopio MAGIC) □ Celeritas (luce e relatività)
□ Vedere l'invisibile (fisica quantistica e moderna) □ MAGIC, una finestra sull'Universo (astrofisica)

IV) (soprattutto per gli studenti di QUINTA) Ritieni che quest'attività sia utile nel migliorare la tua preparazione scientifica in vista dell'esame di Stato e della scelta universitaria?
□ SÍ, molto □ SÍ, in parte □ NO, poco □ NO, per niente □ non so

****

1. Quale tra le seguenti teorie descrive TUTTE le caratteristiche della luce?
(A) l'ottica geometrica (B) l'ottica ondulatoria (C) la relatività (D) nessuna delle tre

2. Cos'è l'effetto Čerenkov?
(A) l'emissione di luce da stelle lontane (B) l'emissione di luce dall'atmosfera (C) l'emissione di luce da particelle cariche più veloci di c/n (velocità della luce nel mezzo attraversato) (D) nessuna delle risposte precedenti è corretta

3. A cosa serve il telescopio MAGIC?
(A) a studiare i raggi cosmici (B) a studiare le sorgenti cosmiche di raggi gamma
(C) a studiare la nostra galassia (D) nessuna delle tre risposte precedenti è corretta

4. Quali caratteristiche ha il telescopio MAGIC rispetto agli altri telescopi a Terra?
(A) la più grande parabola ottica (B) la maggior velocità di puntamento
(C) una struttura particolarmente leggera (D) tutte e tre le risposte precedenti sono corrette

5. Quali sono, tra i seguenti, i segnali elettromagnetici di maggior energia?
(A) i raggi ultravioletti (B) i raggi gamma (C) i raggi X (D) la radiazione Čerenkov

6. La velocità della luce nel vuoto
(A) dipende dalla velocità della sorgente che la emette (B) dipende dalla velocità dell'osservatore che la riceve
(C) dipende sia dalla velocità della sorgente che dell'osservatore (D) è invariante per tutti gli osservatori inerziali

7. Perché la fisica classica non è in grado di descrivere correttamente il comportamento della luce?
(A) perché non ne spiega l'aspetto ondulatorio (B) perché non interpreta correttamente il processo di rifrazione
(C) perché non è possibile applicare alla luce le trasformazioni di Galilei
(D) perché non ammette che un'onda si propaghi nel vuoto

8. La contrazione delle lunghezze è simmetrica per due osservatori inerziali?
(A) sí, perché la velocità della luce è costante (B) sí, perché non esiste un sistema di riferimento privilegiato
(C) no, perché il moto dei due osservatori avviene in verso opposto
(D) no, perché si contraggono anche le unità di misura.

9. Alla luce della teoria della relatività, la meccanica classica
(A) ne costituisce il limite per piccole masse (B) ne costituisce il limite per grandi masse
(C) ne costituisce il limite per piccole velocità (D) ne costituisce il limite per grandi velocità

il questionario prosegue sul retro

Figure A.1: *The feedback test proposed to the participants to the lectures (side A).*

10. La luce risente dell'attrazione gravitazionale?
(A) Sí, perché è composta da particelle materiali (B) No, perché è composta da particelle di massa nulla
(C) Sí, perché la presenza di una massa modifica la geometria dello spazio (D) No, perché è un'onda

11. Il comportamento ondulatorio della luce è dimostrato sperimentalmente da:
(A) Il fenomeno della riflessione (B) Il fenomeno della rifrazione
(C) I fenomeni della diffrazione e dell'interferenza (D) Nessuna delle tre risposte precedenti è corretta.

12. Quale di queste applicazioni tecnologiche sfrutta l'effetto fotoelettrico?
(A) i pannelli solari votovoltaici (B) le aperture di sicurezza per cancelli e ascensori
(C) il rivelatore (camera) del telescopio MAGIC (D) tutte e tre le risposte precedenti sono corrette

13. Se vogliamo "risolvere" (osservare come separati) due oggetti puntiformi molto vicini utilizzando un'onda di lunghezza λ e un foro circolare:
(A) maggiore è λ, migliore è la possibilità di separare le immagini
(B) minore è λ, migliore è la possibilità di separare le immagini
(C) la possibilità di separare le immagini non dipende da λ
(D) non è possibile rispondere senza conoscere le caratteristiche dell'apparato di misura

14. Per osservare "oggetti molto piccoli" si utilizzano come "sonde"
(A) elettroni a BASSA energia perché corrispondono a onde con PICCOLA lunghezza
(B) elettroni a BASSA energia perché corrispondono a onde con GRANDE lunghezza
(C) elettroni a GRANDE energia perché corrispondono a onde con PICCOLA lunghezza
(D) elettroni a GRANDE energia perché corrispondono a onde con GRANDE lunghezza

15. La struttura interna di un protone corrisponde a:
(A) un quark e un antiquark (B) quark ed elettroni (C) tre quark (due uguali fra loro e uno diverso)
(D) Il protone non ha struttura interna, non ci sono esperimenti che la evidenziano

16. Quali tipi di radiazione sono DIRETTAMENTE rivelabili da Terra?
(A) i raggi gamma (B) i raggi X (C) le onde radio e luminose (D) tutte e tre le risposte precedenti sono corrette

17. Quali tra i seguenti fenomeni di origine astrofisica producono raggi gamma?
(A) l'emissione termica stellare (B) le reazioni chimiche nelle nebulose (C) il collasso gravitazionale
(D) solo i fenomeni più energetici (per esempio, esplosioni di Supernovae)

18. Come vengono prodotte le coppie di elettroni e positroni negli sciami atmosferici?
(A) dalla ionizzazione delle molecole d'aria (B) dal decadimento dei nuclei radioattivi
(C) dalla 'materializzazione' dei fotoni energetici ($E=mc^2$) (D) dalla radiazione Čerenkov

19. Che tipo di luce raccoglie il telescopio MAGIC?
(A) i raggi gamma prodotti dall'annichilazione di coppie $e^+ e^-$ negli sciami cosmici
(B) la radiazione luminosa prodotta dalle particelle cariche che attraversano l'alta atmosfera
(C) i raggi gamma prodotti dalle sorgenti astrofisiche (D) nessuna delle risposte precedenti è corretta

20. Cosa sono gli AGN (Active Galactic Nuclei)?
(A) oggetti stellari nel nucleo della nostra galassia (B) nuclei di galassie lontane che emettono raggi X e gamma
(C) nuclei atomici che emettono raggi gamma (D) nessuna delle tre risposte precedenti è corretta

Eventuali osservazioni e contributi personali:

Figure A.2: *The feedback test proposed to the participants to the lectures (side B).*

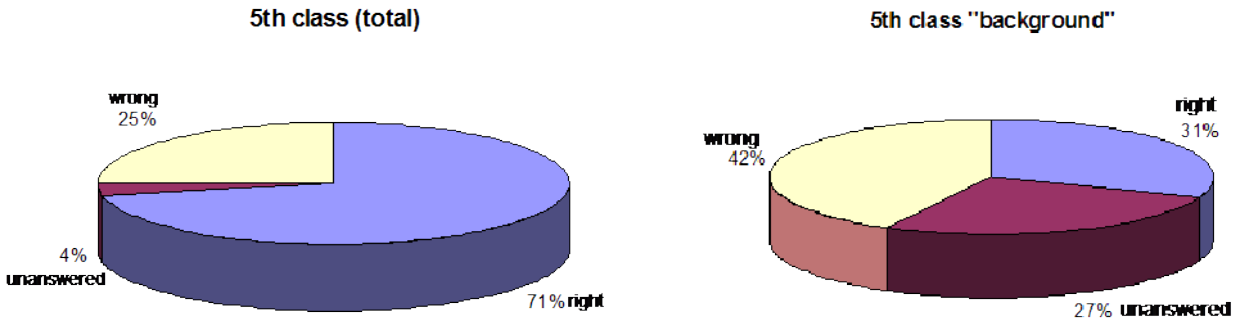

Figure A.3: *The percentage of success in the feedback test.*

The students could indicate a possibly missed lecture: in this situation the corresponding items were not considered as valid answers and the percentage of success in the test was evaluated on the remaining 15 items. Only the students which participated to at least three or four lectures were considered in the statistical analysis of the answers.

As the students coming from ordinary and experimental courses at the same year of study show little difference in the results (within 2–3 % of the total), with a wider spread between intermediate and last year students, the statistical sample was then subdivided by year of study.

The resulting samples included 77 set of questions from students of the third year, 24 set of questions from students of the fourth year and 24 set of questions from students of last year of secondary school, for a total of 125 set of questions.

The third and fourth year students answered correctly to $62 \pm 2\%$ of the questions, while the students of last year, coming almost exclusively from experimental courses, reached a higher percentage of success, roughly 70 %.

The best results (19 and 20 correct answers out of 20) were obtained by three students of third year and two of the last year, confirming the equal opportunity to profit of such lectures independently from the age and the background of formal study of physics.

As the topics treated in the lectures are normally excluded from the curricular program, except for the final year of experimental courses like the Liceo Tecnologico “Brocca” and the Liceo Scientifico PNI (Piano Nazionale per l’Informatica), there was little doubt on the independence of the information needed to answer properly to the set of questions from the curricular studies at that time of the year.

Nevertheless, a further check of this possibility was realized with the subministration of the same test in three classes of a different Liceo tecnologico “Brocca” in Verona, in order to get an estimate of the student’s background knowledge in the field.

I chose an experimental course as reference sample considering the fact that most of the participants to the lectures (88 out of 125) studied physics in an experimental course at Liceo “G. Galilei”.

Three subsamples were composed of 23 set of questions from students of the third year, 21 set from students of the fourth year and 17 set from students of the last year of studies, for a total of 61 set of questions.

As expected, the percentage of success for the students of the reference sample in the test was much lower than that of the participants to the lectures: the values obtained by intermediate course students ranged within 22% and 28%, compatible with a pure statistical noise.

The students of the final year in the reference sample gave on average the 31% of correct answers.

Figure A.3 shows the high percentage of right answers in the test of the 14 last year students which participated to the four lectures compared to the reference sample.

The high participation of students to the physics lectures at the liceo "G. Galilei", together with the test results which showed the high degree of understanding and learning of the public, states the validity of this communicative strategy and encourages the prosecution of this kind of activity in our school.

A.2 MAGIC outreach: poster presentations to the public

The Innovaction exhibition held in Udine from year to year has been the occasion to propose and illustrate the MAGIC esperiment to the public.

I produced two posters to introduce the telescope and the γ-ray astrophysical observations to different public targets: the first one (see figure A.4) was exposed for the first time in 2007 in the MAGIC stand as explanation support for adults, while the second (see figure A.5) is directed to young people and schools.

The different public targets led me to different choices in the image composition: a more traditional plot is used for adults, following the usual occidentallecture order from left to right and from top to bottom.

Four topics are grouped as small chapters one below the other, to introduce the reader to γ-ray astronomy from the very basic information (nature of γ-rays and the IACT detection technique) to the MAGIC telescope, to end with its scientific results.

The separation among these segments allows different entry levels in the illustration, from the very beginner to the more experienced reader, who can skip the first topics or even jump directly to the final information about the scientific result of the collaboration.

On the other hand, the poster addressed to young students is based on a direct structure with a central "star" surrounded by individual panels, which also suggest the activity of the MAGIC telescope as a new opening on the Universe, or a blowing up extension of the observations in the field.

The single panels around the central "star" directly focus on different features of the telescope, while the larger panel on the right allows a plain description of the instrument.

A "deep sky" background image is used in this poster to evocate the field indagated by MAGIC: the choice of such a dark background is balanced by the bright images in the panels and the yellow used for the writings.

Both posters have been repeatedly updated and exposed in different occasions, like the "*Comunicare Fisica 2007*" workshop held in Trieste [dS07b] and the physics lectures held in Verona in 2008: every time they have met the interest and appreciation of the public.

Among the other outreach activities for the MAGIC-Udine group, I also prepared the italian version of the MAGIC-II inauguration flyer and the italian text of the movie realized for that occasion.

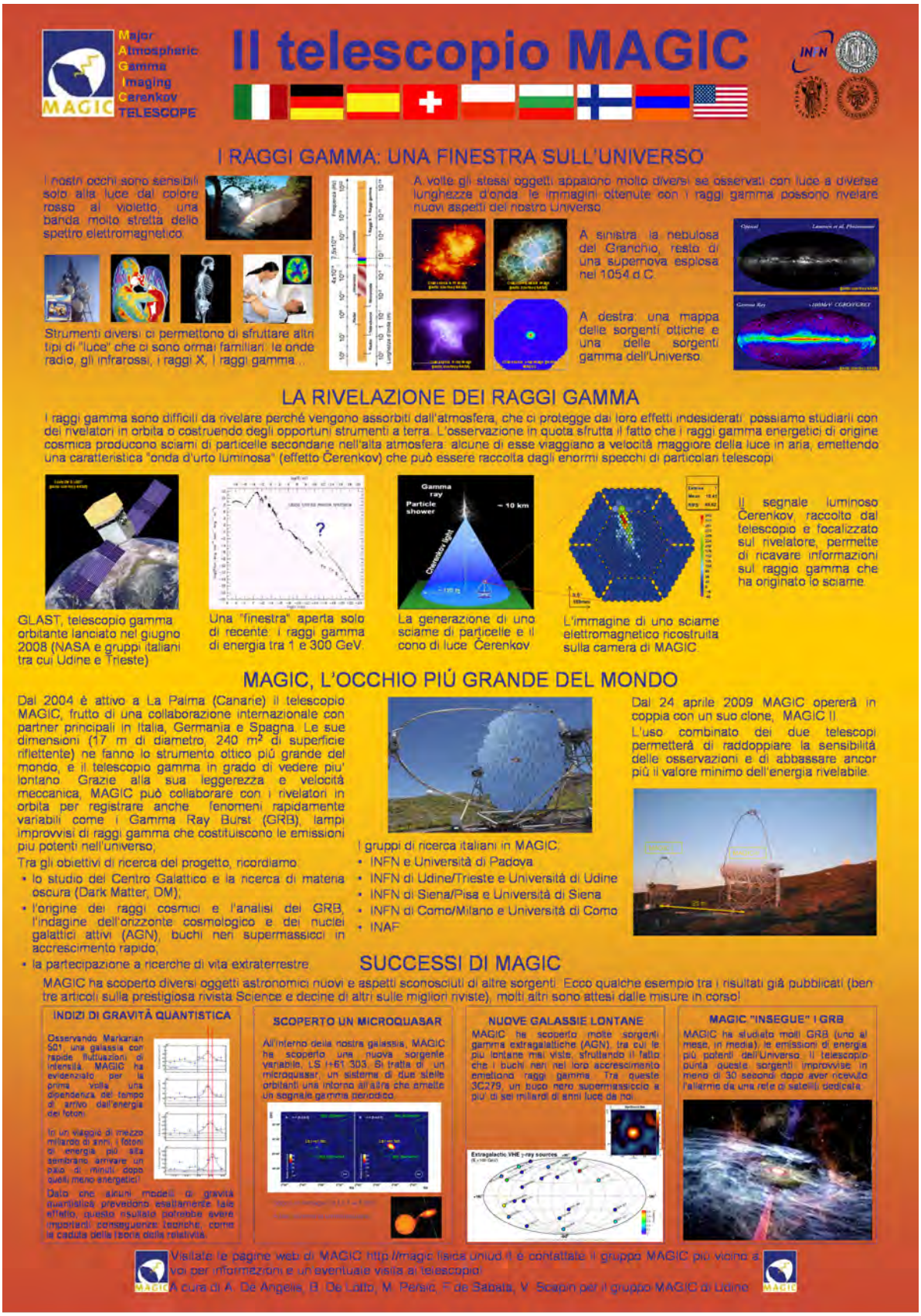

Figure A.4: *The MAGIC poster presentation elaborated for Innovaction2007 exposition.*

Figure A.5: *The MAGIC poster presentation directed to the students.*

Summary

My PhD work within the MAGIC collaboration was directed on two main topics, both related to the stereoscopic telescope MAGIC-II, namely:

- a full Monte Carlo simulation of the new stereoscopic system, in order to obtain an accurate evaluation of its expected performance;

- the possible implementation of a modified central pixel on both telescopes, in order to realize a quantum interferometer with the individual photon detection and time-tagging technique dedicated to time-correlation and intensity interferometry studies.

In more detail, I produced for the MAGIC Udine group a wide database of simulated events using the CNAF facility, to be used in the future data analysis of MAGIC-II. Before the commissioning of the second telescope, I used the simulated events to test the potential of MAGIC-II on the basis of the standard MARS analysis software integrated with algorithms specific for the stereoscopic system.

The stereoscopic system is expected to improve significantly the performance with respect to the single MAGIC telescope: in particular, it will allow a more precise reconstruction of the showers and a significant reduction of hadronic background below 100 GeV.

This will make possible an improved angular and energy resolution as well as a reduction of the analysis threshold down to 20 – 30 GeV. Altogether it will give MAGIC-II a sensitivity increased of a rough factor 3 with respect to the single MAGIC telescope.

With regard to the second topic, considering the presently available technology and the most recent experiences with IACTs and other quantum optical devices, I developed a project for a new Quantum Interferometer to be implemented on MAGIC-II.

In more detail, the Intensity Interferometer is composed of two equivalent fast photocounting units (a single unit can be used as Correlation Spectrometer) based on the standard MAGIC-II PMT R10408 in the central pixel of each telescope, plus a digital correlation system located downstream. The optical transmission line and the signal preamplification and formation electronics are the same used for all MAGIC-II camera pixels.

The two units are synchronized by a Rubidium atomic clock, while tunable time delays compensate for the path variations during the transit of the source, allowing different baselines for space correlation measurements.

The new interferometer is expected to reach a nanosecond sensitivity on the time-correlation measurements and a spatial resolution better than a milliarcsec on the sources, thus opening a new observational window on a still unexplored scale.

Moreover, during my PhD work I also realized a cycle of lectures on modern physics in a secondary school with the MAGIC telescope as leading theme, and produced some posters and other outreach material for the collaboration.

Acknowledgements

At the end of this thesis I want to thank my supervisors, prof. Alessandro de Angelis, who gave me the opportunity for "a second turn on the Carousel of Physics", and prof. Cesare Barbieri, for their attention and support.

This work would have never been achieved without the contributions of many really MAGIC people I met here and there within the collaboration: among all the others, I am particularly grateful for their effective teaching to Abelardo, Alessandro, Emiliano, Karsten and Pratik.

I also greatly appreciated the comments and contributions to my work of Claudio, Dainis, Daniela, Florian, Juan, Mosè, Paola, Pierre, Ray and Toni.

I enjoyed the friendly atmosphere of the MAGIC groups of Udine and Padova, in particular thanks to Barbara, Elisa, Franz, Massimo, Michela, Michele, Nijil, Oriana, Saverio, Valeria, Villi.

I want to address here a special thank to Giampiero, for his constant presence in the relevant moments of my life, included the PhD experience...

I'm indebted with Donata, Luca, Martina, Tiziana and, above all, with Marcella, for their hidden and patient support during the last three years of study.

Bibliography

[Abd08] Abdo, A. A. et al. (The FERMI LAT collab.). The Fermi Gamma Ray Space Telescope discovers the Pulsar in the Young Galactic Supernova-Remnant CTA 1. *Science*, **322**:1218, 2008. (arXiv:astro–ph/0810.3562).

[Abr07] Abraham, J. et al. (The P. Auger collab.). Correlation of the Highest-Energy Cosmic Rays with Nearby Extragalactic Objects. *Science*, **318**:938, 2007.

[Aha03] Aharonian, F. A. et al. (The HEGRA collab.). Is the giant radio galaxy M87 a TeV gamma-ray emitter? *Astron. Astrophys.*, **403**:L1, L5, 2003.

[Aha04] Aharonian, F. A. *Very high energy cosmic gamma radiation.* World Scientific, Singapore, 2004.

[Aha06a] Aharonian, F. A. et al. A detailed spectral and morphological study of the gamma–ray supernova remnant RX J1713.7-3946 with H.E.S.S. *Astron. Astrophys.*, **449**:223, 2006. (arXiv:astro–ph/0511678).

[Aha06b] Aharonian, F. A. et al. A low level of extragalactic background light as revealed by gamma-rays from blazars. *Nature*, **440**:1018, 2006. (arXiv:astro–ph/0508073).

[Aha08] Aharonian, F. A. High energy astrophysics with ground-based gamma ray detectors. *Rep. Prog. Phys., to appear*, 2008.

[All70] Allen, L. R. and Frater, R. H. Wideband multiplier correlator. *Proc. Instn. elect. Engrs*, **117**:1603, 1970.

[Ame98] Amelino-Camelia, G. et al. Potential Sensitivity of Gamma-Ray Burster Observations to Wave Dispersion in Vacuo. *Nature*, **393**:763, 1998. (arXiv:astro–ph/9712103).

[Ame06] Amenomori, A. et al. (The P. Auger collab.). Are protons still dominant at the knee of the cosmic-ray energy spectrum? *Phys. Lett. B*, **632**:58, 2006.

[AND] ANDOVER website. *http://www.andovercorp.com.*

[Ang07] De Angelis, A. et al. Evidence for a new light spin-zero boson from cosmological gamma-ray propagation? *Phys. Rev. D*, **76**:121301, 2007.

[Ang08a] De Angelis, A. et al. Axion-Like Particles, Cosmic Magnetic Fields and Gamma-Ray Astrophysics. *Phys. Lett. B*, **659**:847, 2008. (arXiv:astro–ph/0707.2695).

[Ang08b] De Angelis, A. et al. Constraints on Large–Scale Magnetic Fields from the Auger Results. *Mod. Phys. Lett. A*, **23**:315, 2008. (arXiv:astro–ph/0711.3346).

[Ang08c] De Angelis, A. et al. Very–high–energy gamma astrophysics. *Nuovo Cimento*, **31**:187, 2008.

[Are65] Arecchi, F. T. et al. Measurement of the Statistical distributions of the Gaussian and Laser Sources. *Phys. Rev. Lett.*, **15**:912, 1965.

[ARG] ARGO website. *http://argo.na.infn.it*.

[Arm06] Armeni, M., editor. *Communicating Physics*. Zadigroma, Roma, 2006.

[Bar98] Barrio, J. A. et al. The MAGIC Telescope – Design Study for the Construction of a 17 m Cherenkov Telescope for Gamma Astronomy above 10 GeV. Technical Report MPI-PhE 98-05, 1998.

[Bar04] Baring, M. G. High-Energy Emission from Pulsars: The Polar Cap Scenario. *Adv. Space Res.*, **33**:552, 2004.

[Bar07] Barbieri, C. et al. The optomechanical design of AquEYE, an instrument for astrophysics on its shortest timescales at the Asiago Observatory. *Mem. S. A. It. Suppl.*, **11**:190, 2007.

[Bar08] Barbieri, C. et al. AquEYE, a single photon counting photometer for astronomy. *J. Mod. Opt., to appear*, 2008.

[Bas01] Bastieri, D. et al. A two-level pattern trigger for the MAGIC telescope. *Nucl. Instrum. Meth. A*, **441**:521, 2001.

[Bas07] Bastieri, D. et al. The reflecting surface of the MAGIC-II telescope. In *Proc.* 30^{th} *ICRC Mérida*, volume **3**, page 1547, 2007. (arXiv:astro–ph/0709.1372).

[Bel78] Bell, A. R. The acceleration of cosmic rays in shock fronts. I and II. *Mon. Not. Roy. Astron. Soc.*, **182**:187, *Ibid.*, **182**:443, 1978.

[Bil06] Biland, A. et al. Monte Carlo Production Strategy for MAGIC-II two-telescope system. Technical Report MAGIC TDAS 12-06, 2006.

[Bil07] Biland, A., et al. The Active Mirror Control of the MAGIC Telescope. In *Proc.* 30^{th} *ICRC Mérida*, volume **3**, page 1353, 2007. (arXiv:astro–ph/0709.1574).

[Bla78] Blandford, R. D. and Ostriker, J. P. Particle Acceleration by Astrophysical Shocks. *Astrophys. J. Lett.*, **221**:L29, L32, 1978.

[Bla03] Blanch, O. et al. Testing the effective scale of Quantum Gravity with the next generation of Gamma Ray Telescopes. *Astropart. Phys*, **19**:245, 2003. (arXiv:astro–ph/0107334).

[Bla04] Blanch, O. and Moralejo, A. How To Use the camera simulation program 0.7. Technical Report MAGIC TDAS 04-07, 2004.

[Boc04] Bock, R. et al. Methods for multidimensional event classification: a case study using images from a Cherenkov gamma-ray telescope . *Nucl. Instrum. Meth. A*, **516**:511, 2004.

[Boh13] Bohr, N. On the constitution of molecules and atoms, part I, II and III. *Philos. Mag.*, **26**:1, 476, 857, 1913.

[Boh06] Le Bohec, S. and Holder, J. Optical Intensity Interferometry with Atmospheric Cherenkov Telescope Arrays. *Astrophys. J.*, **649**:399, 2006. (arXiv:astro–ph/0608305).

[Boh08] Le Bohec, S. et al. Stellar Intensity Interferometry with Air Cherenkov Telescope Arrays. In O. Ryan and A. Shearer, editors, *The Universe at Sub-Second Timescales, Proc. AIP conference, to appear*, 2008. (arXiv:astro–ph/0710.0188).

[Bre01] Breiman, L. Random forests. *Machine Learning*, **45**:5, 2001.

[Bre06] Bretz, T. *Observations of the Active Galactic Nucleus 1ES 1218+304 with the MAGIC-telescope*. PhD thesis, Universität Würzburg, 2006.

[Bre08] Bretz, T. et al. The Drive System of the Major Atmospheric Gamma-ray Cherenkov Imaging Telescope. *submitted*, 2008. preprint MPP-2008-101.

[CNA] CNAF website. *http://www.cnaf.infn.it*.

[Coc59] Cocconi, G. In *Proc.* 6^{th} *ICRC Moscow*, volume **2**, page 309, 1959.

[Cop97] Coppi, P. and Aharonian, F. A. Constraints on the VHE Emissivity of the Universe from the Diffuse GeV Gamma-Ray Background. *Astrophys. J.*, **487**:L9, 1997. (arXiv:astro–ph/9610176).

[COR] CORSIKA website. *http://www-ik3.fzk.de/~heck/corsika/physics description*.

[Cro97] Cronin, J. et al. *Sci. Amer.*, **276**:44, 1997.

[CTA] CTA website. *http://www.mpi-hd.mpg.de/hfm/CTA*.

[Dau97] Daum, A. et al. First results on the performance of the HEGRA IACT array. *Astropart. Phys.*, **8**:1, 1997.

[Dir27] Dirac, P. A. M. The quantum theory of the emission and absorption of radiation. *Proc. R. Soc. A*, **114**:243, 710, 1927.

[Dir30] Dirac, P. A. M. *The principles of Quantum Mechanics*. Oxford Univ. Press, Oxford, 1930. (reprint 1999).

[dJ96] de Jager, O. C. et al. Gamma-Ray Observations of the Crab Nebula: A Study of the Synchro-Compton Spectrum. *Astrophys. J.*, **457**:253, 1996.

[Doe01] Doering, M. et al. Measurement of the Cherenkov light spectrum and of the polarization with the HEGRA-IACT-system. In *Proc.* 27^{th} *ICRC*, 2001. (arXiv:astro–ph/0107149).

[Dom05] Domingo-Santamaria, E. et al. The DISP analysis method for point-like or extended γ source searches/studies with the MAGIC telescope. In *Proc.* 29^{th} *ICRC Pune*, volume **5**, page 363, 2005.

[Dor08] Doro, M. et al. The reflective surface of the MAGIC telescope. *Nucl. Instrum. Meth. A, to appear*, 2008.

[Dra05] Dravins, D. et al. QuantEYE. Quantum Optics Instrumentation for Astronomy. Technical Report OWL-CSR-ESO-00000-0162, ESO, 2005.

[Dra06] Dravins, D. Proposal for optical high speed astronomy with MAGIC. *MAGIC int. comm.*, 2006.

[Dra08a] Dravins, D. Photonic astronomy and quantum optics. In D. Phelan et al., editor, *High time resolution astrophysics*, page 95. Springer, 2008.

[Dra08b] Dravins, D. and Germanà, C. Photon correlation spectroscopy for observing natural lasers. In O. Ryan and A. Shearer, editors, *The Universe at Sub-Second Timescales, Proc. AIP conference, to appear*, 2008.

[Dra08c] Dravins, D. and Le Bohec, S. Towards a diffraction-limited square-kilometer optical telescope: Digital revival of intensity interferometry. In T. Andersen, editor, *ELTs - Which Wavelengths? Proc. SPIE conference, to appear*, 2008.

[dS07a] de Sabata, F. L'occhio del fisico. In Longo, F. et al., editor, *Proc. of Comunicare Fisica 07, Trieste, to appear*, 2007.

[dS07b] de Sabata, F. MAGIC, una finestra sull'Universo. In Longo, F. et al., editor, *Proc. of Comunicare Fisica 07, Trieste, to appear*, 2007.

[Dys20] Dyson, F. W. et al. A Determination of the Deflection of Light by the Sun's Gravitational Field, from Observations Made at the Total Eclipse of May 29, 1919. *Phil. Trans. Roy. Soc.*, **A 220**:291, 1920.

[Ein05] Einstein, A. Über einen die Erzeugung und Verwandlung des Lichtes betreffenden heuristischen Gesichtspunkt. *Ann. d. Phys.*, **17**:132, 1905.

[Eli95] Elitzur, M. Masers in the sky. *Sci. Am.*, **272**:52, 1995.

[Fan61] U. Fano. Quantum theory of interference effects in the mixing of light from phase independent sources. *Am. J. Phys.*, **29**:539, 1961.

[Fer49] Fermi, E. On the Origin of the Cosmic Radiation. *Phys. Rev.*, **75**:1169, 1949.

[Fer05] Ferrari, A. et al. FLUKA: a multi-particle transport code. Technical Report CERN 2005-010, 2005.

[Fey50] Feynman, R. P. Mathematical formulation of the quantum theory of electromagnetic interaction. *Phys. Rev.*, **80**:1440, 1950.

[Fey61] Feynman, R. P. *Quantum Electrodynamics*. W. A. Benjamin, New York, 1961.

[FGS] FGST (The Fermi Gamma-ray Space Telescope) website. *http://fermi.gsfc.nasa.gov*.

[Fom94] Fomin, V. P. New methods of atmospheric Cherenkov imaging for gamma–ray astronomy. I. The false source method. *Astrop. Phys.*, **2**:137, 1994.

[Gal10] Galilei, G. *Sidereus Nuncius*. Venezia, 1610.

[Gia62] Giacconi, R. et al. Evidence for x Rays From Sources Outside the Solar System. *Phys. Rev. Lett.*, **9**:439, 1962.

[Gla63] Glauber, R. J. The quantum theory of optical coherence, part I and II. *Phys. Rev.*, **130**(6):2529, *Ibid.* **131**:2766, 1963.

[Gla06] Glauber, R. J. One hundred years of light quanta, Nobel lecture. *Rev. Mod. Phys*, **78**(6):1267, 2006.

[Goe03] Goebel, F. et al. The Data Acquisition of the MAGIC Telescope. In *Proc.* 28^{th} *ICRC Tsukuba*, volume **5**, page 2939, 2003.

[Goe05] Goebel, F. et al. Absolute energy scale calibration of the MAGIC telescope using muon images. In *Proc.* 29^{th} *ICRC Pune*, volume **5**, page 179, 2005.

[Goe07a] Goebel, F. Status of the second phase of the MAGIC telescope. In *Proc.* 30^{th} *ICRC Mérida*, volume **3**, page 1485, 2007. (arXiv:astro–ph/0709.2605).

[Goe07b] Goebel, F. et al. Upgrade of the MAGIC telescope with a Multiplexed Fiber-Optic 2 Gsamples/s FADC Data Aquisition System. In *Proc.* 30^{th} *ICRC Mérida*, volume **3**, page 1481, 2007. (arXiv:astro–ph/0709.2363).

[Gre66] Greisen, K. End to the Cosmic-Ray Spectrum? . *Phys. Rev. Lett.*, **16**:748, 1966.

[HAM] HAMAMATSU website. *http://jp.hamamatsu.com*.

[Han54] Hanbury Brown, R. and Twiss, R. Q. A new type of interferometer for use in radio-astronomy. *Phil. Mag.*, **45**:663, 1954.

[Han56] Hanbury Brown, R. and Twiss, R. Q. Correlation between photons in two coherent beams of light. *Nature*, **177**:27, *Ibid.*, **178**:1046, 1956.

[Han57] Hanbury Brown, R. and Twiss, R. Q. Interferometry of the intensity fluctuation in light, part I and II. *Proc. R. Soc. A*, **242**:300, *Ibid.*, **243**:291, 1957.

[Han58] Hanbury Brown, R. and Twiss, R. Q. Interferometry of the intensity fluctuation in light, part III and IV. *Proc. R. Soc. A*, **243**:199, *Ibid.*, **248**:222, 1958.

[Han69] Hanbury Brown, R. et al. The effect of Čerenkov light pulsess on a stellar intensity interferometer. *Mon. Not. R. astr. Soc.*, **146**:399, 1969.

[Han74a] Hanbury Brown, R. *The Intensity Interferometry*. Taylor & Francis, London, 1974.

[Han74b] Hanbury Brown, R. et al. The angular diameter of 32 stars. *Mon. Not. R. astr. Soc.*, **167**:121, 1974.

[Han03] Hankins, T. H. et al. Nanoseconds radio bursts from strong plasma turbulence in the Crab pulsar. *Nature*, **422**:141, 2003.

[Har92] Hartman, R. C. et al. Detection of high-energy gamma radiation from quasar 3C 279 by the EGRET telescope on the Compton Gamma Ray Observatory. *Astrophys. J. Lett.*, **385**:L1, L4, 1992.

[Har01] Hartman, R. C. et al. Multi-Epoch Multiwavelength Spectra and Models for Blazar 3C 279. *Astrophys. J.*, **558**:583, 2001. (arxiv:astro–ph/0102127).

[Hay08] Hayashida, M. *Observation of Very-High-Energy Gamma-Rays from Blazars with the MAGIC Telescope*. PhD thesis, Technische Universität München, 2008.

[Hec98] Heck, D. et al. Extensive Air Shower Simulation with CORSIKA: A User's Guide. Technical Report FZKA-6019, 1998.

[Hei60] Heitler, W. *The quantum theory of radiation.* Oxford University Press, Oxford, 1960.

[Hen99] Henny, M. et al. The Fermionic Hanbury Brown and Twiss Experiment. *Science*, **284**:296, 1999.

[HES] HESS website. *http://www.mpi-hd.mpg.de/hfm/HESS.*

[Hil85] Hillas, A. M. et al. Cherenkov Images of EAS produced by primary gamma rays and by nuclei. In *Proc.* 19^{th} *ICRC, La Jolla*, volume **3**, 1985.

[Hin04] Hinton, J. A. et al. The status of the H.E.S.S. project. *New Astron. Rev.*, **48**, 2004.

[Hin07] Hinton, J. A. γ-Ray Astronomy. Lecture held at 30^{th} ICRC Mérida, 2007.

[HIP] HIPPARCOS catalogue. *http://archive.ast.cam.ac.uk/hipp/hipparcos.html.*

[Hof99a] Hoffman, C. M. et al. Gamma-ray astronomy at high energies. *Rev. Mod. Phys.*, **71**, 1999.

[Hof99b] Hoffman,C. M. et al. Comparison of techniques to reconstruct VHE gamma-ray showers from multiple stereoscopic Chernkov images. *Astropart. Phys.*, **12**, 1999.

[Hsu07] Hsu, C. C. et al. The Camera of the MAGIC-II Telescope. In *Proc.* 30^{th} *ICRC Mérida*, volume **3**, page 1511, 2007. (arXiv:astro–ph/0709.2474).

[Hub29] Hubble, E. A relation between distance and radial velocity among extra-galactic Nebulae. *Proc. Nat. Ac. Sci.*, **15**, 1929.

[Hur94] Hurley, K. et al. Detection of a γ-ray burst of very long duration and very high energy. *Nature*, **372**, 1994.

[Joh02] Johansson, S. and Letokhov, V. S. Laser Action in a Gas Condensation in the Vicinity of a Hot Star. *JETP Lett.*, **75**:495, 2002.

[Joh04] Johansson, S. and Letokhov, V. S. Astrophysical lasers operating in optical Fe II lines in stellar ejecta of Eta Carinae. *Astron. Astrophys.*, **428**:497, 2004.

[Joh05] Johansson, S. and Letokhov, V. S. Possibility of measuring the width of narrow Fe II astrophysical laser lines in the vicinity of Eta Carinae by means of Brown-Twiss-Townes Heterodyne Correlation Interferometry. *New Astron.*, **10**:361, 2005.

[Joh07] Johansson, S. and Letokhov, V. S. Astrophysical lasers and nonlinear optical effects in space. *New Astron. Rev.*, **51**:443, 2007.

[Kal97] Kalmykov, N. N. et al. Quark-gluon string model and EAS simulation problems at ultra-high energies. *Nucl. Phys. Proc. Suppl.*, 52 B:17, 1997.

[Kem99] Kembhavi, A. K. and Narlikar, J. A. *Quasars and Active Galactic Nuclei.* Cambridge University Press, Cambridge, 1999.

[Kim77] Kimble, H. et al. Photon Antibunching in Resonance Fluorescence. *Phys. Rev. Lett.*, **39**:691, 1977.

[Kne04] Kneiske, T. M. et al. Implications of cosmological gamma-ray absorption ii. Modification of gamma-ray spectra. *Astron. Astrophys.*, **413**:807, 2004.

[Kon97] Konopelko, A. Space-angular and temporal parameters of Čerenkov light emission in air showers of energy from 1 TeV down to 10 GeV. In de Jager, O. C., editor, *Proc. Towards a Major Atmospheric Cherenkov Detector V*, page 208, 1997.

[KVA] KVA website. *http://tur3.tur.iac.es*.

[Lee98] Lee, S. On the Propagation of Extragalactic High Energy Cosmic and γ-Rays. *Phys. Rev. D*, **58**:043004, 1998. (arxiv:astro–ph/9604098).

[Let02] Letokhov, V. S. Astrophysical lasers. *Quant. Electr.*, **32**:1065, 2002.

[Lor02] Lorenz, E. et al. A fast, large dynamic range analog signal transfer system based on optical fibers. *Nucl. Phys. A*, **461**:517, 2002.

[Lor03] Lorenz, E. Very High Energy Gamma Ray Astronomy. *Nucl. Phys. B (Proc. Suppl.)*, **20**:217, 2003.

[Lou00] Loudon, R. *The quantum theory of light,* 3^{rd} *ed.* Oxford Univ. Press, London, 2000.

[LTU] LTU, LT-Ultra Precision Technology GmbH website. *http://lt-ultra.com*.

[Luc05a] Lucarelli, F. et al. Development and first results of the MAGIC central pixel. In *Proc.* 29^{th} *ICRC Pune*, volume **5**, page 367, 2005.

[Luc05b] Lucarelli, F. et al. The timing system of the MAGIC telescope. *Int. J. Mod. Phys. A*, **20**:7012, 2005.

[Luc08] Lucarelli, F. et al. The central pixel of the magic telescope for optical observations. *Nucl. Instrum. Meth. A*, **589**:415, 2008.

[Mad06] Madau, P. Astronomy: Trouble at first light. *Nature*, **440**:1002, 2006. (arXiv:astro–ph/0604448).

[MAG] MAGIC website. *http://mppmu.mpg.de*.

[MAG06] MAGIC collab. (Albert, J. et al.). Variable Very High Energy Gamma–ray Emission from the Microquasar LSI +61 303. *Science*, **312**:1771, 2006.

[MAG07] MAGIC collab. (Albert, J. et al.). Very high energy gamma-ray observations during moonlight and twilight with the MAGIC telescope. *submitted*, 2007. (arXiv:astro–ph/0702475).

[MAG08a] MAGIC collab. (Albert, J. et al.). FADC signal reconstruction for the MAGIC-II telescope. *Nucl. Instrum. Meth. A, to appear*, 2008. (arXiv:astro–ph/0612385).

[MAG08b] MAGIC collab. (Albert, J. et al.). Implementation of the Random Forest Method for the Imaging Atmospheric Cherenkov Telescope MAGIC. *Nucl. Instrum. Meth. A*, **589**:415, 2008.

[MAG08c] MAGIC collab. (Albert, J. et al.). Periodic Very High Energy Gamma-Ray Emission From LS I+61° 303 Observed With The MAGIC Telescope. *Astrophys. J., to appear*, 2008. (arXiv:astro–ph/0801.3150).

[MAG08d] MAGIC collab. (Albert, J. et al.). Probing quantum gravity using photons from a flare of the active galactic nucleus Markarian 501 observed by the MAGIC telescope. *Phys. Lett. B)*, **668**:253, 2008.

[MAG08e] MAGIC collab. (Albert, J. et al.). Very High Energy Gamma Rays from a Distant Quasar: How Transparent is the Universe? *Science*, **320**:1752, 2008. (arXiv:astro–ph/0807.2822).

[MAG08f] MAGIC collab. (Albert, J. et al.). VHE Gamma-Ray Observation of the Crab Nebula and its Pulsar with MAGIC. *Astroph. J.*, **674**:1037, 2008. (arXiv:astro–ph/0705.3244).

[MAG08g] MAGIC collab. (Aliu, E. et al.). First bounds on the high-energy emission from isolated Wolf-Rayet binary systems. *Astrophys. J. Lett.*, **685**:l71, 2008.

[MAG08h] MAGIC collab. (Aliu, E. et al.). Observation of Pulsed γ-Rays Above 25 GeV From the Crab Pulsar with MAGIC. *Science, to appear*, , 2008.

[Man95] Mandel, L. and Wolf, E. *Optical coherence and quantum optics*. Cambridge Univ. Press, Cambridge, 1995.

[Man08] Mansutti, O. *Possible evidence for a new light boson from gamma ray cosmic propagation*. PhD thesis, University of Udine, 2008.

[Mar94] Maraschi, L. et al. The 1993 multiwavelength campaign on 3C 279: The radio to gamma-ray energy distribution in low state. *Astroph. J. Lett.*, **435**:L91, 1994.

[Maz07a] Mazin, D. and Goebel, F. Break in the VHE spectrum of PG 1553+113: new upper limit on its redshift? *Astrophys. J.*, **655**:L13, 2007. (arXiv:astro–ph/0611817).

[Maz07b] Mazin, D. and Raue, M. New limits on the density of the extragalactic background light in the optical to the far infrared from the spectra of all known TeV blazars. *Astron. Astrophys.*, **471**:439, 2007. (arXiv:astro–ph/0701694).

[MEG] MEG website. *http://www.ge.infn.it/∼sicca/meg*.

[Meu04] Meucci, M. et al. The trigger system of the MAGIC telescope: on-line selection strategies for Cherenkov telescopes. *Nucl. Instrum. Meth. A*, **518**:554, 2004.

[Mic21] Michelson, A. A. and Pease, F. G. Measurement of the diameter of alpha Orionis with the interferometer. *Astrophys. J.*, **53**:249, 1921.

[MLT] MLT, Media Lario Technologies website. *http://www.media-lario.com*.

[Mor58] Morrison, P. On Gamma-Ray Astronomy. *Nuovo Cimento*, **7**:858, 1958.

[Mor66] Morgan, B. L. and Mandel, L. Measurement of Photon Bunching in a Thermal Light Beam. *Phys. Rev. Lett.*, **16**:1012, 1966.

[Mor03] Moralejo, A. The Reflector simulation program v.0.6. Technical Report MAGIC TDAS 02-11, 2003.

[Mor04] Moralejo, A. et al. Monte Carlo studies on the MAGIC clone. Technical Report MAGIC TDAS 04-05, 2004.

[Mor08] Moralejo, A. and Gaug, M. A handbook of the standard MAGIC analysis chain. Technical Report MAGIC TDAS 08-02, 2008.

[MPD] MPD, Micro Photon Devices website. *http://www.microphotondevices.com*.

[MSI] MSISE webpage. *http://modelweb/gfsc.nasa.gov/atmos/msise.html*.

[Nal06] Naletto, G. et al. QuantEYE: a quantum optics instrument for extremely large telescopes. In *Proc. SPIE conference*, volume **6269**, pages 65691W–1, 2006.

[Nal07] Naletto, G. et al. Very fast photon counting photometers for astronomical application: from QuantEYE to AquEYE. In *Proc. SPIE conference*, volume **6583**, pages 65830B–1, 2007.

[Nel85] Nelson, W. R. et al. The EGS4 Code System. Technical Report SLAC-265, 1985.

[Nis52] Nishimura, J. and Kamata, K. On the Theory of Cascade Showers, I. *Prog. Theor. Phys.*, **7**:185, 1952.

[Ona04] Ona-Wilhelmi, E. et al. Determination of the Night Sky Background around the Crab Pulsar using its optical pulsation. *Astropart. Phys.*, **22**:95, 2004.

[Ong98] Ong, R. A. Very High Energy Gamma-Ray Astronomy. *Phys. Rep.*, **305**:93, 1998.

[Ost00] Ostankov, A. et al. A study of the new hemispherical 6-dynodes PMT from electron tubes. *Nucl. Instrum. Meth. A*, **442**:117, 2000.

[Pan04] Paneque, D. et al. A method to enhance the sensitivity of photomultipliers for Air Cherenkov Telescopes by applying a laquer that scatters light . *Nucl. Instrum. Meth. A*, **518**:619, 2004.

[Par08] Pareschi, G. and et al. Glass Mirrors by cold slumping to cover 100 m^2 of the MAGIC-II Cherenkov telescope reflecting surface. In *SPIE proceedings, Marseille, to appear*, 2008.

[Peg06] Pegna, R. et al. Performance of the Domino Ring Sampler in the MAGIC experiment. *Nucl. Instrum. Meth. A*, **567**:218, 2006.

[Pen65] Penzias, A. A. and Wilson, R. W. A measurement of the excess antenna temperature at 4080Mc/s. *Astrophys. J.*, **142**:419, 1965.

[Per08] Persic, M. and De Angelis, A. Intergalactic absorption and blazar γ-ray spectra. *Astron. Astrophys., to appear*, **483**:1, 2008. (arXiv:astro–ph/0711.2317).

[Pla00] Planck, M. Entropie und Temperatur strahlender Wärme. *Ann. d. Phys.*, **1**:719, 1900.

[Pri01] Primack, J. R. et al. Probing Galaxy Formation with High Energy Gamma-Rays. In *AIP Conference Proceedings*, volume **558**, page 463, 2001. (arXiv:astro–ph/0011475).

[Pun92] Punch, M. et al. (The WHIPPLE collab.). Detection of TeV photons from the active galaxy Markarian 421. *Nature*, **358**:477, 1992.

[Pur56] Purcell, E. The Question of Correlation Between Photons in Coherent Light Rays. *Nature*, **178**:1449, 1956.

[RAN] RANDOM FOREST website. *http://oz.berkeley.edu/users/breiman*.

[Res90] Ressell, M. T. and Turner, M. S. . *Comm. on Astrophys.*, **14**:323, 1990.

[ROO] ROOT website. *http://www.root.cern.ch*.

[Ros41] Rossi, B. and Greisen, K. Cosmic-Ray Theory. *Rev. Mod. Phys.*, **13**:240, 1941.

[Ros64] Rossi, B. *Cosmic Rays*. mcGraw–Hill, New York, 1964.

[Sai07] Saito, T. Y. et al. Recent progress of GaAsP HPD development for the MAGIC telescope project. In *Proc.* 30^{th} *ICRC Mérida*, volume **3**, page 1461, 2007. (arXiv:astro–ph/0709.2052).

[Sch26] Schrödinger, E. Quantisierung als eigenwertproblem, part I, II, III and IV. *Ann. d. Phys.*, **79**:361, 489, *Ibid.***80**:437, *Ibid.* **81**:109, 1926.

[Sch89] Schmid, H. M. Identification of the emission bands at $\lambda = 683.0$ nm and $\lambda = 708.8$ nm in V1016 Cyg. *Astron. Astrophys.*, **27**(211):L31, 1989.

[She03] Shearer, A. et al. Enhanced Optical Emission During Crab Giant Radio Pulses. *Science*, **27**(301):493, 2003.

[SIF08] In *Proc. of XCIV SIF Conference, Genova, to appear*, 2008.

[Sim08] Simet, M. et al. Milky Way as a kiloparsec-scale axionscope. *Phys. Rev. D*, **77**:063001, 2008.

[Sor02] Sorokin, P. P. and Glownia, J. H. Lasers without inversion (LWI) in Space: a possible explanation for intense, narrow-band, emissions that dominate the visible and/or far-UV (FUV) spectra of certain astronomical objects. *Astron. Astrophys.*, **27**(384):350, 2002.

[Ste08] Stecker, F. W. and Scully, S. T. Is the Universe More Transparent to Gamma Rays than Previously Thought? *submitted*, 2008. (arXiv:astro–ph/0809.2467).

[Sza94] Szabo, A. and Protheroe, R. Implications of particle acceleration in active galacic nuclei for cosmic rays and high energy neutrino astronomy. *Astropart. Phys.*, **2**:375, 1994.

[TAR] TAR, Telescope ARray website. *http://www.telescopearray.org*.

[Tav08] Tavecchio, T. and Mazin, D. Intrinsic absorption in 3C 279 at GeV–TeV energies and consequences for estimates of the EBL. *Mon. Not. R. Astron. Soc.*, **000**:1, 2008. (arXiv:astro–ph/0809.2467).

[Tes07a] Tescaro, D. et al. Study of the performance and capability of the new ultra-fast 2 GSample/s FADC data acquisition system of the MAGIC telescope. In *Proc.* 30^{th} *ICRC Mérida*, volume **3**, page 1393, 2007. (arXiv:astro–ph/0709.1410).

[Tes07b] Teshima, M. et al. Discovery of Very High Energy Gamma–Rays from the Distant Flat Spectrum Radio Quasar 3C 279 with the MAGIC Telescope. In *Proc.* 30^{th} *ICRC Mérida*, volume **3**, page 1045, 2007. (arXiv:astro–ph/0709.1475).

[Tes07c] Teshima, M. et al. SiPM development for Astroparticle Physics applications. In *Proc.* 30^{th} *ICRC Mérida*, volume **5**, page 985, 2007. (arXiv:astro–ph/0709.1808).

[TEV] TEV, TeV gamma-ray sources webpage. *http://www.mppmu.mpg.de/∼rwagner/sources/*.

[Tit65] Titulaer, U. M. and Glauber, R. J. Correlation Functions for Coherent Fields. *Phys. Rev. B*, **140**:676, 1965.

[Tow97] Townes, C. H. Astronomical masers and lasers. *Quant. Electr.*, **27**(12):1031, 1997.

[Twi57] Twiss, R. Q. et al. Correlation between photons in coherent light rays. *Nature*, **178**:1447, 1957.

[Twi59] Twiss, R. Q. and Little, A. G. The detection of time–correlated photons by a coincidence–counter. *Austr. J. Phys.*, **12**:77, 1959.

[Urr95] Urry, C. and Padovani, P. Unified Schemes for Radio–Load Active Galactic Nuclei. *Publ. Astron. Soc. Pac.*, **107**:803, 1995. (arXiv:astro–ph/9506063).

[US] US Standard Atmosphere webpage. *http://modelweb.gsfc.nasa.gov/atmos/us_standard.html*.

[VER] VERITAS website. *http://veritas.sao.arizona.edu*.

[Wal05] Wallace, P. T. *SLALIB – Position Astronomy Library 2.5-3, Programmer's Manual, http://star-www.rl.ac.uk/star/docs/sun67.htx/sun67.html*. 2005.

[Web90] Webb, J. R. et al. The 1987-1990 optical outburst of the OVV quasar 3C 279. *Astron. J.*, **100**:1452, 1990.

[Wee89] Weekes, T. C. et al. (The WHIPPLE collab.). Observation of TeV gamma rays from the Crab Nebula using the Atmospheric Cherenkov Imaging Technique. *Astrophys. J.*, **342**:379, 1989.

[Wee03a] Weekes, T. C. *Very high energy gamma–ray astronomy*. IOP, London, 2003.

[Wee03b] Weekes, T. C. et al. VERITAS: the Very Energetic Radiation Imaging Telescope Array System. *Astropart. Phys.*, **17**:221, 2003.

[Wit02] Wittek, W. Image parameters. Technical Report MAGIC TDAS 02-03, 2002.

[Yam07] Yamamoto, T. et al. The UHECR spectrum measured at the Pierre Auger Observatory and its astrophysical implications. In *Proc.* 30^{th} *ICRC Mérida*, 2007. (arXiv:astro–ph/0707.2638).

[Yer68] Yerbury, M. J. Experimental tests of the theory of an ampitude-limited correlation detector. *Radio Electr. Engr*, **36**:71, 1968.

[Zat66] Zatsepin, G. T. and Kuzmin, V. A. Upper Limit of the Spectrum of Cosmic Rays. *J. Exp. Theor. Phys. Lett.*, **4**:78, 1966.